Thermal Physics in Electronic and Optoelectronic Materials and Devices

by

Abhishek Yadav

A dissertation submitted in partial fulfillment
of the requirements for the degree of
Doctor of Philosophy
(Mechanical Engineering)
in The University of Michigan
2010

Dissertation Committee:

Assistant Professor Kevin P. Pipe, Co-Chair
Assistant Professor Max Shtein, Co-Chair
Associate Professor Rachel S. Goldman
Associate Professor Katsuo Kurabayashi

Acknowledgements

First and foremost, I would like to thank my advisors Prof. Kevin P. Pipe and Prof. Max Shtein. Their advice, motivation, and, ideas have been instrumental for this work. Prof. Kevin Pipe was a continuous source of new and innovative ideas. His objectivity and persistence were always helpful when facing challenging research problems. Prof. Max Shtein helped me through infinite discussions we had during our group meetings. His knowledge in organic semiconductors was helpful in bringing my research to quick fruition. His passion towards research and commitment for excellence always inspired me.

I am also grateful to my committee members Prof. Rachel S. Goldman and Prof. Katsuo Kurabayashi. Prof. Rachel Goldman provided many critical comments for work on quantum dot superlattices, which led to a better understanding of underlying issues. Being a GSI with Prof. Kurabayashi was helpful in understanding the importance of teaching in academia.

This work would not have been possible without help from many colleagues and collaborators including: Paddy Chan, Kwang Hyup An, Huarui Sun, Brendan O'Connor, Yiying Zhao, Steven E. Morris, Yansha Jin, Gunho Kim, Andrea Bianchini, Denis Nothern, Jinjjing Li and Chelsea Haughn. Paddy Chan and Huarui Sun sat next to my desk for most of my stay here, and, shared many meals and ideas about science. Paddy

Chan introduced me to the field of thermoreflectance, which was the starting point of my work on temperature modulation spectroscopy. Huarui Sun discussed intricate details of my research, and provided many useful ideas. Kwang Hyup An trained me on thermal evaporation system and many other experimental setups. Yansha Jin trained with me on TEM and shared many useful ideas about electron microscopy. Steve Morris helped me with thermal evaporation and purification of organic material.

I am also grateful to many friends who made my stay at Ann Arbor fun including: Deepak Kumar, Krispian Lawrence, Kulwinder Singh and Manvendu Bharadwaj. Deepak's advice on all matters of life was helpful.

Finally, this work would not have been possible without the support of my parents Satyanarain and Nisha Yadav and my sister Sugandha Yadav, who have shared my joys throughout past 5+ years.

Table of Contents

List of Figures

List of Tables

Abstract

Operating temperature affects the performance and reliability of most electronic and optoelectronic devices. The aim of this work is to study thermal physics in two particular contexts – thermoelectric devices and organic photovoltaic devices – to gain fundamental understanding of electrical transport and optical processes in these devices that could aid in increasing their efficiency and discovering new applications.

Thermoelectric devices convert heat energy to electricity and vice versa. Nanostructured materials offer a means to increase conversion efficiency. In the second part of this thesis we examine a practical means to enable 1D transport (and thus high conversion efficiency) using aligned chains of quantum dots. We show theoretically that this alignment can increase the thermoelectric power factor by a factor of 5 in common semiconductor material systems. In addition, we examine nanostructured thermoelectric materials based on HgCdTe quantum well superlattices. Using a steady state differential technique, we measure Seebeck coefficient and thermal conductivity, deriving a maximum thermoelectric figure-of-merit of 1.4 as compared to a maximum of ~ 0.33 for bulk HgCdTe.

Solid state thermoelectric generators can be useful for scavenging waste heat energy, provided they meet the requirements of scalability and low cost. As a potential means to meet the need of scalable fabrication as well as offer mechanical flexibility, we

explore the fabrication of thermoelectric power generators based on thin-films deposited on fibers that can be woven into energy-harvesting textiles. Using Ni-Ag metal thermocouples, we experimentally demonstrate the feasibility of this technology, developing a model for optimizing device performance and predicting the maximum power generated for more high-performance material systems.

In the third part of my thesis, we show that the strong link between temperature and optical properties of a material can be used to study the generation of excitons in organic semiconductor thin films, with important implications for solar energy conversion. An experimental setup based on a phase-sensitive detection technique is designed and used to measure the temperature dependences of exciton oscillator strength, linewidth, and transition energy. Importantly, this technique can differentiate Frenkel and charge transfer excitons, which play crucial but separate roles in the photovoltaic conversion process.

Chapter 1

Introduction

1.1 Thermal effects on electronic and transport properties of semiconductors

Fundamental properties of semiconductors such as band structure, probability distribution of charge carriers, and transport properties are strongly dependent on temperature. For example, the dielectric constant and other optical properties are based on interband electronic transitions for which the magnitude (oscillator strength), linewidth, and peak energy all vary upon temperature changes. Phonons and electrical carriers, which carry heat, have occupation probabilities and scattering rates that are all temperature-dependent. Below I give an overview of some of the common temperature dependencies encountered in semiconductor materials and devices, ending with a summary of the work of this thesis in studying thermal and temperature-dependent properties in nanostructured materials.

1.1.1 How does temperature affect the electronic bandgap?

An increase in temperature can cause thermal expansion in a crystalline lattice due to anharmonic interactions between neighboring molecules. The potential energy of atoms

at a displacement x from their equilibrium separation at T=0 can be written as [1]:

$$U(x) = cx^2 - gx^3 - fx^4 \tag{1.1}$$

where c,g, and f are experimentally determined constants. Upon an increase in temperature, the mean displacement of the atoms can be given by [1]:

$$\langle x \rangle = \frac{\int_{-\infty}^{\infty} x e^{-\frac{U(x)}{k_B T}} dx}{\int_{-\infty}^{\infty} e^{-\frac{U(x)}{k_B T}} dx} \tag{1.2}$$

assuming the Boltzmann distribution for atom positions. This then gives [1]:

$$\langle x \rangle = \frac{3g}{4c^2} k_B T \tag{1.3}$$

where $3gk_B/4c^2$ is the thermal expansion coefficient.

Thermal expansion in conjunction with the deformation potential can be used to derive the effect of thermal expansion on bandgap, although due to computational complexities it is common in practice to fit experimental data to an empirical relationship such as the Varshni equation [2]:

$$E_G(T) = E_0 - \frac{\alpha T^2}{T + \beta} \tag{1.4}$$

where E_0 is the bandgap at T=0 and α and β are fitting constants. It can be seen from this equation that an increase in temperature causes a decrease in the bandgap; an increase in interatomic spacing weakens the bond and makes it easier to excite an electron from the valence band to the conduction band.

1.1.2 How does temperature affect the Fermi distribution?

The probability of an electron occupying an energy level in the electronic density of states is given by the Fermi function [1]:

$$f(E) = \frac{1}{1 + e^{\frac{E - E_F}{k_B T}}} \tag{1.5}$$

where E_F is the Fermi energy, T is the absolute temperature, k_B is the Boltzmann constant, and E is the electron energy. **Figure 1.1** shows the Fermi distribution as a function of electron energy for a range of temperatures. At T=0, the Fermi distribution is a step function with no states occupied above the Fermi level. With an increase in temperature, states above the Fermi level are increasingly occupied. The free carrier concentration in a semiconductor depends on the Fermi level; for moderate densities, the Boltzmann approximation holds and is given by [3]:

$$n = N_C e^{\frac{E_F - E_C}{k_B T}} \tag{1.6}$$

where E_C is the energy of the conduction band edge and N_C is the effective electron density of states. For bulk semiconductors with parabolic dispersion [3],

$$N_C = 2\sqrt{\frac{m_e^* k_B T}{2\pi\hbar^2}} \tag{1.7}$$

where m_e^* is the electron effective mass and $\hbar$ is the reduced Planck's.

1.1.3 How does temperature affect the scattering of free carriers?

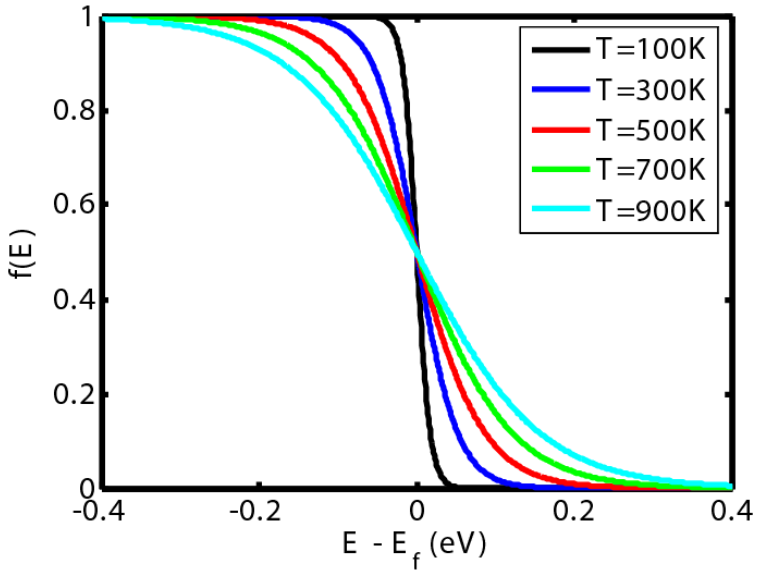

Figure 1.1. Effect of temperature on Fermi distribution

Electrons traveling through a semiconductor lose energy through collisions with lattice vibrations. The lattice vibration quantum, known as the phonon, has a frequency distribution governed by Bose-Einstein statistics [4]:

$$n_\omega = \frac{1}{e^{\frac{\hbar\omega}{k_B T}} - 1} \tag{1.8}$$

where ω is the radial frequency. The dispersion relation for phonons is dependent on material properties such as the speed of sound and interatomic potentials. The lowest energy branch of phonons, known as acoustic phonons, has a dispersion which passes through 0 and which can be written at low energies as [4]:

$$\omega = v_s q \tag{1.9}$$

where v_s is the speed of sound and q is the phonon wavevector. Interactions between electrons and phonons depend on the displacements of atoms from their equilibrium positions. The perturbation potentials for electron-phonon interactions can be written as [5]:

Acoustic phonons: $$U_{AP} \sim D\frac{\partial u}{\partial x} \tag{1.10}$$

Optical phonons: $$U_{OP} \sim D_o u \tag{1.11}$$

where u is the atomic displacement from equilibrium position, and D is a deformation potential for acoustic phonons and D_0 for optical phonons. With an increase in temperature, the displacements of atoms about their equilibrium positions increase, and as a result, the scattering of electrons with phonons is expected to increase. With an increase in temperature, higher energy phonons are occupied which can also lead to an increase in scattering rate.

1.1.4 How does temperature affect scattering of phonons?

The scattering of phonons determines the thermal conductivity of materials. For semiconductors, the dominating mechanisms for scattering of phonons are:

1) Phonon-Phonon scattering
2) Phonon impurity scattering
3) Phonon boundary scattering

The thermal conductivity can be written as [4]:

$$k = \frac{1}{2}\int_0^\infty \tau v^2 C_\omega d\omega \tag{1.12}$$

Where v is the group velocity of phonons, τ is the scattering time, and, C_ω is the specific heat capacity per unit frequency at temperature T and is given by [4]:

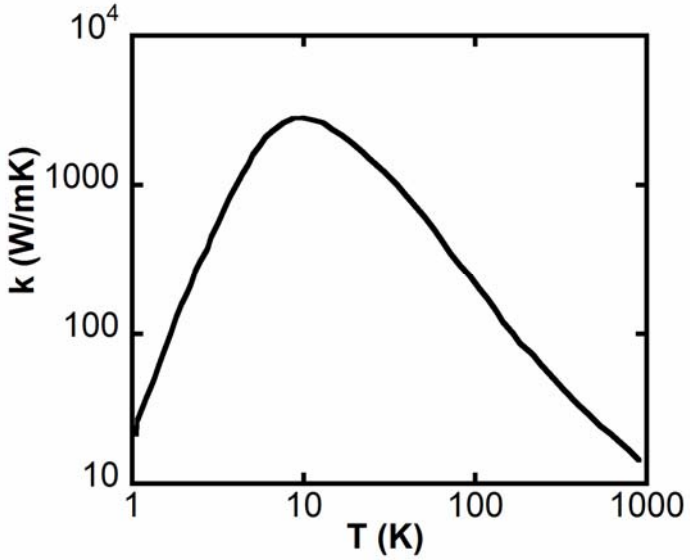

Figure 1.2 Thermal conductivity of GaAs as a function of temperature. Low temperature thermal conductivity is determined by boundary scattering, while, high temperature thermal conductivity is determined by phonon scattering.

$$C_\omega = \hbar\omega D(\omega)\frac{dn_\omega}{dT} \tag{1.13}$$

where $D(\omega)$ is the density of states of phonons. At high temperatures, the scattering is dominated by phonon-phonon scattering, whose scattering rate can be written as [4]:

$$\frac{1}{\tau} = Be^{-\frac{\theta_D}{bT}}T^3\omega^2 \tag{1.14}$$

where B and b are constants and θ_D is Debye temperature. This scattering gives the temperature dependence of thermal conductivity as [4]:

$$k \propto \frac{1}{T} \tag{1.15}$$

At low temperatures, where phonon occupation is low, the dominating scattering mechanism is boundary scattering. The scattering rate for phonon boundary scattering can be written as [4]:

$$\frac{1}{\tau} = \frac{b_s v}{L} \tag{1.16}$$

where b_s is shape factor, L is size of grains. The thermal conductivity at low temperature has a temperature dependence given by [4]:

$$k \propto T^3 \tag{1.17}$$

1.2 Overview of work

This work is focused on understanding and applying thermal effects to derive electronic structure and transport properties in organic and inorganic semiconductors.

Chapter 2 gives an introduction to thermoelectric energy conversion and the thermoelectric figure of merit (ZT). Thermoelectric generators are discussed, and their performance is compared to other heat engines.

Chapter 3 is focused on nanostructured materials for high efficiency thermoelectric energy conversion. As will be shown, the existing efficiencies of bulk thermoelectric materials are insufficient to compete with gas and steam compression cycle based systems. The fundamental cause is the inherent tradeoff between the electrical conductivity and Seebeck coefficient with increasing doping in semiconductors. We describe the motivation for nanostructured materials in which the electronic density of states is increased at the band edge, and use InAs/GaAs and Ge/Si as model material systems to demonstrate that 1D transport is achievable in composites which have quantum dots aligned in 1 dimension. We show that this geometry of incorporating aligned quantum dot in a matrix can result in a large increase in ZT.

Chapter 4 is focused on the design of integrated thermoelectric coolers for optoelectronic devices. Although thermoelectric coolers suffer from a low COP, they are suitable for microscale spot-cooling applications that require the cooler to be fabricated in an integrated growth process using epitaxy. ZT values for small barrier mercury cadmium

telluride superlattices, used to make infrared detectors, are characterized using a steady-state differential measurement. Coupled electrothermal simulations are performed, based on measured electrical and thermal properties, to optimize the geometry of a thermoelectric cooler monolithically integrated with an infrared detector pixel for maximum cooling.

Chapter 5 is focused on designing thermoelectric power generators for energy scavenging application. Similar to thermoelectric coolers, thermoelectric generators suffer from low conversion efficiencies compared to steam or internal combustion engines. However, many energy scavenging applications require scalable and low-cost devices. In particular, we study textile-based geometries for thin-film thermoelectric elements that are fabricated on flexible polymer fibers. The geometry of convectively-cooled single-fiber thermoelectric generators is optimized based on a measured effective heat transfer coefficient. Of many multi-fiber multi-thermocouple geometries possible, we focus on simple weave textile geometries, fabricating plain weave thermoelectric generators by a combination of thermal evaporation and electroless plating of metals.

Chapter 6 gives an introduction to organic photovoltaics, in which thermally activated transport of excitons and charge carriers mediates energy conversion. In this chapter, I briefly discuss the physics of light absorption, exciton formation and transport, highlighting the importance of exciton disassociation through the formation of charge transfer states. This chapter serves as background to Chapter 7, in a new characterization technique is introduced for organic semiconductors

Chapter 7 examines the effect of temperature on the electronic structure of organic semiconductors. Temperature modulation spectroscopy is proposed and applied to organic semiconductors for the first time. Using a phase-sensitive detection technique,

we measure the modulation in optical transmission spectrum caused by a periodic change in temperature for copper phthalocyanine. This modulation spectrum is used to determine excitonic transitions and the temperature dependences of oscillator strength, transition energy, and lifetime broadening. A clear difference in the temperature dependence of oscillator strength is observed for Frenkel and charge transfer (CT) excitons, motivating the broad use of this technique to determine exciton character and measure electronic coupling parameters for organic semiconductors.

Figure 1.3 shows an overview of work in this thesis.

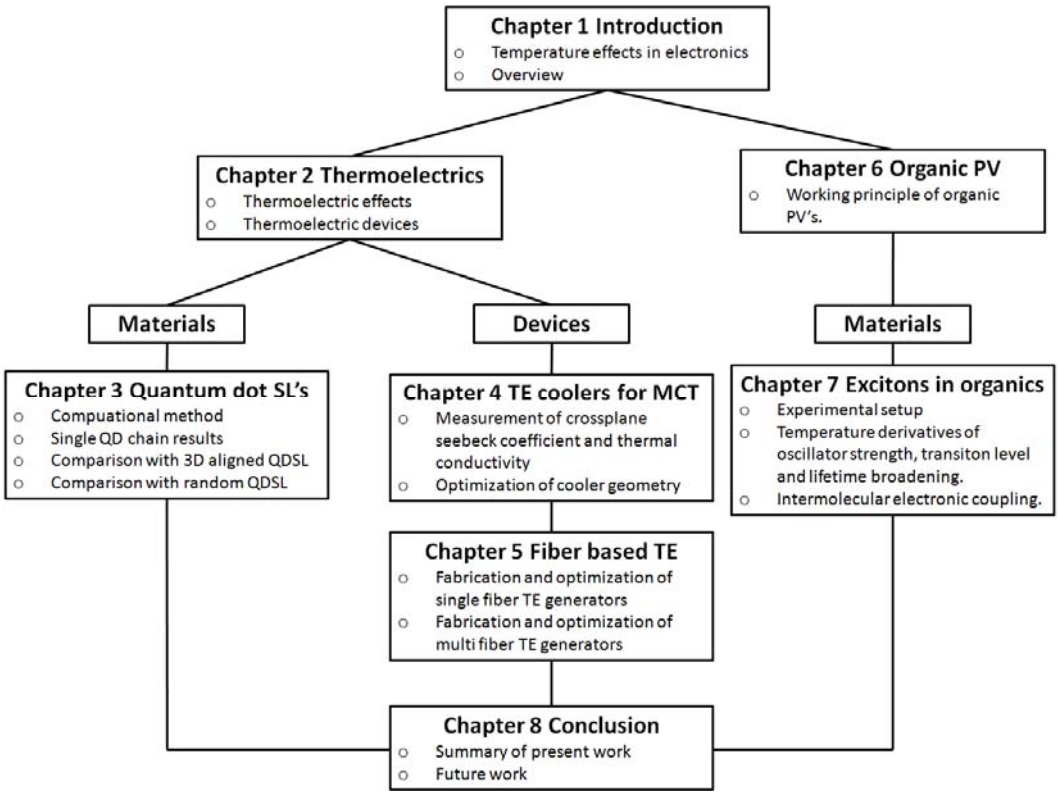

Figure 1.3. An overview of the work in this thesis.

Chapter 2

Thermoelectric energy conversion

2.1 Thermoelectric transport

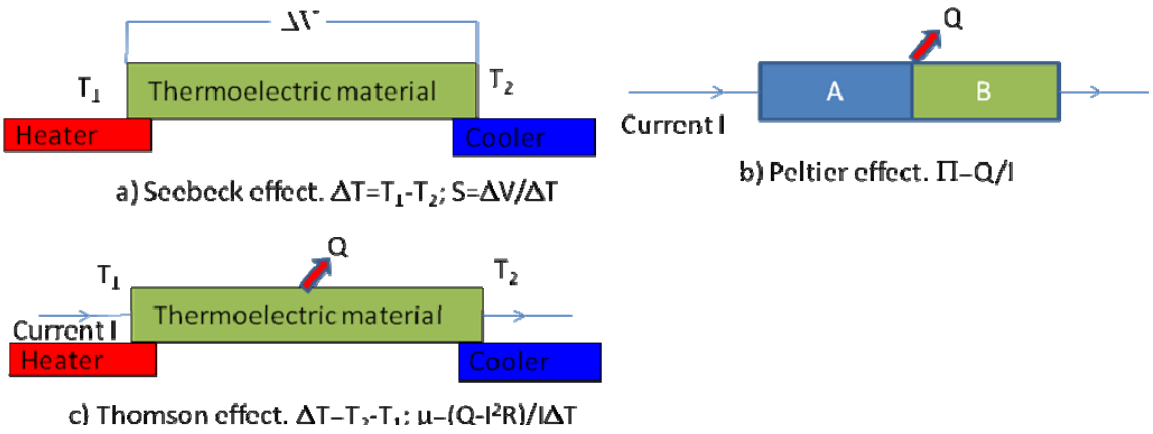

Figure 2.1. Illustration of thermoelectric effects: (a) Seebeck effect with Seebeck coefficient *S*, (b) Peltier effect with Peltier coefficient Π, and (c) Thomson effect with Thomson coefficient μ.

Thermoelectric effects are based on the transfer of electronic energy between kinetic form (heat) and potential form (voltage). In 1821, Thomas Seebeck discovered the Seebeck effect which is shown in **Fig.** 2.1(a) [6, 7]. When a temperature difference (ΔT) is applied across a conductor, a voltage difference ($\Delta V = S\Delta T$) is induced that is proportional to ΔT by the Seebeck coefficient *S*. This discovery was followed by the observation by Jean Peltier in 1834 of cooling or heating at a junction of dissimilar

metals on passing an electric current. This is known as the Peltier effect and is shown in **Fig.** 2.1(b) [6]. The Peltier coefficient is defined as the heat absorbed or rejected (Q) at the junction per unit electric current ($\Pi = Q/I$), and is related to the Seebeck coefficient by $\Pi = T \times S$. A third thermoelectric effect in which a current carrying conductor is heated or cooled in the presence of a temperature gradient was discovered by William Thomson (Lord Kelvin) in 1855. This is known as Thomson effect [6] and is shown in **Fig.** 2.1(c); the corresponding constant is known as the Thomson coefficient γ. Together, these three effects compose thermoelectric phenomena.

2.2 Thermoelectric devices

2.2.1 Thermoelectric power generator

A thermoelectric power generator converts heat energy into electrical energy using the Seebeck effect. In its most common form, a number of *n* and *p* type thermoelectric elements ("legs") are connected electrically in series and thermally in parallel, as shown in **Fig.** 2.2 (a). Since *n* and *p* type semiconductors generate induced thermal voltages of opposite sign, in this configuration their thermal voltages add. **Figure** 2.2 (b) shows picture of a commercially-available single stage thermoelectric module from Melcor [8]. The module is reversible, functioning as a cooler if a bias current is applied (as discussed in the next section).

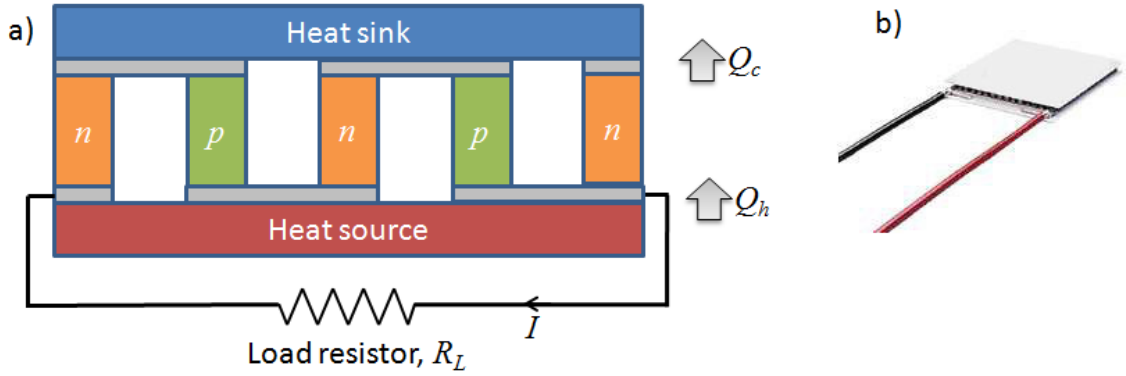

Figure 2.2. (a) Schematic of a thermoelectric power generator **(b)** picture of commercially available thermoelectric unit from Melcor.

In order to approximate the efficiency of thermoelectric energy conversion for the module, we assume that both the heat sink and heat source function as thermal reservoirs and have temperatures that are independent of heat flux. Under these conditions, the rate of heat transfer from the hot side can be written as [9]:

$$Q_h = K\Delta T + \alpha T_h I - \frac{1}{2} I^2 R \tag{2.1}$$

where Q_h is the rate of heat transfer at hot side, k is the net thermal conductivity, α is the net Seebeck coefficient, T_h is the hot side temperature, I is the current through the device, and R is the total electrical resistance of the device. Here we have assumed that the Seebeck coefficient of metal used to form the junctions is negligible, and that half of the resistive (I^2R) heating goes to each junction. The net thermal conductivity for thermal elements in parallel can be written as [9]:

$$k = k_n \frac{A_n}{l_n} + k_p \frac{A_p}{l_p} \tag{2.2}$$

where kn, An, and ln are the thermal conductivity, cross-sectional area, and length of the n type legs, and kp, Ap, and lp are the thermal conductivity, cross-sectional area, and

length of the p type legs. The net Seebeck coefficient is given by [9]:

$$\alpha = |\alpha_n| + |\alpha_p| \tag{2.3}$$

where α_n and α_p are the Seebeck coefficients of the *n* and *p* type materials. The efficiency of the thermoelectric generator is given by

$$\eta = \frac{I^2 R_0}{Q_h} \tag{2.4}$$

which reaches a maximum value (for an optimal leg geometry) of [9]:

$$\eta_{\max} = \left(1 - \frac{T_h}{T_c}\right) \frac{\sqrt{1 + ZT_{avg}} - 1}{\sqrt{1 + ZT_{avg}} + \frac{T_c}{T_h}} \tag{2.5}$$

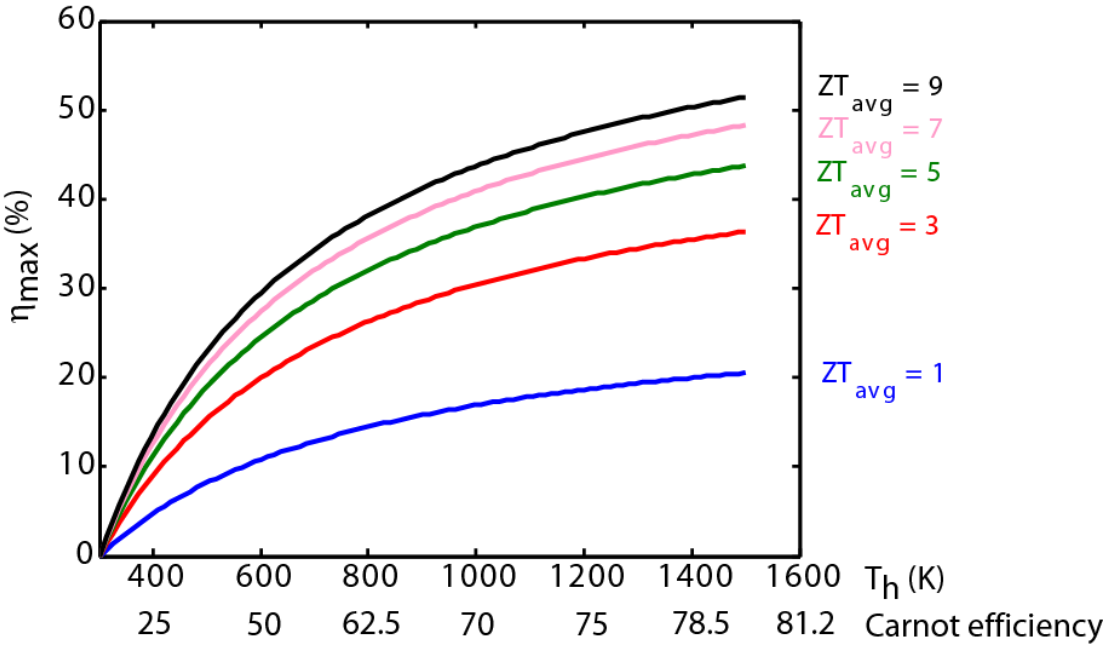

Figure 2.3. Maximum efficiency of thermoelectric power generator as a function of heat source temperature for different values of the figure of merit.

where *Z* is the dimensionless thermoelectric figure of merit defined by:

$$Z = \frac{\alpha^2}{k\rho} \tag{2.6}$$

and T_{avg} is the average temperature of heat sink and source given by

$$T_{av} = \frac{T_c + T_h}{2} \tag{2.7}$$

Figure 1.3 shows the maximum efficiency vs. hot side temperature for different values of ZT_{avg}, assuming a cold side temperature of 27°C. It is evident that the maximum efficiency depends on the dimensionless figure of merit. Steam engines used in fossil fuel fired power plants work at T_h ~ 700 K at efficiencies up to 40%. Internal combustion engines work at higher temperatures of T_h ~ 1000 K but also have larger losses leading to lower efficiencies in the range of 20-35%. Hence, a ZT_{avg} of greater than 3 is required to achieve efficiencies close to IC engines.

2.2.2 Thermoelectric cooler

Thermoelectric modules may also act as refrigerators or heat pumps if electrical current is applied as the driving force. Thermoelectric cooling is based on the Peltier effect as discussed above; thermoelectric cooler modules have a configuration that is identical to that of a thermoelectric power generator, as shown in **Fig.** 2.2. In **Fig.** 2.4 we show a simplified schematic of a thermoelectric cooler along with the transitions in energy for electron and hole distributions at metal/semiconductor interfaces that give rise to cooling. When an electric current is passed through the device, electrons in the *n*-type semiconductor legs and holes in the *p*-type legs flow from the cold side to the hot side. Because of the band conduction constraint, the energies at which these carriers flow are significantly higher than their average energy in the metal contacts. To make up this energy difference, electrons and holes pull heat energy from the surrounding lattice when they move from a metal contact to a semiconductor leg. Conversely, when electrons and holes move from a semiconductor leg to a metal contact, they lose this energy to the surrounding lattice, heating it up. In addition, resistive heating in the leg bulk region and

parasitic heat conduction from the hot interface to cold interface also occurs. The rate of cooling can be written as [9]:

$$Q_c = \alpha T_c I - \frac{1}{2} I^2 R - K\Delta T \tag{2.8}$$

where T_C is the temperature of cold side and other parameters are as defined in section 2.2.1. The net voltage drop across the device can be written as [9]:

$$V = \alpha \Delta T + IR \tag{2.9}$$

where the term $\alpha\Delta T$ takes into account the bulk Seebeck voltage which must be overcome by the external power supply. Then the power supplied can be written as [9]:

$$P = IV = \alpha I \Delta T + I^2 R \tag{2.10}$$

The coefficient of performance (*COP*) of a heat pump can be written as [9]:

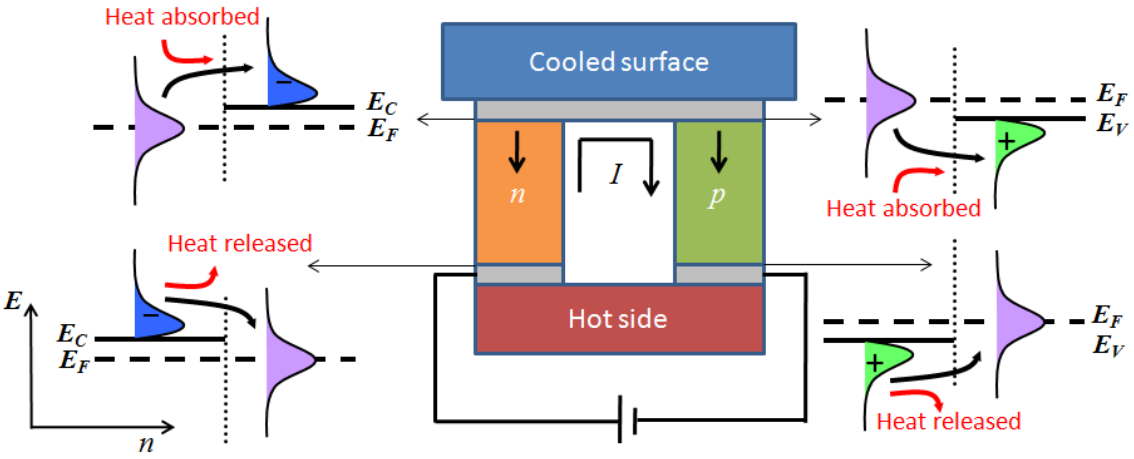

Figure 2.4. Schematic of a thermoelectric cooler with a solid state description of the origin of cooling.

$$COP = \frac{Q_c}{P} = \frac{\alpha T_c I - \frac{1}{2} I^2 R - K\Delta T}{\alpha I \Delta T + I^2 R} \tag{2.11}$$

Again, Equation (2.11) can be optimized for the leg geometry and thermoelectric parameters, resulting in a maximum *COP* that can be written as [9]:

$$\eta_{\max} = \left(\frac{T_c}{T_h - T_c} \right) \frac{\sqrt{1 + ZT_{avg}} - \frac{T_h}{T_c}}{\sqrt{1 + ZT_{avg}} + 1} \tag{2.12}$$

Figure 2.5 shows the maximum COP as a function of the dimensionless figure of merit for T_h=300K and ΔT = 30K.With an increase in ZT, the COP increases. The COP of the best current bulk thermoelectric material (bismuth telluride) is also shown. In comparison, vapor compression cycle based refrigerators give a much higher COP.

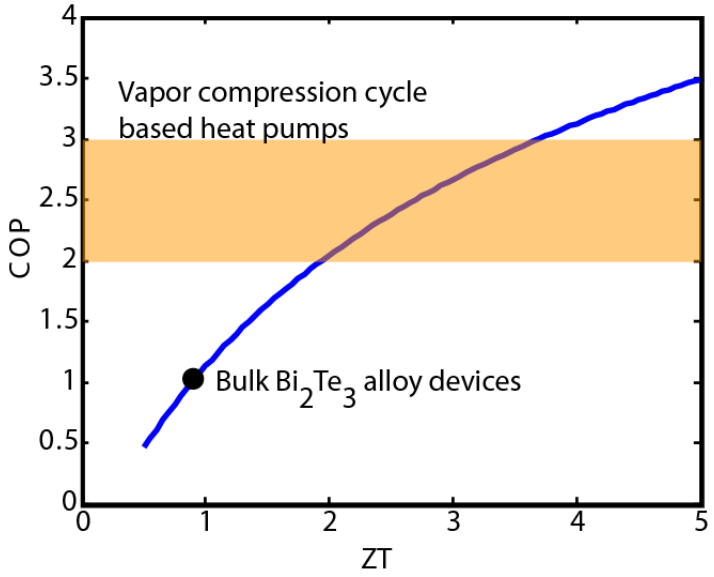

Figure 2.5. Maximum COP of a thermoelectric refrigerator as a function of dimensionless figure of merit ZT for T_h=300K and ΔT = 30K. The COP of commercially available, vapor compression cycle based refrigerators is also shown.

2.3 Status of thermoelectric materials

The best thermoelectric materials known are chalcogenides containing bismuth or antimony as the electropositive atom and tellurium as the electronegative atom. **Figure** 2.6 shows ZT of the best bulk thermoelectric materials [10]. At temperatures less than 450 K, bismuth telluride (Bi_2Te_3) is the best thermoelectric material. For temperatures of 450 K to 850 K, lead telluride has the best performance. High-temperature thermoelectrics are generally made from silicon germanium compounds.

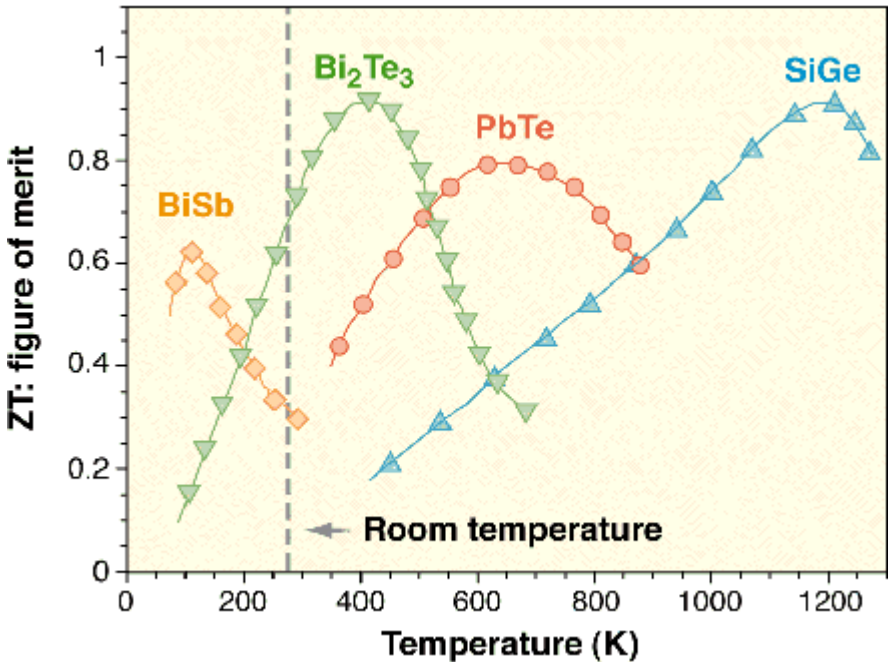

Figure 2.6. ZT of best thermoelectric materials as a function of temperature. From [4].

Chapter 3

Thermoelectric properties of aligned quantum dot chains

3.1 Theory of thermoelectric transport

In this section we look at the tradeoff between electrical conductivity and Seebeck coefficient that limits the thermoelectric power factor, and consequently, the thermoelectric figure of merit of bulk materials. Our discussion follows a similar path to that given in [4, 11]. The transport of charge carriers is governed by the Boltzmann transport equation, which can be written as:

$$\frac{\partial f}{\partial t} + \vec{\mathrm{v}} \cdot \nabla_r f + \frac{\vec{F}}{m} \cdot \nabla_{\mathrm{v}} f = \left.\frac{\partial f}{\partial t}\right|_{collision} \tag{3.1}$$

where f is the distribution function of charge carriers and is a function of time, spatial coordinates, and momentum coordinates, $\vec{\mathrm{v}}$ is the velocity of the charge carriers, and $\vec{F}$ is the force acting on charge carriers. We make simplifying assumptions of steady-state electron transport in 1D along the x direction, a small change in the distribution function and its gradient on application of an electric field, and elastic scattering. Given a force -eE_{x} on electrons, where E_{x} is the applied electric field along the x direction, Equation (3.1) can be written as:

$$v_x \frac{\partial f_0}{\partial x} - \frac{eE_x}{m} \frac{\partial f_0}{\partial v_x} = -\frac{f - f_0}{\tau} \tag{3.2}$$

where f_0 is the equilibrium distribution function and τ is the momentum relaxation time. The carrier distribution can then be written as:

$$f = f_0 - \tau \left(v_x \frac{\partial f_0}{\partial x} - \frac{eE_x}{m} \frac{\partial f_0}{\partial v_x} \right) \tag{3.3}$$

The equilibrium distribution for electrons is given by the Fermi-Dirac distribution:

$$f_0 = \frac{1}{1 + e^{\frac{E - E_f}{k_B T}}} \tag{3.4}$$

where E is the energy of electrons, E_f is the Fermi level, k_B is the Boltzmann constant, and T is the absolute temperature. The first term in parentheses on the right side of Equation (3.3) is a gradient in the distribution function due to a change in either the Fermi level or the carrier temperature with position. The second term is due to the force of the applied field on the electron distribution. The spatial gradient of the distribution function can be written as:

$$\frac{\partial f_0}{\partial x} = \frac{\partial f_0}{\partial E_f} \frac{\partial E_f}{\partial x} + \frac{\partial f_0}{\partial T} \frac{\partial T}{\partial x} \tag{3.5}$$

Using Equation (3.4) this can be further simplified as:

$$\frac{\partial f_0}{\partial x} = -\frac{\partial f_0}{\partial E} \frac{\partial E_f}{\partial x} - \frac{E - E_f}{k_B T} \frac{\partial f_0}{\partial E} \frac{\partial T}{\partial x} \tag{3.6}$$

The current density can be written as:

$$j = -\frac{2}{(2\pi)^3} \int_{-\infty}^{\infty} \int_{-\infty}^{\infty} \int_{-\infty}^{\infty} e v_x f dk_x dk_y dk_z \tag{3.7}$$

Substituting equation (3.3) and (3.6) in this expression yields:

$$j = -\frac{2}{(2\pi)^3}\int_{-\infty}^{\infty}\int_{-\infty}^{\infty}\int_{-\infty}^{\infty} ev_x\left(f_0 - \tau\left(-v_x\frac{\partial f_0}{\partial E}\frac{\partial E_f}{\partial x} - v_x\frac{E-E_f}{k_BT}\frac{\partial f_0}{\partial E}\frac{\partial T}{\partial x} - \frac{eE_x}{m}\frac{\partial f_0}{\partial E}\frac{\partial E}{\partial v_x}\right)\right)dk_x dk_y dk_z \tag{3.8}$$

The integral over f_0 is zero since the current densities in the $+x$ and $-x$ directions are the same for the equilibrium distribution. Equation 1.8 can then be reduced to:

$$j = L_{11}\left(\frac{1}{e}\frac{\partial E_f}{\partial x} + E_x\right) + L_{12}\left(-\frac{\partial T}{\partial x}\right) \tag{3.9}$$

where L_{11} and L_{12} are defined as:

$$L_{11} = \frac{2}{(2\pi)^3}\int_{-\infty}^{\infty}\int_{-\infty}^{\infty}\int_{-\infty}^{\infty} ev_x^2\tau\left(-\frac{\partial f_0}{\partial E}\right)dk_x dk_y dk_z \tag{3.10}$$

$$L_{12} = -\frac{2}{(2\pi)^3}\int_{-\infty}^{\infty}\int_{-\infty}^{\infty}\int_{-\infty}^{\infty} ev_x^2\tau\frac{E-E_f}{k_BT}\left(-\frac{\partial f_0}{\partial E}\right)dk_x dk_y dk_z \tag{3.11}$$

The electrochemical potential can be written as:

$$\phi = -\frac{E_c}{e} - \frac{E_f}{e} \tag{3.12}$$

where E_c is the conduction band edge and E_f is measured with respect to E_c. The gradient of electrochemical potential is given by:

$$\frac{\partial \phi}{\partial x} = F_x - \frac{1}{e}\frac{\partial E_f}{\partial x} \tag{3.13}$$

where $F_x = -(1/e)\partial E_c/\partial x$ is the external applied electric field. Equation (3.9) can then be written as:

$$j = L_{11}\left(-\frac{\partial \phi}{\partial x}\right) + L_{12}\left(-\frac{\partial T}{\partial x}\right) \tag{3.14}$$

In the case of no temperature gradient, the proportionality between electron current density and the gradient of electrochemical potential is given by the electrical

conductivity. Hence, electrical conductivity σ can be written as:

$$\sigma = L_{11} \tag{3.15}$$

In the case of a temperature gradient and open circuit, the proportionality between induced voltage and the temperature gradient is given by Seebeck coefficient (S), which can be written as:

$$S = \frac{-\partial\phi / \partial x}{\partial T / \partial x} = \frac{L_{12}}{L_{11}} \tag{3.16}$$

From Equation (3.11) we can see that the Seebeck coefficient is proportional to $\sigma(E)(E-E_f)$ where $\sigma(E)$ is the integrand of L_{11}. The Seebeck coefficient is proportional to the average energy of electrons with respect to the Fermi energy under open circuit condition, weighted by the electrical conductivity at each energy level occupied by an electron. Hence, the Seebeck coefficient will be larger in magnitude if electrons carry energy that is greater than or less than the Fermi energy. In contrast, the electrical conductivity is maximized if the Fermi level lies in the conduction band, which results in a large number of electrons participating in transport. **Figure** 3.1(a) shows the density of

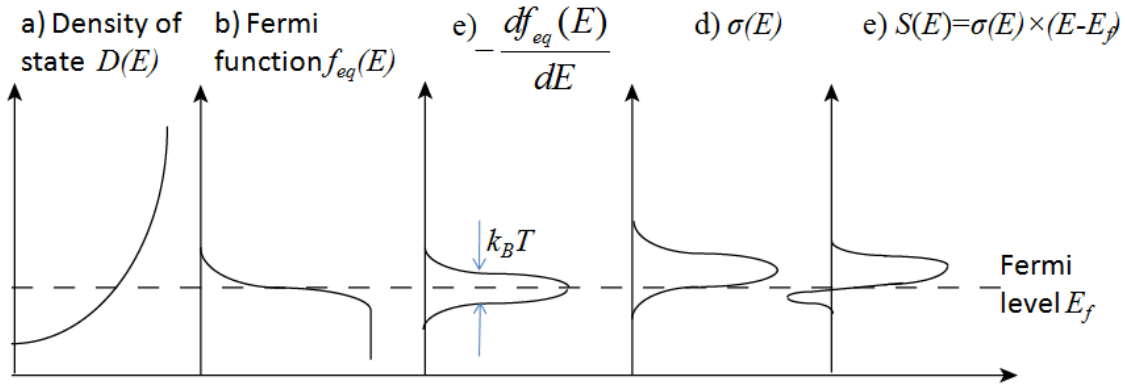

Figure 3.1. (a) 3D electron density of states, (b) Fermi distribution, (c) derivative of Fermi function, (d) electrical conductivity, and (e) Seebeck coefficient as a function of energy.

states of electrons in bulk semiconductors. **Figs** 3.1(b) and (c) show the Fermi function and its derivative with respect to energy. The derivative is important because only energy levels with nonzero values of the derivative participate in transport. **Fig.** 3.1 (d) shows the electrical conductivity, which is a convolution of the density of states and the derivative of the Fermi function. It follows the derivative of Fermi function closely, which implies that only electrons near the Fermi level can participate in charge transport. For the Seebeck coefficient (shown in **Fig.** 3.1 (e)), the average energy with respect to the Fermi energy must be taken into account. Electrons above and below the Fermi level carry thermal energy in opposite directions (even though they travel in the same direction) and hence their contributions to the Seebeck coefficient are of opposite sign.

3.2 Nanostructured materials for high efficiency thermoelectric devices

Nanostructured materials, which may be tailored for optimum transport of heat and electricity, have been proposed for the next generation of thermoelectric materials [12-15]. As seen in Section 2.1, the electrical conductivity and Seebeck coefficient have opposite behavior as Fermi level is increased in bulk materials. Fermi level in semiconductors increases with an increase in doping. The Seebeck coefficient can be nonzero only if the energy distribution of conducting carriers is asymmetric about the Fermi level. This implies that the Fermi level cannot be too deep in the conduction band. However, if it moves too close to the band edge, the density of states becomes small, leading to a reduction in electrical conductivity. If the density of states at the band edge can be increased, however, then a higher electrical conductivity can be achieved without sacrificing Seebeck coefficient, leading to a higher ZT. Low dimensional materials such

as quantum wells and nanowires have a very high density of states at the band edge, as shown in **Fig.** 3.2. It is clear from recent work on nanowires [16] and nanowire superlattices [17] that nanowires can increase the thermoelectric power factor significantly beyond its bulk value. For example, Mingo calculated the thermoelectric power factor ($S^2\sigma$, where S is the Seebeck coefficient and σ is the electrical conductivity) for III-V [18] and II-VI [19] nanowires, predicting substantial increases with respect to the corresponding bulk materials, as shown in **Fig.** 3.3(b). For comparison, the thermoelectric power factor of bulk III-V semiconductors is shown in **Fig.** 3.3(a). Due to the increased control of the density of states and hence the energies of charge carriers, 1D quantum structures are predicted to have a significantly higher power factor than not only

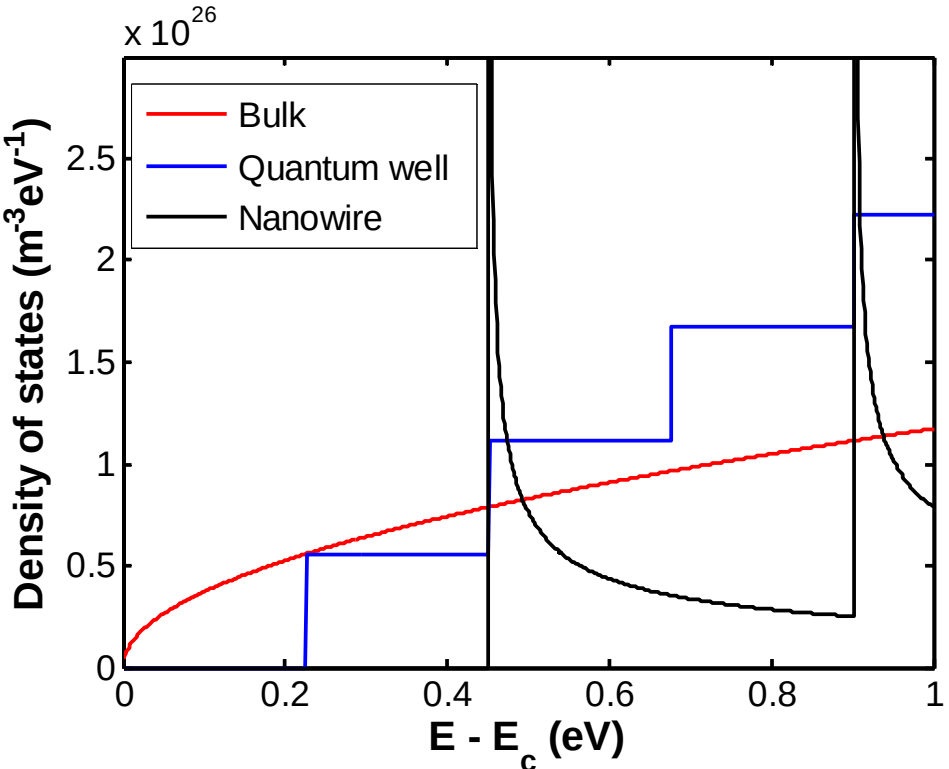

Figure 3.2. Electronic density of states of a 3D bulk GaAs, 2D GaAs quantum well with infinite confining potential and well thickness of 5 nm, and 1D square quantum nanowire with infinite confining potential and wire size of 5 nm.

bulk materials but also quantum well (QW) and 3D ordered quantum dot (QD) superlattices (SL) [17]. However, nanowires are difficult to implement in thermoelectric devices due to practical issues with electrical contacts, structural integrity, and wire alignment [20].

Quantum dot superlattices (QDSLs) provide a promising alternative to nanowires, as they can be fabricated within a matrix that provides structural support. Furthermore, QDs can be incorporated into a matrix with various spatial arrangements. Most QD nanocomposites consist of QDs arranged randomly within a matrix with negligible long range ordering of the QDs [21]. For random QD nanocomposites, a power factor intermediate to those of the matrix and QDs is predicted [22]. In another approach, known as a 3D ordered QDSL, [23] the electronic wavefunctions of neighboring QDs interact strongly, leading to delocalization of electrons and miniband formation in 3 directions. For these structures, the decreased density of states compared to the bulk leads to a lower predicted electrical conductivity and consequently a decrease in the power

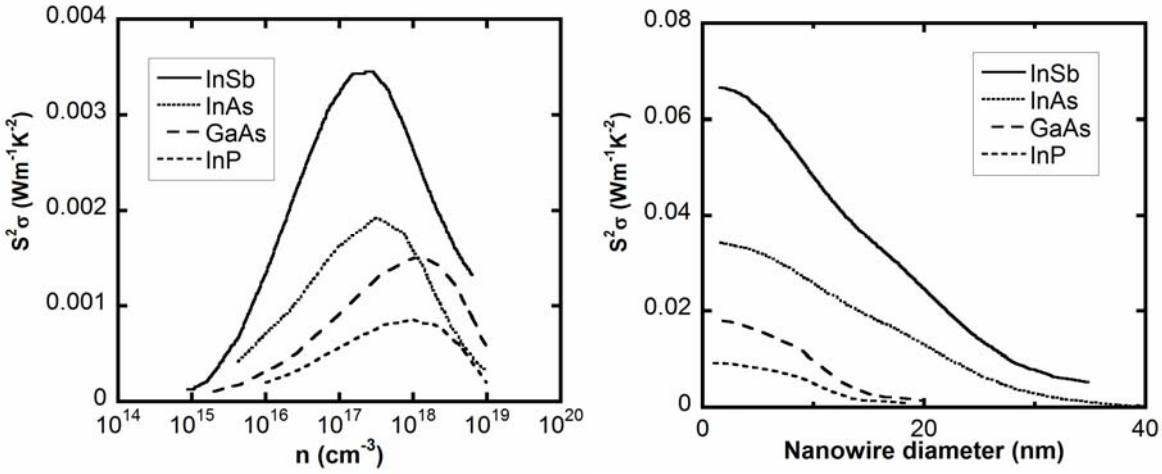

Figure 3.3. (a) Thermoelectric power factor of bulk III-V semiconductors **(b)** Thermoelectric power factor of III-V semiconductor nanowires. Figures reproduced from Mingo [18].

factor. Here we calculate the thermoelectric properties of a QD chain nanocomposite, which consists of a QDSL with a 2D pattern of QDs that are aligned to form chains [24-28], with negligible interactions between neighboring chains. This geometry leads to confinement of electrons in the chains, with carrier transport through minibands occurring only along the chains. We predict that QD chain nanocomposites can have greatly enhanced thermoelectric properties due to 1D carrier transport along the chains, analogous to transport in nanowires or nanowire SLs. In both nanowires and QD chain nanocomposites, a reduction in thermal conductivity (λ) with respect to the bulk is expected to lead to further enhancement in the thermoelectric figure of merit $ZT = S^2\sigma/\lambda$ [29–31]. For example, while the bulk thermal conductivities of GaAs and Si are 55 W/mK and 130 W/mK respectively, the addition of ErAs nanoparticles to InGaAs has been shown to decrease its thermal conductivity by a factor of 2 [30]. Here we focus on the electronic contribution to ZT ($S^2\sigma$) for two material systems (InAs/GaAs and Ge/Si) that are frequently utilized in electronic and optoelectronic applications. Both are compressively strained semiconductor systems in which Stranski-Krastanow (SK) growth leads to self-assembled QD formation; control of the ordering of such QDs is an active area of investigation [32, 33]. For GaAs (Si) with embedded InAs (Ge) QD chains, we calculate an increase in the thermoelectric power factor by a factor of 3 (1.5) in comparison with the corresponding GaAs (Si) bulk.

3.3 Theory and Calculation Method

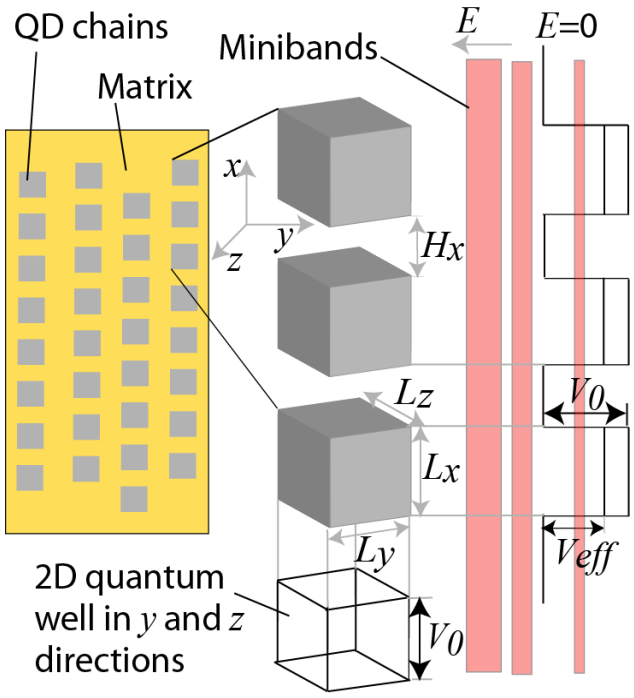

Figure 3.4. Illustration of aligned quantum dot chain, energy minibands, and potential wells in x,y, and z directions. L_x, L_y and L_z are the QD sizes in x,y,z directions, H_x is the QD spacing along the direction of alignment, V_0 is the confining potential, and V_{eff} is the effective confining potential for the x direction.

Figure 3.4 illustrates the alignment of QDs, which can take place either parallel to the growth direction (vertical chain) or perpendicular to the growth direction (horizontal chain). Both vertical and lateral alignment have been observed experimentally for InAs/GaAs QDs using special annealing sequences [25-27] and/or in situ buffer layer patterning [24, 28]. Vertical and lateral alignment has also been observed in Ge/Si QDs [32, 34]. For transport along a QD chain aligned in the x direction, we approximate the QDs as cubes of dimensions L_x, L_y, and L_z, with inter-dot spacing H_x and interchain spacing H_i. The Schrödinger equation is solved in the envelope function effective mass approximation [35]. Using a self-consistent solution to the Schrödinger and Poisson

	n-GaAs/InAs	*p*-Ge/Si
m_w	0.04[39,40]	0.28[23,42]
m_b	0.067[39]	0.49[23,42]
V_0 (eV)	0.45[39,41]	0.45[23,42]
τ (Sec)	1.33×10^{-13}	1.0×10^{-12}
L_x (nm)	10	4
L_y=L_z (nm)	5	4
H_x(nm)	5	2
n_{bulk} (cm^{-3})	5×10^{18}	3×10^{19}

Table 3.1. Effective mass and band offsets for InAs and Ge QDs. Here, m_b and m_w are the effective masses of the bulk and the QD, respectively, V_0 is the confining potential, and τ is the relaxation time. The QD size spacing, and bulk ionized impurity concentration used in calculations of the QD chain composite and random QD nanocomposite power factors are also given. L_x, L_y and L_z are the QD size in *x*,*y*,*z* directions, H_x is the QD spacing along direction of alignment, n_{bulk} is the bulk ionized impurity concentration.

equations, the error in the position of the energy bands due to neglecting the effect of band-bending has been shown to be less than 5% [36]. Hence, for ease of calculation, band-bending is neglected. In the directions perpendicular to the QD chain, 2D confinement is approximated by two 1D QWs with confined subband energy levels [36]. Using these subband energy levels, an effective potential along the QD chain (V_{eff}) is calculated, as illustrated in **Fig.** 3.4. V_{eff} is then used in a Kronig-Penny model to calculate the miniband energy levels as a function of k_x, i.e. the miniband dispersion

$E(k_x)$. Finally, $E(k_x)$ is used to calculate the density of states $2/(Ly \times Lz) \times dk_x/d\mathrm{E}$. The electronic transport properties σ and S are then calculated using the Boltzmann transport equation by summing over all n minibands [11]:

$$\sigma = \frac{q^2 \tau}{\pi L_y L_z} \sum_n \int_{\frac{-\pi}{L_x+H_x}}^{\frac{\pi}{L_x+H_x}} \mathrm{v}_{x,n}\left(k_x\right)^2 \left(-\frac{\partial f_0}{\partial E}\right) dk_x \tag{3.17}$$

$$S = \frac{-1}{qT} \frac{\sum_n \int_{\frac{-\pi}{L_x+H_x}}^{\frac{\pi}{L_x+H_x}} \mathrm{v}_{x,n}\left(k_x\right)^2 \left(-\frac{\partial f_0}{\partial E}\right)\left(E_n\left(k_x\right) - E_f\right) dk_x}{\sum_n \int_{\frac{-\pi}{L_x+H_x}}^{\frac{\pi}{L_x+H_x}} \mathrm{v}_{x,n}\left(k_x\right)^2 \left(-\frac{\partial f_0}{\partial E}\right) dk_x} \tag{3.18}$$

Here, the integration is over the miniband quasi Brillouin zone [37], q is the electron charge, τ is the relaxation time for carriers, T is the temperature, f_0 is the equilibrium Fermi distribution, E_f is the Fermi level, k_x is the wavevector for minibands along the QD chain, $E(k_x)$ is the dispersion relation obtained from the solution of the Schrödinger wave equation, and $\mathrm{v_x}$ is the electron group velocity given by:

$$\mathrm{v}_{x,n}\left(k_x\right) = \frac{1}{\hbar} \frac{\partial E_n\left(k_x\right)}{\partial k_x} \tag{3.19}$$

We have studied two different material systems: InAs/GaAs and Ge/Si, which have different confining potentials and free carrier effective masses. For InAs/GaAs (Ge/Si), the band offset is dominated by the conduction (valence) band offset [38]; hence, we study *n*-InAs/GaAs and *p*-Ge/Si. A Fermi level of zero corresponds to the GaAs conduction band edge (silicon valence band edge) for the InAs/GaAs (Ge/Si) system. We use literature values of conduction and valence band offsets and QD carrier effective

masses that are corrected for strain and confinement effects, as given in Table 3.1, which are taken from Refs. [39-41] for InAs/GaAs and [23, 42] for Ge/Si. For all calculations, we assume room temperature (300 K) and a constant relaxation time, with values listed in Table 3.1. For the InAs/GaAs system, τ is derived from the mobility in bulk GaAs at the doping level that corresponds to a Fermi level position at the conduction band edge. For the Ge/Si system, τ is taken from Ref. [23].

3.4 Single Quantum Dot Chains: Size Effects

In this section, we examine the effects of QD size on the thermoelectric properties of a single QD chain. Similar trends were observed for both Ge/Si and InAs/GaAs systems; for simplicity, we focus on the InAs/GaAs system. **Figure**s 3.5 (a) and 3.5 (b) show σ and S as a function of the Fermi level for a single InAs/GaAs QD chain, in comparison with that of bulk GaAs. Oscillations in σ and S occur as the Fermi level is increased and swept through the minibands. Similar oscillations as a function of Fermi level have been predicted for various nanostructured materials including 3D ordered QDSLs [23, 37], quantum well (QW) SLs [43], and nanowire SLs [17]. For 1D transport (along an individual nanowire), σ is inversely proportional to the wire diameter [16]. Additionally, for QD chains, an increase in σ is predicted to occur with increasing QD diameter due to an increase in the number of subbands per QD, leading to a greater number of QD chain minibands. Since the total density of states at any energy level is the summation of the density of states for each individual miniband at that energy level, the presence of multiple minibands increases the total density of states and hence σ.

In **Fig.** 3.5 (c), the power factor ($S^2\sigma$) is plotted as a function of Fermi level for a variety of QD sizes, in comparison with that of bulk GaAs. In all cases, $S^2\sigma$ is maximized

when the Fermi level lies within a few k_BT of the GaAs matrix conduction band edge. For higher Fermi levels, the minibands form a nearly continuous band, leading to low values of S and $S^2\sigma$.

3.5 QD Chain Nanocomposite

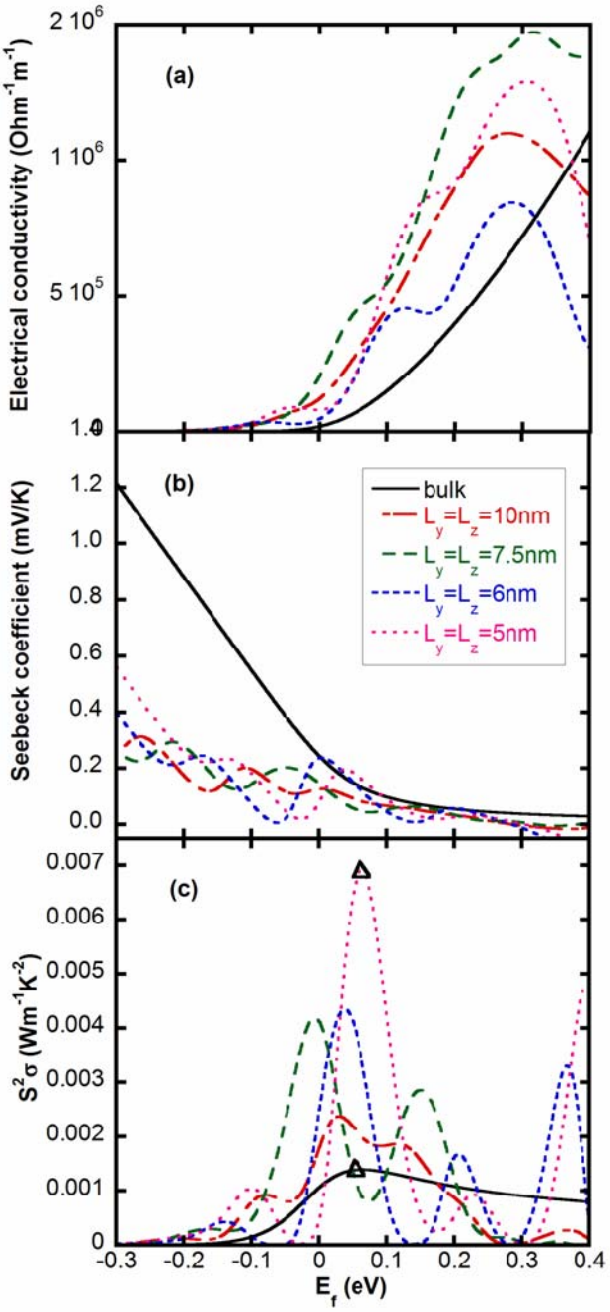

Fig. 3.5. (a) Electrical conductivity, **(b)** Seebeck coefficient, and **(c)** power factor as a function of Fermi level for individual InAs/GaAs QD chain with L_x=10nm and H_x=5nm. Triangles denote the maximum in $S^2\sigma$ of bulk and QD chain with dot size L_y=L_z=5nm, used in the calculation of normalized $S^2\sigma$ of the QD chain nanocomposite in **Fig.** 3.6.

In this section, we compare the thermoelectric properties of a multiple QD chain nanocomposite (i.e. a 2D pattern of QD chains) with those of a random QD nanocomposite. We calculate the net $S^2\sigma$ of the QD chain and compare it to that of the randomly ordered nanocomposite, considering both as a function of the volume fraction of QDs (φ). For a given values of matrix and QD carrier densities, we use a parallel conductor model [44] for the QD chain and a 2D resistance network [45] for the randomly ordered nanocomposite. In the parallel conductor model, charge conduction in the matrix is assumed to occur in parallel to that through the QD chains. For φ <0.4 (the percolation threshold), 2D models have been reported to be sufficient [46]. The size and spacing of QDs as well as the bulk doping used in the calculations are given in Table 3.1.

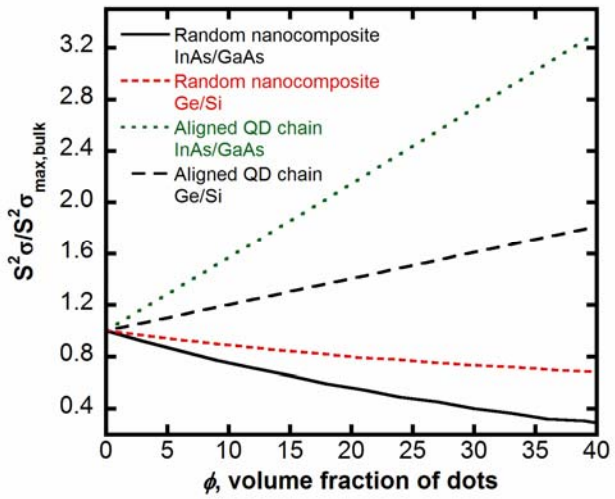

Figure 3.6. Comparison of normalized power factors, (i.e. the maximum power factor divided by the maximum power factor of the bulk) for the QD chain nanocomposite and random QD nanocomposite. For the InAs/GaAs system, QD dimensions and spacing for 1D chain are L_x=10nm, L_y=L_z=5nm and H_x=5nm. For the Ge/Si QD system, QD dimensions and spacing are L_x=L_y=L_z=4nm and H_x=2nm. L_x,L_y,L_z are dot dimensions in x,y,z directions and H_x is dot spacing along the alignment direction.

The bulk doping is chosen to correspond to the value which gives a maximum power factor. The ionized impurity concentration in the QDs is then calculated using the Poisson equation. The maximum $S^2\sigma$ of the InAs/GaAs QD chain occurs at E_f=0.064 eV above the conduction band edge of bulk GaAs, which corresponds to a bulk doping concentration of approximately 5×10^{18} cm^{-3} [11]. For Ge/Si QDs, the maximum $S^2\sigma$ occurs at E_f=0.002 eV above the valence band edge of bulk Si, which corresponds to a bulk doping concentration of approximately 1×10^{19} cm^{-3}.

To compare the InAs/GaAs and Ge/Si systems, we plot the maximum $S^2\sigma$ of the nanocomposite divided by the maximum $S^2\sigma$ of the bulk (GaAs or Si), i.e. the "normalized" power factor, as a function of φ. This is shown in **Fig.** 3.6 for both multiple QD chain and random nanocomposites. Since the parallel conductor model does not include interactions between the bulk and QD chains or between neighboring QD chains, the nanocomposite electrical conductivity ($\sigma_{nanocomposite}$) and Seebeck coefficient ($S_{nanocomposite}$) can be written as:

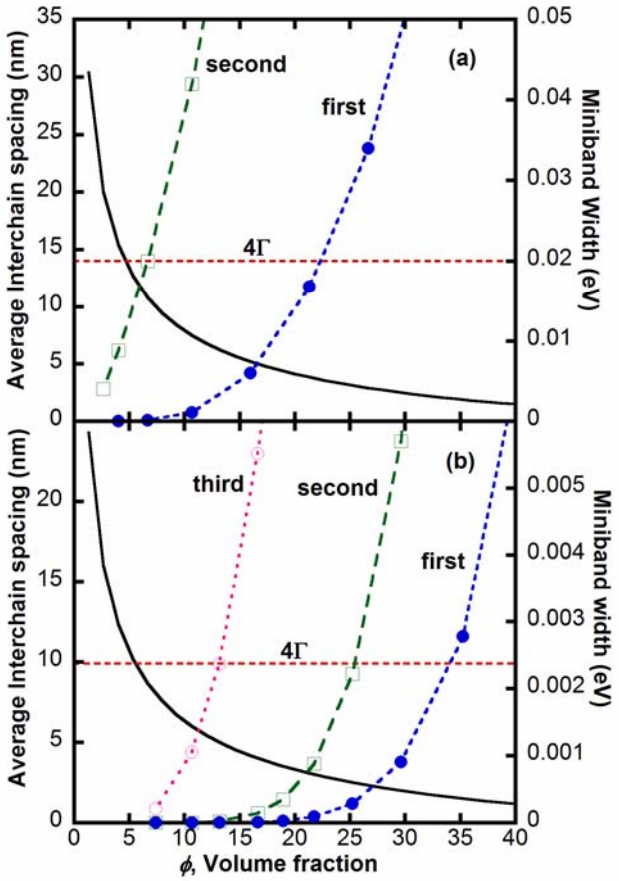

Figure 3.7. The average interchain spacing (solid line) is plotted on left axis and miniband widths (dotted lines) and 4 times the scattering potential (dotted line) are plotted on right axis as a function of the QD volume fraction. **(a)** The first and second minibands widths are plotted for InAs/GaAs dot chains with size and spacing as in **Fig.** 3.6. **(b)** The first, second and third minibands widths are plotted for Ge/Si dot chains with size and spacing as in **Fig.** 3.6.

$$\sigma_{nanocomposite} = \sigma_{chain}\varphi_{chain} + \sigma_{bulk}\left(1-\varphi_{chain}\right) \tag{3.20}$$

$$S_{nanocomposite} = \frac{S_{chain}\sigma_{chain}\varphi_{chain} + S_{bulk}\sigma_{bulk}\left(1-\varphi_{chain}\right)}{\sigma_{chain}\varphi_{chain} + \sigma_{bulk}\left(1-\varphi_{chain}\right)} \tag{3.21}$$

Here, σ_{chain} and S_{chain} (σ_{bulk} and S_{bulk}) are the electrical conductivity and Seebeck coefficient of the QD chain (bulk) corresponding to the maximum in power factor of the

QD chain (bulk), shown by the triangles in **Fig.** 3.5 (c). $\varphi_{chain} = \varphi \times (L_x + H_x)/L_x$ is the volume fraction of QD chains. From Equation (3.20), it is evident that the $\sigma_{nanocomposite}$ is linearly dependent on φ. Due to the similarities in S for the bulk and QD chain, $S_{nanocomposite}$ has a weak dependence on φ. Hence, for the multiple QD chain nanocomposite, the normalized $S^2\sigma$ is linearly dependent on φ. For the random QD nanocomposite, $S^2\sigma$ varies linearly with φ for low φ. For high φ, percolation effects lead to saturation in $S^2\sigma$. For aligned QDs with $\varphi = 0.4$, the normalized $S^2\sigma$ increases by more than 300% (180%) compared to bulk InAs/GaAs (Ge/Si). This stands in stark contrast to the random QD nanocomposite, for which the normalized $S^2\sigma$ decreases with increasing φ due to the intrinsically lower $S^2\sigma$ of the QDs.

To achieve 1D transport along the chain, interactions between neighboring chains must be negligible. **Fig.** 3.7 plots the values of φ and interchain spacing (H_i) for which this assumption holds. As φ is increased, the spacing between QD chains is reduced. The different regimes of charge transport in confined systems can be described using the parameters of lateral interwell coupling ($\Delta/4$) and scattering potential ($\Gamma = \hbar/\tau$, where Δ is the miniband width and τ is the relaxation time) [47]. When $\Delta/4 << \Gamma$, there is negligible miniband transport along the lateral direction (i.e. between the chains) [47]. In **Fig.** 3.7(a), for the InAs/GaAs system, H_i (left axis) and the first and second miniband widths in the lateral direction (right axis) are plotted as a function of φ. For comparison, 4Γ is also shown. For φ=0.06, corresponding to H_i=11 nm, miniband transport in the lateral direction commences, and the assumption of negligible transport between the chains is no longer valid. As shown in **Fig.** 3.6, H_i=11 nm corresponds to an increase in power factor of 1.4x in comparison to the bulk. Similarly, for Ge/Si, H_i (left axis) and the first, second, and third miniband widths in the lateral direction (right axis) are plotted as a function of

φ. For the Ge/Si system, at φ=0.11 (corresponding to H_l=5 nm), miniband transport begins. It is important to note that for both material systems miniband transport in the lateral direction can also be suppressed by placing the chains randomly and destroying long range order. In this case, higher φ values can potentially be used to obtain higher $S^2\sigma$.

3.6 Comparison of QD chains with 3D ordered QD nanocomposites

In this section, we compare the thermoelectric properties of QD chains with those of a 3D ordered QDSL, i.e. a 3D array of equally-spaced QDs. We assume identical QD sizes for the QD chain and 3D ordered QDSL (L_x=L_y=L_z=10nm for InAs/GaAs and L_x=L_y=L_z=4nm for Ge/Si), and identical QD separations in the x direction (H_x=5nm for the QD chain, H_x=H_y=H_z=5nm for the QDSL for InAs/GaAs; H_x=2nm for the QD chain, H_x=H_y=H_z=2nm for the QDSL for Ge/Si). The miniband dispersion of the 3D ordered QDSL is calculated according to the method outlined in Refs. [37] and [48]. This method approximates the 3D confinement as three independent 1D quantum wells for which the miniband energies as a function of wavevectors in x, y, z directions, $E(k_x)$, $E(k_y)$, and $E(k_z)$, are calculated. The miniband dispersion for miniband n ($E^n(\mathbf{k})$), is then obtained by summing $E(k_x)$, $E(k_y)$, and $E(k_z)$. σ and S are then calculated by integrating over **k** space as shown below:

$$\sigma = \frac{q^2\tau}{4\pi^3}\sum_n \int_{-\frac{\pi}{L_z+H_z}}^{\frac{\pi}{L_z+H_z}} \int_{-\frac{\pi}{L_y+H_y}}^{\frac{\pi}{L_y+H_y}} \int_{-\frac{\pi}{L_x+H_x}}^{\frac{\pi}{L_x+H_x}} \mathrm{v}_{\mathrm{x}}^{\mathrm{n}}(\mathbf{k})^2 \left(-\frac{\partial f_0}{\partial E^n(\mathrm{k})}\right) dk_x dk_y dk_z \qquad (3.22)$$

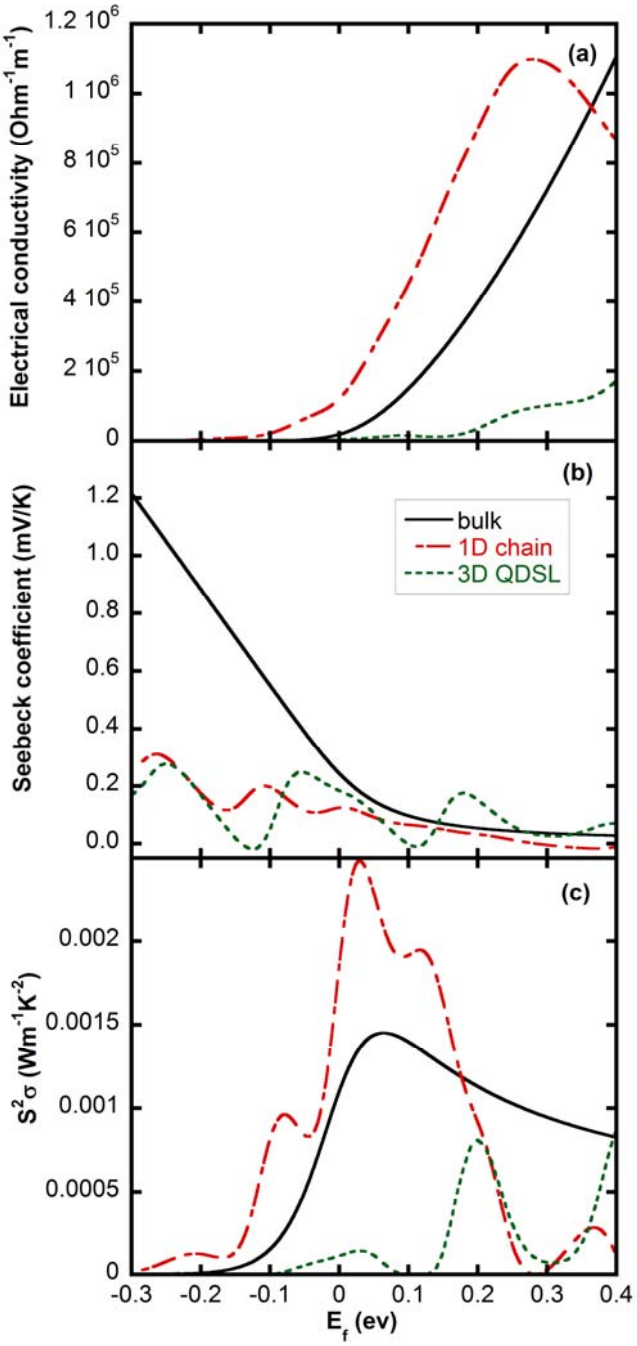

Figure 3.8. (a) Electrical conductivity, **(b)** Seebeck coefficient, and **(c)** power factor as a function of Fermi level for InAs/GaAs 1D QD chain with L_x= L_y= Lz=10nm and H_x=5nm, 3D QDSL with L_x= L_y= Lz=10nm and H_x= H_y= H_z=5nm, and bulk GaAs.

$$S = \frac{-1}{qT} \frac{\sum_n \int_{-\frac{\pi}{L_z+H_z}}^{\frac{\pi}{L_z+H_z}} \int_{-\frac{\pi}{L_y+H_y}}^{\frac{\pi}{L_y+H_y}} \int_{-\frac{\pi}{L_x+H_x}}^{\frac{\pi}{L_x+H_x}} \mathrm{v}_{\mathrm{x}}^{\mathrm{n}}(\mathbf{k})^2 \left(E^n(\boldsymbol{k}) - E_f\right) \left(-\frac{\partial f_0}{\partial E^n(\boldsymbol{k})}\right) dk_x dk_y dk_z}{\sum_n \int_{-\frac{\pi}{L_z+H_z}}^{\frac{\pi}{L_z+H_z}} \int_{-\frac{\pi}{L_y+H_y}}^{\frac{\pi}{L_y+H_y}} \int_{-\frac{\pi}{L_x+H_x}}^{\frac{\pi}{L_x+H_x}} \mathrm{v}_{\mathrm{x}}^{\mathrm{n}}(\mathbf{k})^2 \left(-\frac{\partial f_0}{\partial E^n(\mathrm{k})}\right) dk_x dk_y dk_z} \tag{3.23}$$

where the summation is over *n* minibands. The electron group velocity is again given by Equation (3.19).

A comparison of σ, *S*, and $S^2\sigma$ for single QD chains, a 3D ordered QDSL, and the bulk are shown in **Figs.** 3.8(a), (b) and (c) (**Figs.** 3.9(a), (b) and (c)), for the InAs/GaAs (Ge/Si) system. σ of the QD chains is much higher than that of the bulk and the 3D QD SL, as shown in **Figs.** 3.8(a) and 3.9(a), presumably due to 1D transport along the chains. The lower σ for the 3D QD SL in comparison with that of the bulk, even above (below) the conduction (valence) band edges, is likely due to the lower density of states for the QD SL in comparison to the bulk. For both QD chains and the 3D QD SL, *S* is smaller than that of the bulk for Fermi levels below (above) the band edge, presumably due to the presence of minibands below (above) the band edge in the bulk, as shown in **Figs.** 3.8(b) and 3.9(b). As the Fermi level moves through the minibands, oscillations in *S* and σ are observed, similar to those observed in Section III for the case of the 1D QD chain.

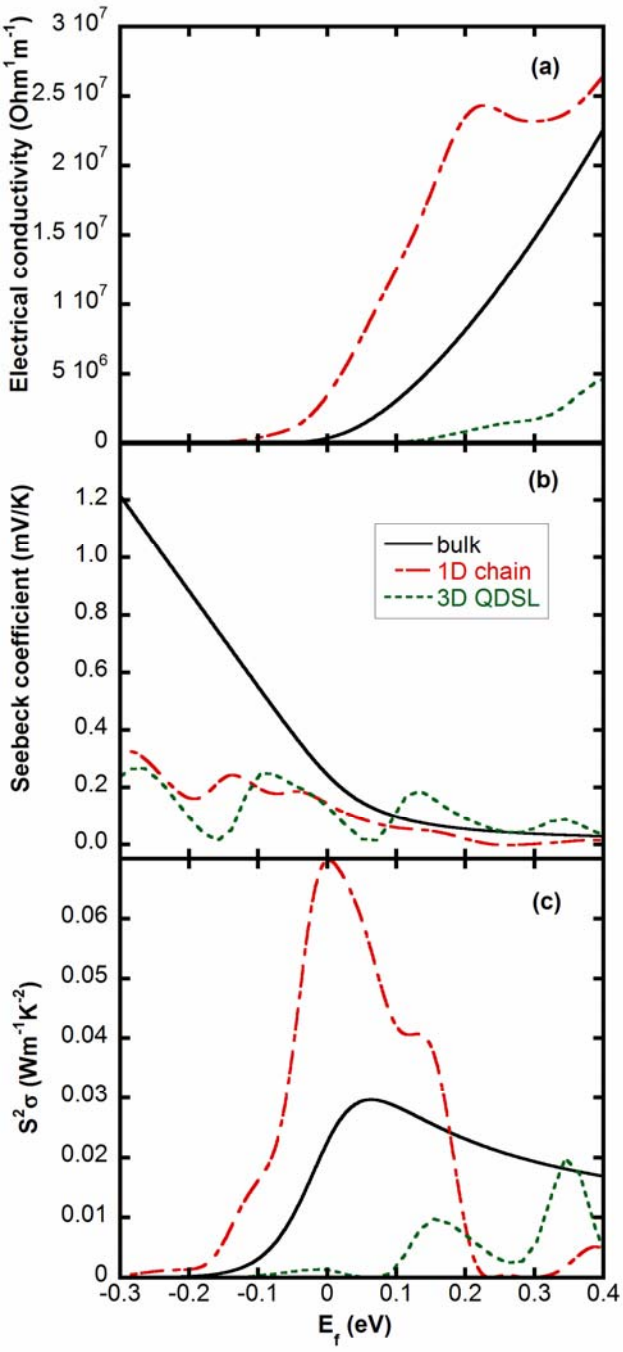

Fig. 3.9. (a) Electrical conductivity, **(b)** Seebeck coefficient, and **(c)** power factor as a function of Fermi level for Ge/Si 1D QD chain with L_x= L_y= Lz=4nm and H_x=2nm, 3D QDSL with L_x= L_y= L_z=4nm and H_x= H_y= H_z=2nm, and bulk Si.

Figures 3.8(c) and 3.9(c) present $S^2\sigma$ values as a function of Fermi level for InAs/GaAs and Ge/Si systems. For the 1D QD chain, $S^2\sigma$ is significantly enhanced with respect to

the 3D ordered QDSL and bulk, due to the higher σ in the 1D QD chain case. For the 3D QDSL, due to its low σ, $S^2\sigma$ is not enhanced even with respect to the bulk.

As H_i (φ) is decreased (increased), the interaction between neighboring chains (interwell coupling $\Delta/4$) is enhanced. At a critical H_i, (given by $\Delta/4 > \Gamma=\hbar/\tau$) there is a transition from localized carrier transport through QD chains to delocalized carrier transport in all three directions, as shown in **Fig.** 3.7. In Ref. [23], a 3D ordered QDSL with carrier transport coupled to all 3 directions through the minibands was likewise investigated numerically. In both 3D cases (here and Ref. [23]), insignificant increases in the $S^2\sigma$ with respect to the maximum $S^2\sigma$ in the bulk were predicted. For the 1D QD chains, however, as shown in **Figs.** 3.8 and 3.9, $S^2\sigma$ is predicted to be much higher than that of either a 3D QDSL or the bulk.

3.7 Summary and Conclusions

We have investigated the thermoelectric properties of aligned QD chains and QD chain nanocomposites in the InAs/GaAs and Ge/Si systems. Using the Schrödinger and Boltzmann transport equations, we calculated the miniband dispersion and resulting transport properties S and σ. A comparison of the properties of single QD chains with those of the corresponding bulk reveals higher $S^2\sigma$ values for both Ge/Si and InAs/GaAs systems, presumably due to the 1D confinement along the chain length which increases σ. Additionally, in both cases, $S^2\sigma$ of the QD chains increases with decreasing QD size. The incorporation of the QD chains into a matrix leads to a reduced $S^2\sigma$ in comparison with single QD chains, due to parallel conduction through the matrix; however, an increase in $S^2\sigma$ compared with both the random QD composite and the corresponding bulk is observed. An increase in thermoelectric power factor by a factor of 3 (1.5) for the

InAs/GaAs (Ge/Si) system with respect to bulk is demonstrated. The power factor of a 1D QD chain is shown to be much higher than that of 3D ordered QDSL with similar QD sizes and spacings. The limitations of our model were assessed in terms of the minimum (maximum) H_i (ϕ) for which 1D conduction through the chains occurs without lateral inter-chain coupling. Overall, we show that the 1D nature of conduction in the minibands can be exploited to yield a thermoelectric enhancement similar to that predicted for nanowires and nanowire superlattices, but without the practical difficulties associated with these structures. This improved thermoelectric performance using aligned QD chains is a general concept which could be applied to many material systems to yield high energy conversion efficiencies.

Chapter 4

Integrated Thermoelectric Coolers for Mercury Cadmium Telluride Based Infrared Detectors

4.1 Introduction

Mercury cadmium telluride (MCT) is an alloy of semimetal mercury telluride (E_g=-0.01 eV) and semiconductor cadmium telluride (E_g=1.5 eV) [49]. By alloying the two in various compositions ($Hg_{1-x}Cd_xTe$), the bandgap can be controlled between 0 and 1.5 eV. It has a direct energy gap, high mobility, and low dielectric constant, making it suitable for many optoelectronic applications such as infrared photodetectors. Specifically, at x~0.2 the bandgap is matched to long wave infrared (LWIR) light which is detected in thermal imaging applications such as night vision [49]. MCT has very low electron effective mass [50], resulting in low scattering rates and very high mobility and electrical conductivity. The thermal conductivity of bulk MCT is very small [50] (< 4 W/mK at 300K) and decreases with increasing cadmium concentration. However, the density of electron states is also low, leading to a smaller Seebeck coefficient than many other semiconductors and poor thermoelectric performance in spite of its high electrical mobility and low thermal conductivity.

Small-barrier [51] and high-barrier [52, 53] quantum well (QW) superlattices (SLs) have been proposed to improve the ZT of MCT. If MCT with high ZT were developed, it could be used as a monolithically integrated cooler material for infrared photodetector pixel elements. Such coolers have potential for dramatically reducing the pixel operating temperature, leading to greatly reduced noise. Recognizing that the cross-plane thermoelectric properties of MCT SLs are much better than their in-plane properties (this direction also being more convenient for monolithic integration with pixel elements), we concentrate in this chapter on the measurement of cross-plane Seebeck coefficient and thermal conductivity of small-barrier MCT SLs fabricated by EPIR Technologies, Inc. (Bolingbrook, IL).

4.2 Cross-plane Seebeck coefficient and thermal conductivity of small-barrier $Hg_{1-x}Cd_xTe$ superlattices

Nanostructuring electronic materials can lead to anisotropic thermal and electrical properties due to quantum confinement effects and scattering at interfaces [4, 31]. 1D nanostructured materials, such as quantum well superlattices have different thermal and electrical properties in the direction of growth (cross-plane direction) and in the plane of growth (inplane direction) [31]. In this chapter, we will concentrate on measurement of cross-plane thermal conductivity and Seebeck coefficient of small barrier HgCdTe superlattices.

4.2.1 Measurement of Seebeck coefficient and thermal conductivity of thin films

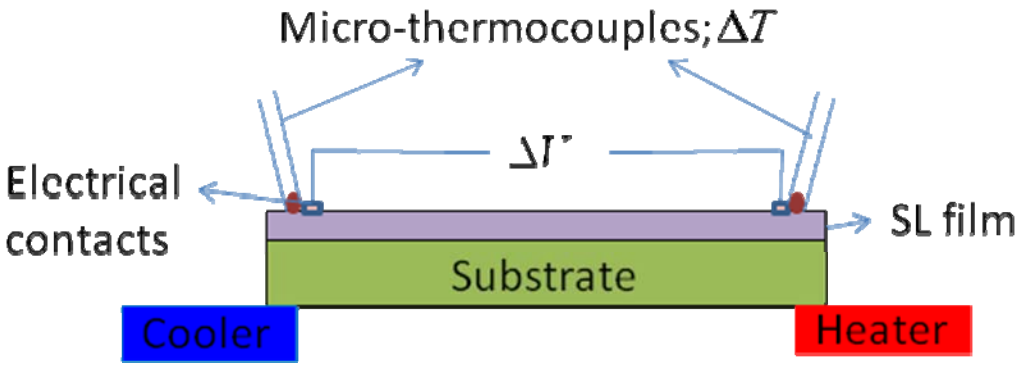

Figure 4.1. Setup for in-plane Seebeck coefficient measurement

Measurement of the Seebeck coefficient requires simultaneous measurement of temperature difference applied and thermoelectric voltage induced across a material. **Figure** 4.1 shows a setup which can be used for this purpose. The sample is placed such that one side sits on a heater and the other side sits on a cooler. The temperature on each side is measured using a microthermocouple, and the open circuit voltage is measured using a digital multimeter. The Seebeck coefficient is then given by:

$$S = -\frac{\Delta V}{\Delta T} \tag{4.1}$$

This simple method is effective in measuring the in-plane Seebeck coefficient of thin films (such as superlattices) if the substrate is electrically insulating. If the substrate is not electrically insulating, it will contribute to the net Seebeck coefficient developed. But, an approximate Seebeck coefficient of the thin film can be calculated if the Seebeck coefficient and electrical conductivity of the substrate and the electrical conductivity of the thin film are known. In-plane thermal conductivity of a thin film can also be measured using the setup of **Fig.** 4.1, but the rate of heat transfer must be accurately measured and convection effects must be taken into account. To measure the cross-plane

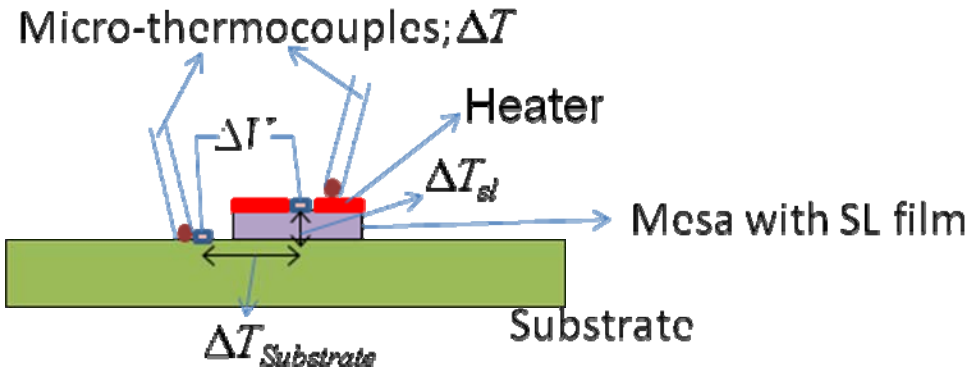

Figure 4.2. Illustration of setup for cross-plane Seebeck coefficient measurement.

Seebeck coefficient, a temperature gradient must be applied perpendicular to the film and voltage must be measured across the film. Most thin films are grown epitaxially on a thick substrate; fabricating free-standing thin films with electrodes on either side is not usually practical.

An alternative is to create mesa geometry for the thin film and measure the temperature difference and voltage induced between the top of the mesa and a location near the bottom of the mesa, as shown in **Fig.** 4.2. A heating wire has to be fabricated on top of mesa to heat the top surface. A one dimensional heat transfer through the mesa can be achieved if a serpentine heating wire is fabricated on the mesa to uniformly heat it. If a line heater is used, then heat spreading inside the mesa has to be taken into account. In this case, the measured Seebeck coefficient contains contributions from both the thin film and substrate. The measured thermoelectric voltage and temperature can be written as:

$$\Delta T = \Delta T_{film} + \Delta T_{substrate} \tag{4.2}$$

$$\Delta V = S_{film}\Delta T_{film} + S_{substrate}\Delta T_{substrate} \tag{4.3}$$

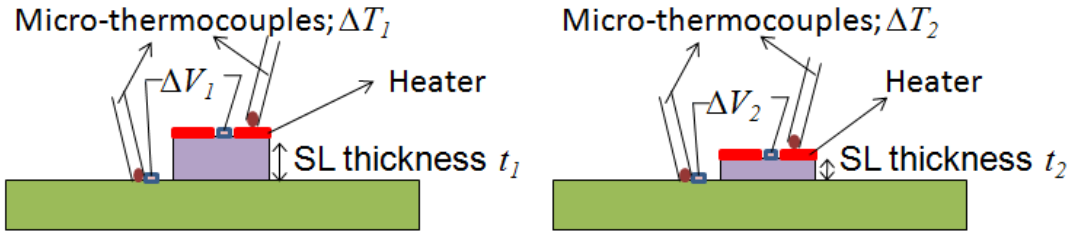

Figure 4.3. Illustration of differential method for cross-plane Seebeck coefficient and thermal conductivity measurement

To obtain the superlattice Seebeck coefficient, both ΔT_{film} and $\Delta T_{substrate}$ must be determined. Comparison to a FEM simulation can be used for this purpose. However, for accurate computation, the convective heat transfer must be taken into account. This method has been used to measure the cross-plane Seebeck coefficient and thermal conductivity of InGaAS/InGaAlAs superlattices [54].

A more reliable method to calculate the SL Seebeck coefficient and thermal conductivity is to use differential measurement of two samples with the same microfabricated structure but different SL thicknesses [55-57], as shown in **Fig.** 4.3. This does not require accurate determination of the heat transfer coefficient or any FEM simulation. The temperature difference and thermoelectric voltage are measured as a function of power applied to the heater for both samples, and the cross-plane Seebeck coefficient and thermal conductivity of the superlattice can then be written as:

$$S_{sl} = \frac{\Delta V_1 - \Delta V_2}{\Delta T_1 - \Delta T_2} \tag{4.4}$$

$$k_{sl} = \frac{P \times (t_2 - t_1)}{A(\Delta T_2 - \Delta T_1)} \tag{4.5}$$

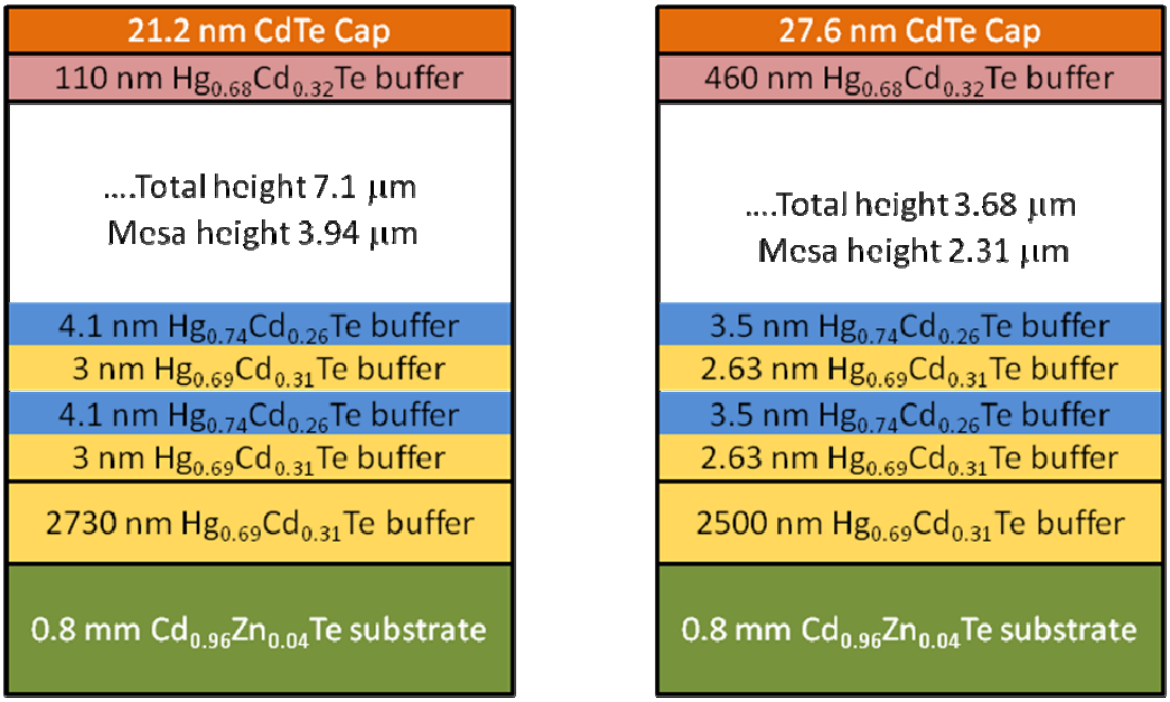

Figure 4.4. Schematic of SL structure used for measurement

where P is the power applied to the heater, ΔV_1 and ΔV_2 are the thermal voltages measured between the top and bottom of the two mesas, ΔT_1 and ΔT_2 are the temperature differences measured between the top and bottom of the two mesas, t_1 and t_2 are the thicknesses of the two superlattices, and A is the mesa area. This measurement method assumes a one-dimensional heat flow from the top of the mesa to bottom, which is valid if the size of the mesa is small compared to the heating wire or if the heating is uniform. Another assumption in this measurement technique is that the configuration of thin films, i.e., the doping and thickness of each layer, if the film is a superlattice, has to be the same.

Two samples with mesas measuring 450×450 µm^2 and SL thicknesses of 3.94 µm (sample 1) and 2.31 µm (sample 2) were fabricated by EPIR Technologies, Inc. and used for measurement. The sample structures, shown in **Fig.** 4.4, are doped at 2.5×10^{16} cm^{-3}

and 6.4×10^{16} cm^{-3} respectively. There is a small difference in the thickness of each layer, and the thickness of capping and buffer layers, which can generate an error in measurement. A serpentine thin film gold wire heater was fabricated on top of the mesa, as shown in **Fig.** 4.5. Two gold wires are used to pass current through the microfabricated surface heater, while two other gold wires are used to measure the induced thermoelectric voltage between the top contact and bottom contact. Because of the low thermal conductivity of HgCdTe, it is difficult to maintain stable temperatures even over small areas if a heat sink is not used. Hence, all measurements were done with samples mounted on a heat sink at 19 °C. A microthermocouple is used to measure the average temperature on the top and side contacts. The temperature difference (ΔT) and voltage

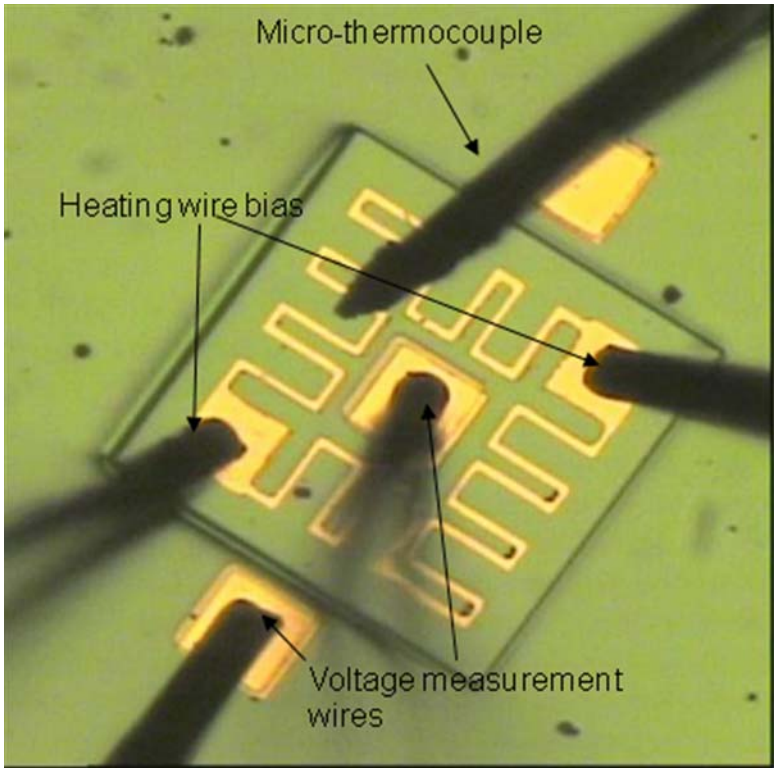

Figure 4.5. Measurement setup

drop (ΔV) between the mesa top and side contact are measured as a function of power applied to the heater. Because the SL layer is thicker for Sample 1, a larger ΔT develops for the same power applied to the heater, giving rise to a larger thermal voltage ΔV.

4.2.2 Results and discussion

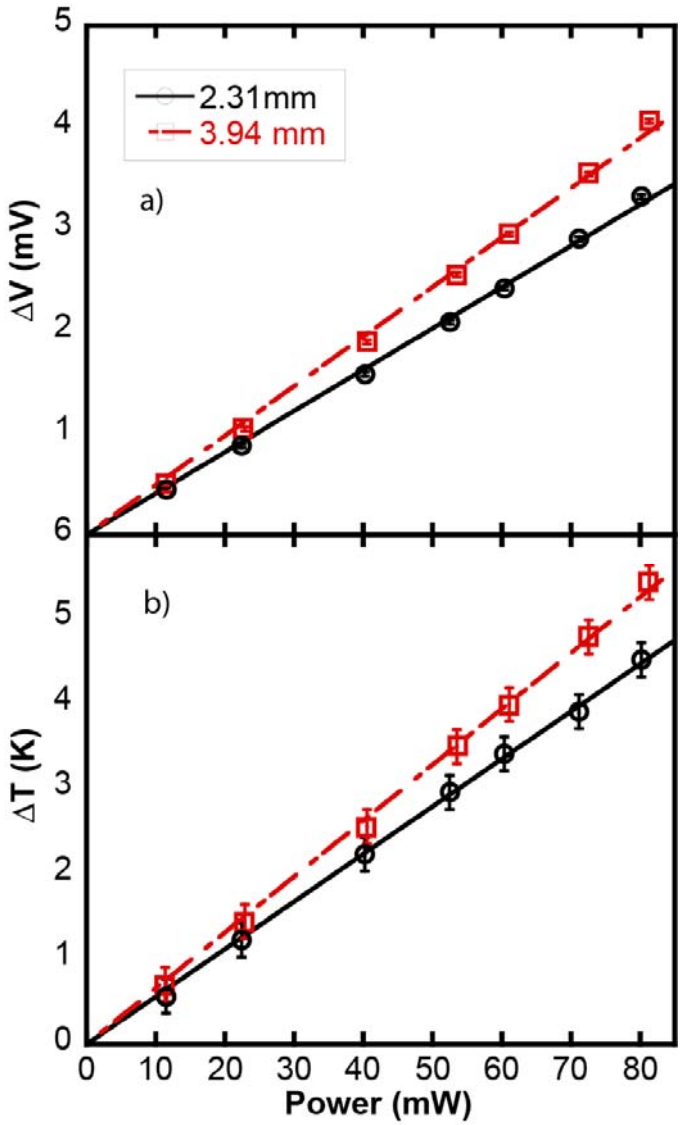

Figure 4.6. (a) Thermoelectric voltage developed and **(b)** Temperature difference between top and bottom edge of mesa as a function of power applied to the heater.

The measured temperature difference and thermoelectric voltage as a function of power

applied to the heater are shown in **Figs.** 4.6. Recognizing the linear nature of the Seebeck coefficient reflected in Equation (4.1), linear curves are fit to the ΔT vs. power and ΔV vs. power curves, yielding the following equations:

$$\Delta T_2 = (65.66 \pm 0.453) \times P \tag{4.6}$$

$$\Delta V_2 = (48.66 \pm 0.48) \times P \tag{4.7}$$

$$\Delta T_1 = (55.846 \pm 0.361) \times P \tag{4.8}$$

$$\Delta V_1 = (40.54 \pm 0.32) \times P \tag{4.9}$$

The slope of ΔT vs. power gives the thermal resistance. The cross-plane thermal conductivity is then given by:

$$R_{th,2} - R_{th,1} = \frac{t_2 - t_1}{kA} \tag{4.10}$$

where R_{th} is the thermal resistance, A is the mesa area, t is the SL thickness, and k is the cross-plane thermal conductivity to be calculated. The Seebeck coefficient was similarly obtained as the ratio of voltage difference to temperature difference. A thermal conductivity of 0.82±0.07 W/mK and Seebeck coefficient of 811±150 μV/K were measured. Although the error in individual measurement is small (0.2 K for ΔT and 0.02 mV for ΔV), this error is amplified when taking the difference ΔT or ΔV between the samples because of very small difference in thickness between the samples. Hall measurements were used to measure the resistivity of a sample with superlattice configuration of 4.1 nm $Hg_{0.74}Cd_{0.26}Te$/3.5 nm $Hg_{0.68}Cd_{0.32}Te$ and doping of 3.03×10^{16} cm^{-3}. These measurements were done at EPIR Technologies, Inc. (Bolingbrook, IL) and a resistivity of 0.017 Ω.cm was obtained. From this value of resistvity, ZT is calculated to be 1.43 as compared to a maximum ZT of 0.33 for bulk $Hg_{1-x}Cd_xTe$ with $0<x<0.3$ and

doping<10^{19} cm^{-3} [58].

4.3 Design of integrated thermoelectric cooler

4.3.1 Design considerations

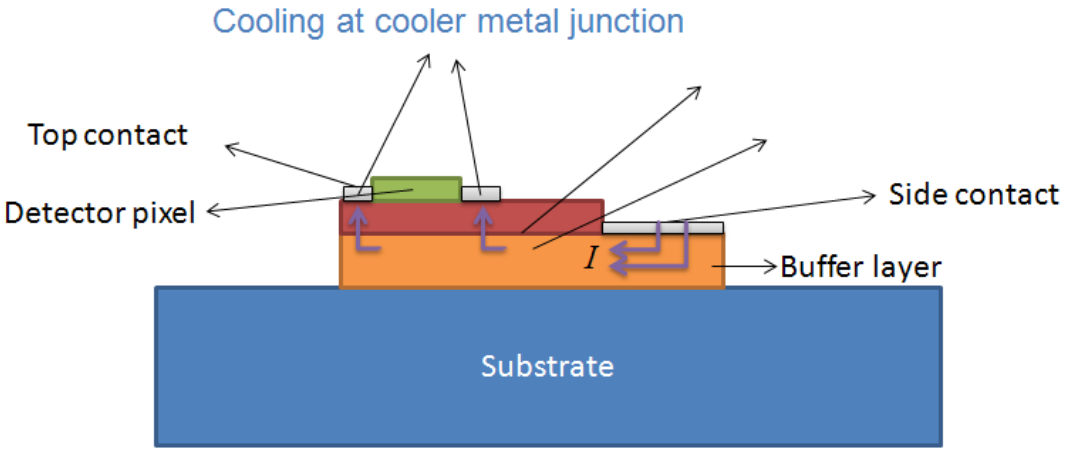

Figure 4.7. Proposed geometry of an integrated thermoelectric cooler for cooling infrared detector pixels.

Figure 4.7 shows a schematic of the proposed monolithically integrated thermoelectric cooler. Similar integrated coolers have been designed for p-n diodes [59], InGaAsP laser diodes [60], and, GaAs/AlGaAs vertical-cavity surface emitting laser diodes [61]. A $Cd_{0.3}Zn_{0.7}Te$ buffer layer is first deposited on the CdTe substrate for carrier injection. HgCdTe superlattices are then epitaxially grown on top of the buffer layer. Since thermoelectric cooling is an interface effect, the contact where heat is rejected should be as far away from the detector pixel as possible in order to prevent heat from flowing back to the pixel. For *n*-type semiconductors, the contact where current is injected is hot while the other contact is cold. Hence in the proposed configuration the integrated cooler current is injected from the side contact.

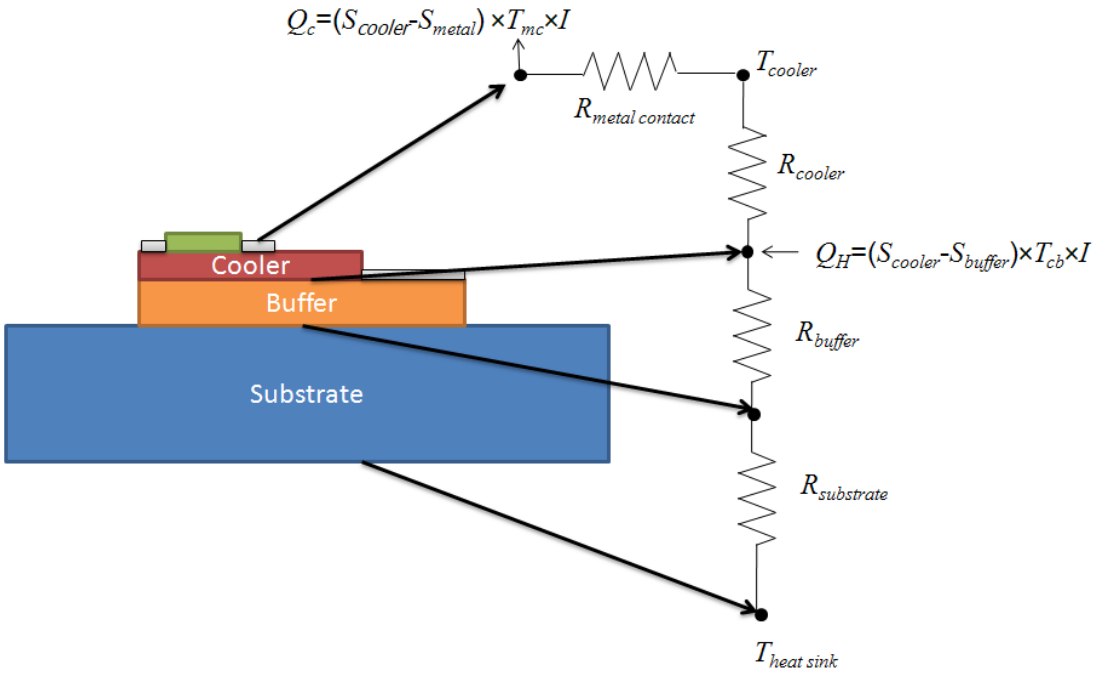

Figure 4.8. Illustration of multilayer thermal resistances. Also shown are the locations of Peltier heating and cooling.

Figure 4.8 shows the thermal resistances of the different layers which affect heat conduction. If the buffer is highly doped, then Peltier heating mainly happens at the cooler-buffer interface. A low-doped buffer can move the Peltier heating to the buffer-side contact interface but will also lead to higher Joule heating and nonuniform current injection into the cooler because of shorter current paths to cooler edge near side contact. From **Figure** 4.8, it is clear that R_{cooler} must be maximized to prevent Q_h from flowing back to the pixel, and R_{buffer}+$R_{substrate}$ must be minimized to make Q_h flow efficiently to the bottom of substrate where it can be removed by the heat sink.

4.3.2 Coupled electrothermal modeling

The coupling of heat transfer and electric current in thermoelectric materials can be described by the Seebeck and Peltier coefficients through constitutive equations [62]:

$$\vec{q} = \Pi\vec{j} - k\nabla T \tag{4.11}$$

$$\vec{j} = \sigma\vec{E} - \alpha\nabla T \tag{4.12}$$

where $\vec{q}$ and $\vec{j}$ are the electric and heat current densities, Π is the Peltier coefficient, α is the seebeck coefficient, T is the absolute temperature, and $\vec{E}$ is the electric field. The governing equations for heat and electric charge current can be written as [62]:

$$\rho C\frac{\partial T}{\partial t} + \nabla.\vec{q} = \dot{q} \tag{4.13}$$

$$\nabla.\left(j + \frac{\partial \vec{D}}{\partial t}\right) = 0 \tag{4.14}$$

where ρ is the density, C is the specific heat capacity, and D is the electric flux density vector defined by:

$$\vec{D} = \varepsilon\vec{E} \tag{4.15}$$

The solution of Equations 3.11-3.15 is accomplished using the commercially available FEM software ANSYS. **Figures** 4.9 (a) and (b) show an ANSYS drawing and associated mesh of the substrate, buffer layer, cooler layer, and detector pixel. Meshing is done

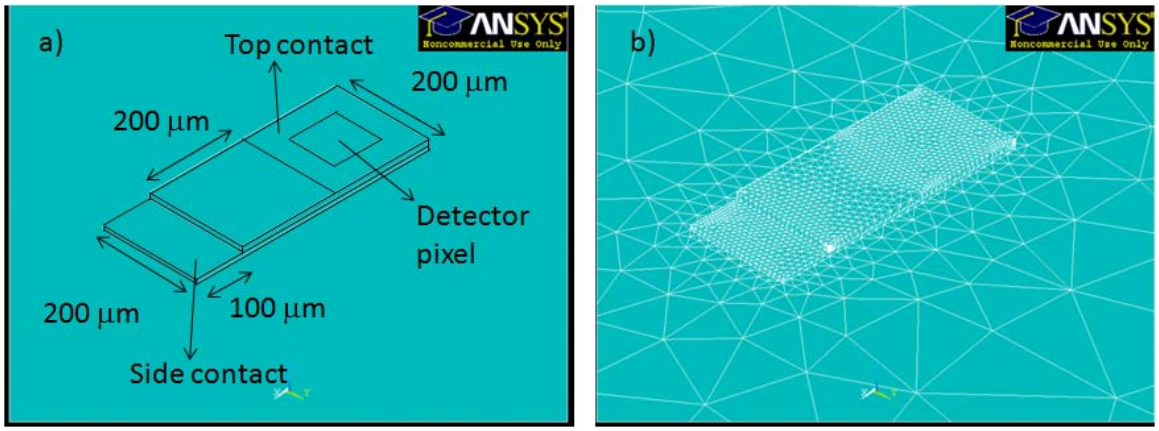

Figure 4.9. (a) ANSYS drawing of cooler and detector pixel mesa **(b)** 3D meshing of all layers.

using 3D 10 node tetrahedron elements (SOLID227). The heat transfer boundary conditions specify free convection at all surfaces except the bottom surface, which is heat sunk at 19°C. The heat transfer coefficient for free convection from microelectronic devices has been measured upto a value of 84000W/m^{2}K [63]. Here we take a conservative value of heat transfer coefficient of 100 W/m^{2}K and the ambient temperature as 19°C. The electrical boundary conditions are specified as uniform voltage at the contacts. The substrate and detector pixel are assumed to be electrically insulating for simplicity.

4.3.3 Results and discussion

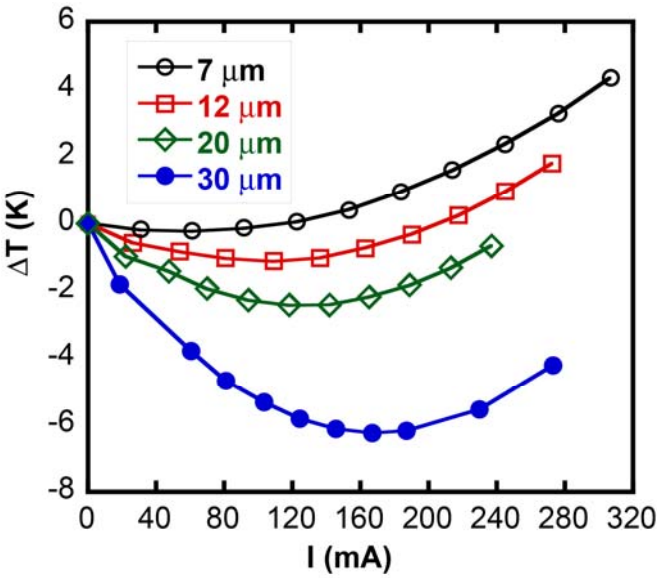

Figure 4.10. The average temperature drop on detector pixel surface. $t_{substrate}$ = 800μm and t_{buffer} = 8μm.

Figure 4.10 shows the temperature drop of the detector pixel surface with respect to the ambient temperature of 19°C. The simulation is done for a substrate thickness $t_{substrate}$ of 800μm and a buffer layer thickness t_{buffer} of 8μm which are typical values for epitaxially grown samples [64]. With an increase in thickness of the cooler, a larger

reduction in temperature of pixel surface is seen. The peak in cooling shifts to higher currents, as a thicker cooler leads to a larger electrical resistance. Similar results are shown in **Fig.** 4.11 (a) for a substrate thickness of $t_{substrate}$ of 30μm and a buffer layer thickness t_{buffer} of 5μm. Although, above mentioned values are not typical for epitaxially grown samples, thinner substrates can be obtained by polishing the backside of wafer. An increase in the maximum cooling with an increase in cooler thickness is again seen. The current at which maximum cooling occurs increases with cooler thickness initially, and then decreases due to an increase in joule heating. **Figure** 4.11 (b) shows the maximum cooling as a function of cooler thickness. A linear relation is obtained between the maximum cooling and cooler thickness due to one dimensional heat transport in the cooler.

Figure 4.12 (a) shows the effect of substrate thickness on pixel cooling. With an increase in substrate thickness, the cooling is reduced, with the current at which

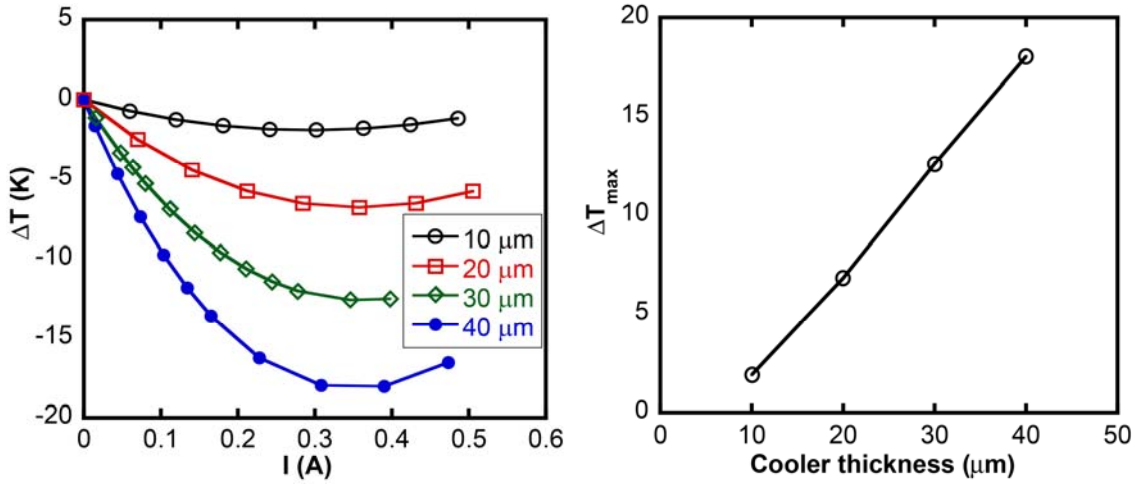

Figure 4.11. (a) The average temperature drop on the detector pixel surface, assuming $t_{substrate}$ = 30 μm and t_{buffer} = 5μm. **(b)** Maximum cooling as a function of cooler thickness.

maximum cooling occurs becoming smaller. An increased substrate thickness provides higher thermal impedance to the flow of heat from the cooler-buffer interface and Joule heat to the heat sink at the bottom. **Figure** 4.12 (b) shows the maximum cooling as a function of substrate thickness. The cooling does not vary linearly because of heat spreading in the substrate. Hence, beyond a threshold value of substrate thickness, further increase in the thickness of the substrate leads to minimal reduction in maximum cooling. This threshold value of substrate thickness is dependent on the substrate thermal conductivity as well as the thermal resistances of the buffer and cooler layers and the heat transfer coefficient.

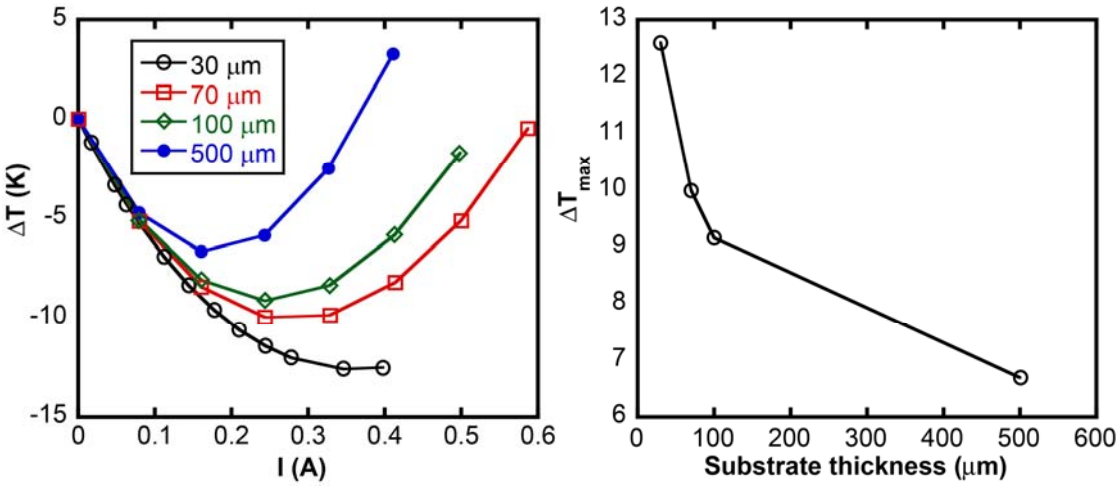

Figure 4.12. (a) The average temperature drop on the detector pixel surface as a function of substrate thickness, assuming t_{cooler}= 30 μm and t_{buffer} = 5μm. **(b)** Maximum cooling as a function of substrate thickness.

4.4 Summary and conclusions

In this chapter, the feasibility of using integrated solid state coolers for cooling mercury cadmium telluride based superlattice detectors has been investigated. Using a steady state

differential measurement, the cross-plane Seebeck coefficient and thermal conductivity of small barrier HgCdTe superlattices were measured, finding a Seebeck coefficient of 811±150 μV/K and a thermal conductivity of 0.82±0.07 W/mK. Assuming an electrical resistivity of 0.017 Ω·cm (obtained from Hall measurements), a ZT value of 1.43 is obtained, as compared to ZT of 0.33 for bulk $Hg_{1-x}Cd_xTe$ with $0<x<0.3$ and doping$<10^{19}$ cm^{-3}. This increase in ZT is attributed to an increase in the Seebeck coefficient as well as a decrease in thermal conductivity. Although a ZT of 1.43 is still small for solid state heat engines or heat pumps to compete with mechanical heat engines and heat pumps, it shows a promising trend of using nanostructed HgCdTe superlattices for high efficiency thermoelectrics.

Using the obtained values of Seebeck coefficient and thermal conductivity, we use FEM simulation to design a thermoelectric cooler monolithically integrated with an infrared detector pixel. An integrated cooler can help in reducing local hot spots, and effectively pumping heat from active device area in a chip, such as infrared detector pixel in a focal plane array, to the parts of chip which are not utilized in active devices such as substrate. We find a general trend of higher cooling with thinner substrates and thicker cooler layers. The cooling on pixel surface increases linearly with cooler thickness demonstrating a one dimensional heat transfer in the cooler. With an increase in thickness of substrate, the cooling decrease in a non linear fashion because of heat spreading in the substrate.

Chapter 5

Fiber-based flexible thermoelectric power generator

5.1 Introduction

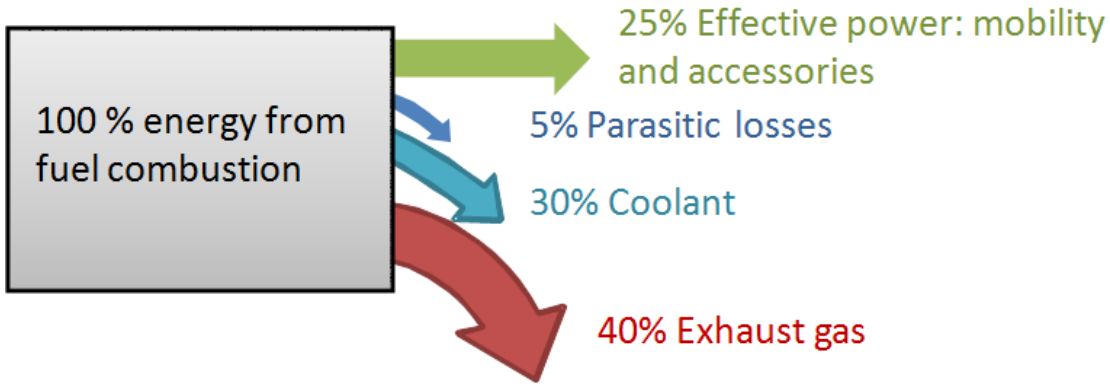

Figure 5.1. Distribution of power produced in an internal combustion. Only ~35% of the power produced is utilized, with the rest dissipated mainly as heat [65].

Thermoelectric (TE) power generators can potentially be used to improve the efficiencies of mechanical and electrical devices by converting waste heat to electrical power. For example, in an internal combustion engine, only about 35% of the energy produced from combustion is converted into useful work, with the rest being dissipated as heat in the engine body or exhaust [65]. TE generators are typically fabricated from

crystalline semiconductors such as Bi_2Te_3 or SiGe, making them rigid and unsuitable for covering large areas or arbitrary shapes that are commonly encountered in waste heat recovery applications. In order to improve thermal contact to heat sources of arbitrary geometry, it is desirable to produce thermoelectric generators that can conform easily to a surface. However, thermoelectric devices based on flexible materials such as organic semiconductors have proven impractical to date due to low ZT stemming from low electrical carrier mobility [66]. Another idea is to embed discrete miniature TE chips in a flexible matrix; however, such systems are not easy or inexpensive to manufacture and may be hampered by their reliability [20].

A more desirable configuration is one in which intrinsically flexible thermoelectric devices are fabricated in an inexpensive reel-to-reel process. Flexible photovoltaic cells [67] and organic light emitting diodes (OLEDs) [68] have been fabricated by depositing thin films on flexible substrates or fibers [69, 70]. In addition, miniaturization of energy conversion devices is being pursued to operate low power electronics using readily available energy sources such as human body heat [71] or heel strikes during walking [71].

Previous work in flexible thermoelectric power generators has involved fabrication of multiple thermocouple junctions on flexible planar substrates. Itoigawa et al. [72] used a wavy polyimide sheet with junctions at the top and bottom of the sheet to build a flexible thermopile. Sato et al [73] used a combination of copper and polyimide sheets as a flexible substrate to create an in-plane temperature gradient from a cross-plane heat flux. These techniques require photolithography and precision machining, however, and their flexibility is limited to a single plane and constrained by the thickness of the substrate. Here we demonstrate a flexible thermoelectric generator based on thin-film

thermoelectric junctions on flexible fibers. These fibers can be woven into energy-harvesting fabrics or interwoven with structural fibers such as carbon fibers to create an energy-harvesting composite. We deposit thin films using vacuum thermal evaporation, a technique which has been shown to be amenable to scale up in a high-throughput reel-to-reel fashion for the fabrication of devices such as thin-film solar cells and organic LEDs, and metallization of food packaging plastics and other low-cost applications. To prevent abrasion of the thermoelectric coating or electrical shorting, the fibers can easily be coated with a light-weight plastic barrier film, either by calendaring or by chemical vapor deposition [74]. Weaving techniques used in common textiles or those specifically developed for electronic textiles [75] can be used to establish robust parallel and series electrical interconnects.

5.2 Materials and processes for flexible thermoelectric devices

Figure 5.2 shows different materials which can be used to make flexible substrates/devices. For example, metal wires or sheets can be used as a substrate for

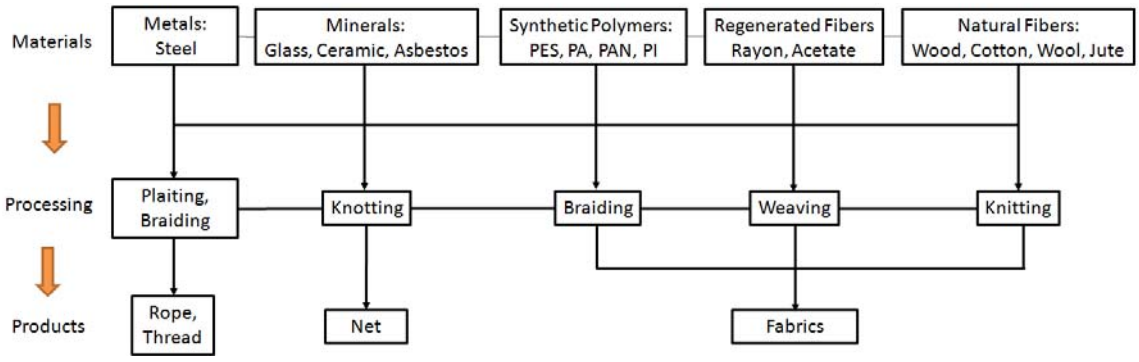

Figure 5.2. Materials and processes used for producing different textile products. The abbreviations are: PES is polyester, PA is polyamide (nylon), PAN is polyacetonitrile and PI is polyimide.

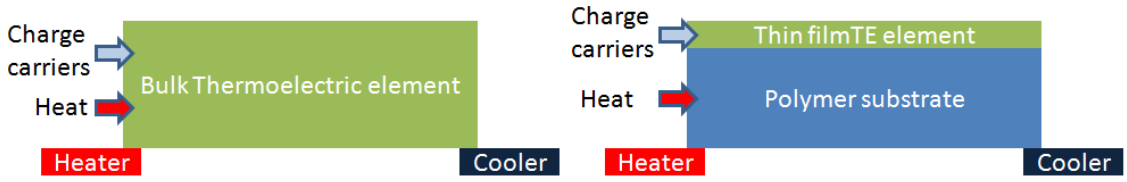

Figure 5.3. (a) Bulk thermoelectric device (b) TE generator with thermoelectric element fabricated on a flexible polymer substrate

flexible thermoelectric devices, but since they have large thermal conductivities (on the order of 100 W/mK), they can require a large heat sink or very long segment lengths in order to achieve a large enough temperature difference between the hot and cold ends of the thermocouples. Polymers have very low thermal conductivity (<1W/mK), and may be suitable candidates for compact, flexible thermoelectric generators. Polymers can be distinguished into 3 main categories: 1) natural, 2) synthetic, and 3) regenerated or semi-synthetic. Minerals such as glass and asbestos can also be drawn into fibers which have low thermal conductivity.

The thermoelectric element can be thin films of metals or polycrystalline semiconductors, which may be fabricated by a number of thin film deposition techniques including thermal evaporation, sputtering, electroless plating, and electrodeposition. An example device geometry is shown in **Fig.** 5.3 (b). While in a bulk TE generator (as shown in **Fig.** 5.3(a)) both heat and charge carriers are carried in same material, in a thin film device the heat is mainly carried by the electrically insulating substrate. As a result, a very large temperature gradient can be established if a polymer substrate is used.

The substrate material can be processed in different ways to yield fabrics, sheets, or threads/ropes. A TE generator requires that the two ends of the thermocouple be at different temperatures. For TE generators cooled by natural convection, the distance

between the cold junction and the hot surface must be maximized. A woven fabric in plain weave geometry is a suitable candidate for achieving this. A plain weave consists of two sets of fibers (the warp and weft) which are perpendicular to each other and go over and under consecutive fibers as shown in **Fig.** 5.4(a). A shuttle loom (as shown in **Fig.** 5.4(b)) is often used to produce woven fabrics [76]. The warp fibers are held parallel to each other, with alternate fibers being picked up. The weft fiber is attached to shuttle which is passed perpendicular to the warp fibers. Finally, the reed which picks alternate warp fiber is lowered.

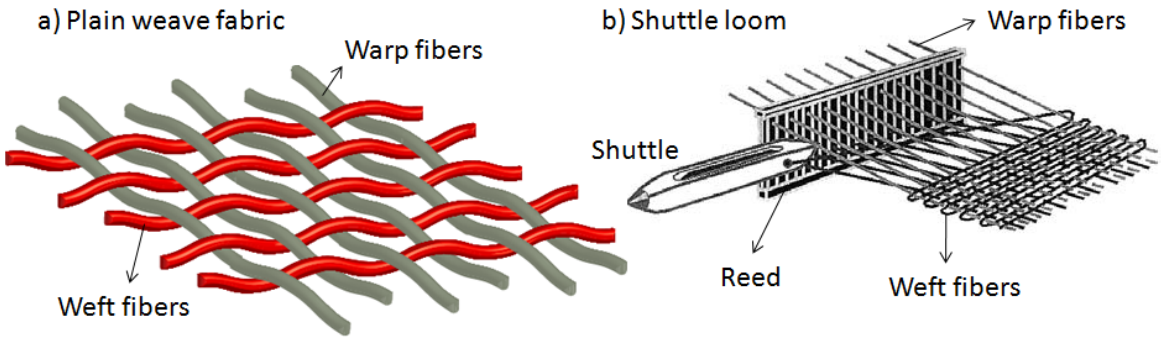

Figure 5.4. a) Schematic of a plain weave fabric b) Shuttle loom widely used to make woven fabrics. Figure reproduced from ref. [75] page 87.

5.3 Single-fiber thermoelectric power generators

5.3.1 Fabrication method and testing procedure

Thin-film metallic thermocouples are a convenient basis for a proof-of-concept demon-

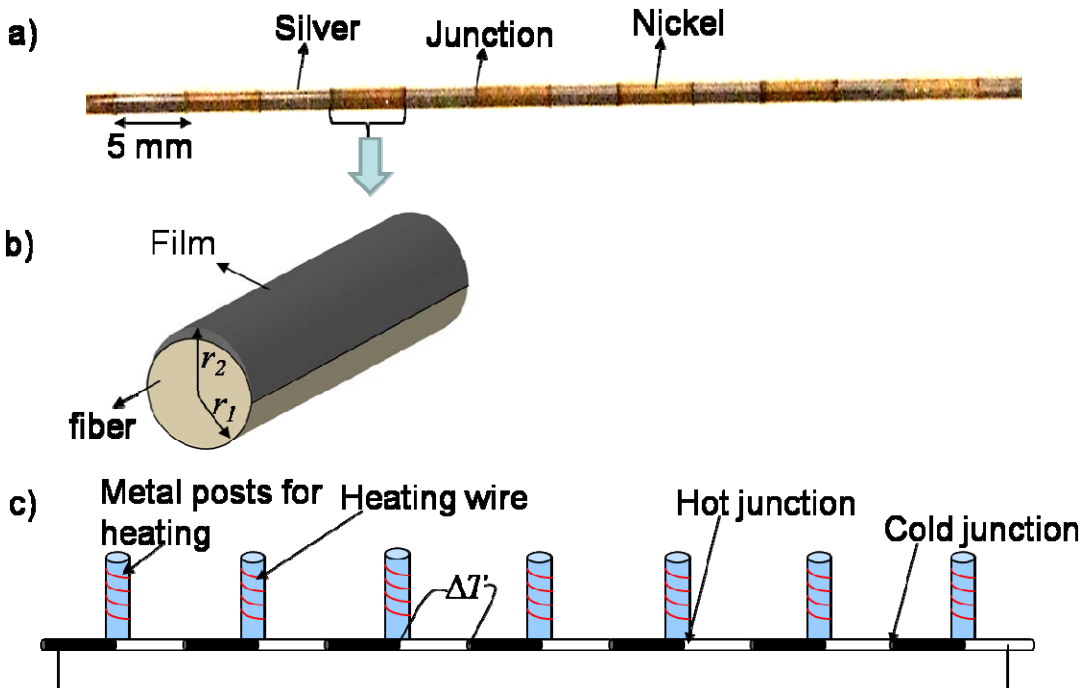

Figure 5.5. (a) Picture of striped thin film thermoelectric fiber made with thermal evaporation of nickel and silver **(b)** Illustration of fiber with thin film deposited on one side **(c)** Schematic of experimental setup for applying a temperature gradient and measuring the induced open circuit voltage.

stration of thermoelectric fibers. Adjacent stripes of nickel and silver are first deposited on one side of a silica fiber of diameter 710 μm by thermal evaporation under a pressure of 5×10^{-7} torr as shown in Figs. 5.5a & 5.5b. First a silver layer of thickness 120 nm is deposited through a mask; the mask is then moved to cover the deposited silver, and a nickel layer of thickness 120 nm is deposited. The junctions are formed by a small (0.5 mm) overlap between the two metals.

In order to test the thermoelectric properties of the fiber, temperature gradients must be applied by heating alternate junctions. This mimics the performance of the fiber inside a woven pattern, which has a temperature gradient normal to the surface. As shown in **Fig.** 5.5c, we use electrically insulated posts with heating wire wrapped around them to function as heat sources, bringing alternate fiber junctions in contact with them. The unheated junctions are exposed to ambient (22^{o}C) and lose heat due to convection. Temperature differences between neighboring junctions are measured using microthermocouples. Open circuit voltage vs. temperature is measured, as well as the induced voltage across a matched load resistor.

5.3.2 Measurement of thermoelectric power generation characteristics

The resistance of the thermoelectric fiber is measured to be 123 Ω, which includes the contact resistance between the gold probe wires and the ends of the TE fiber. This gives a total resistivity of 470 nΩ m for Ni-Ag, which is higher than literature values of

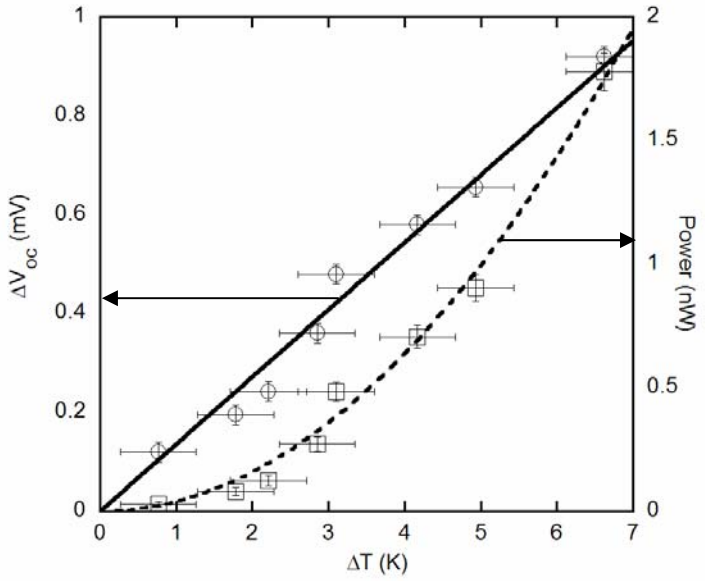

Figure 5.6. Net thermal voltage and maximum power output as a function of temperature applied for 7 couples.

190 nΩ m [77] for vacuum evaporated nickel and 20 nΩ m [78] for vacuum evaporated silver. The larger resistivity is attributed to junction and contact resistivity, as well as film quality.

In **Fig.** 5.6 the open circuit voltage developed as a function of temperature difference (ΔT) between the junctions and the maximum power output is plotted. The net open circuit voltage is sum of the thermoelectric voltage developed over all the junctions. A linear fit to the experimental data yields a Seebeck coefficient of 19.6 ± 0.6 μV/K, which agrees well with the bulk theoretical value for the Ni-Ag junction of 19.2 μV/K [79]. The measured Seebeck coefficient shows no effects due to film thickness or substrate geometry. The maximum generated power is measured by placing a load resistor with resistance matched to that of the fiber and is given by:

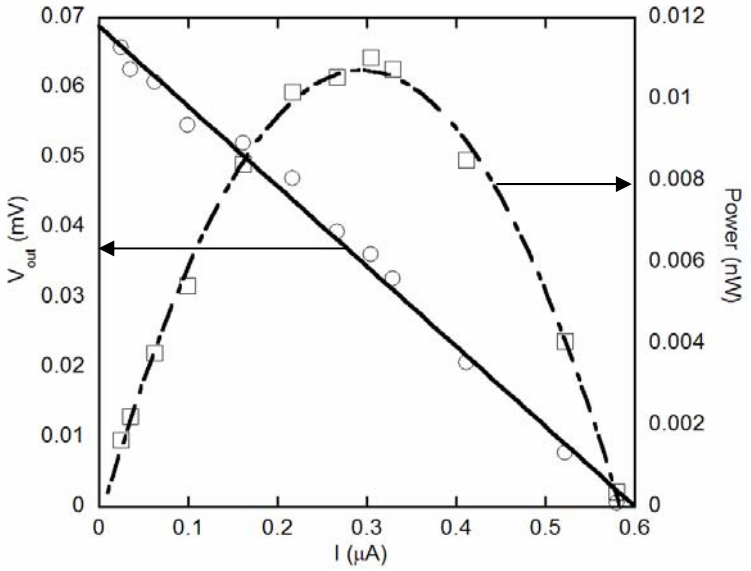

Figure 5.7. Power and output voltage as a function of current for ΔT=3.1 K for 1 couple.

$$P_{\max} = \frac{n^2 S^2 \Delta T^2}{4R_f} \tag{5.1}$$

where P_{max} is the maximum power output, S is the net Seebeck coefficient of each junction, n is the number of thermocouples, and R_f is the total electrical resistance of the fiber, which can be written as:

$$R_f = \left(\frac{\rho_e}{A_e} + \frac{\rho_p}{A_p} \right) nl \tag{5.2}$$

where ρ_e and ρ_p are the electrical resistivity of the n and p segments and A_e and A_p are the respective cross-sectional areas. The maximum power increases as the square of the temperature difference applied, which is seen in the experimental data. The internal resistance of the fiber and the combined Seebeck coefficient of the junction also affect the power output. **Figure** 5.7 plots the voltage and power versus the current produced by a single thermocouple for a constant ΔT = 3.1 K. At a constant ΔT, the fiber acts as a constant voltage source for which the maximum current is given by the short circuit current. With an increase in load resistance, the current decreases but the output voltage increases; hence there is a maximum in the power output at a load resistance that is matched to the resistance of fiber. Increasing the number of thermocouples shifts the line upward, but the slope of the V_{out} versus I curve will remain constant for same load resistance. Increasing the number of thermocouples will increase the maximum output voltage (ΔV_{OC}), as well as the slope of the graph (i.e. fiber resistance, R_f). As Equation (5.1) indicates, the power will increase linearly with the number of couples.

5.3.3 Optimization of material parameters for maximizing power generation

In thermoelectric power generators ΔT is often a fixed parameter, given for example by the wall temperature of the heat source and the lowest heat sink temperature accessible via convective cooling. In the case of constant ΔT, the power simply scales as $1/l$ with increasing segment length l, due to an increase in the electrical resistance [80]. Taking into account the effect of contact resistance, an optimization of power can be obtained [81, 82]. For fiber-based flexible thermoelectric power generators, one practical configuration would involve a woven thermoelectric fabric wrapped around a hot object, experiencing convective cooling on the opposite side. Under these boundary conditions, both ΔT and resistance can change with segment length, and an optimization in power output can also be obtained. To investigate the optimization conditions for power output, a simple fin heat transfer equation is used to calculate the temperature difference between the hot and cold junctions. The thermal resistances of the thin film and fiber substrate are given by [83]:

$$R_{th,film} = \frac{l}{\pi\left(r_2^2 - r_1^2\right)k_{film}} \tag{5.3}$$

$$R_{th,fiber} = \frac{l}{\pi r_1^2 k_{fiber}} \tag{5.4}$$

where r_2 and r_1 are the outer and inner diameters as shown in **Fig.** 5.5, k_{fiber} is the thermal conductivity of the fiber, and k_{film} is the thermal conductivity of the thin film. For the silica fiber, the thermal conductivity is 1.2 W/mK, and the thermal resistance of both metal films is calculated to be at least 9 times larger than the thermal resistance of the fiber; hence heat transfer through the film is neglected. If thicker films of metals were to

be used, then $R_{th,film}$ will become comparable to $R_{th,fiber}$ and the heat transfer through the film would become important. Each segment of fiber can be treated as a fin with a given hot temperature T_h as shown in inset of **Fig.** 5.8. Because of the symmetry in the temperature profile, a boundary condition of zero net heat flux ($dT/dx=0$) is used on both ends of the segment. The temperature in the segment is given by:

$$T(x) = T_\infty + (T_h - T_\infty) \times \frac{\cosh m(l-x)}{\cosh ml} \tag{5.5}$$

where T_∞ is the ambient temperature (assumed to be 22°C) and m is given by [83]:

$$m = \sqrt{\frac{4h}{k_{fiber} D}} \tag{5.6}$$

where h is the heat transfer coefficient and D ($=2r_1$) is the diameter of the fiber. The heat transfer coefficient is obtained by fitting the experimentally obtained T_c with that calcu-

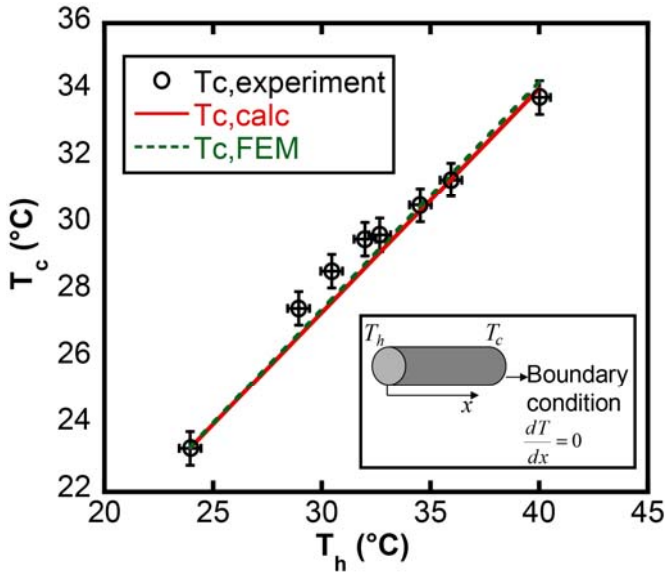

Figure 5.8. Temperature of cooler junction as a function of temperature of hotter junction from experiment, fin calculation and FEM simulation. Inset: One dimensional heat transfer along a segment can be modeled as fin heat transfer with adiabatic boundary condition (BC) on end of segment & convection on fiber surface.

lated from Equation (5.5). For a value of h=7.8 W/m^{2}K, a good match between experiments and calculation is obtained. This value is consistent with the cooling of a small surface by natural convection. **Figure** 5.8 shows the T_c obtained from Equation (5.5), finite element modeling (FEM) simulations using ANSYS™ (www.ansys.com), and experimental data. Equation (5.5) gives a good match with experiments. The FEM simulations in which exact modeling is also done to show the same T_c, further verifying the model.

Figure 5.9 shows the predicted power obtained per couple vs. the segment length for Ni-Ag thermocouples with the same film thicknesses as in the experiments above. Using Equation (5.5), ΔT can be calculated, and the net power per couple can be written as:

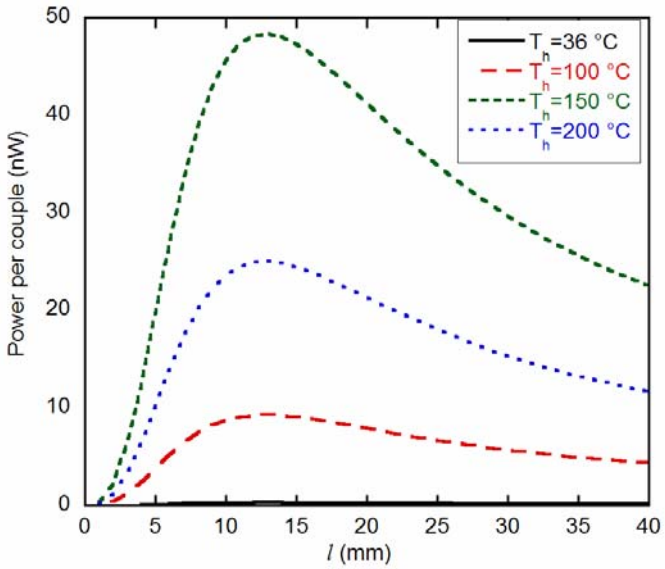

Figure 5.9. Power per couple vs. the segment length for different hot junction temperatures.

$$P = \frac{\pi S^2 \left(T_h - T_\infty\right)^2 t}{8\left(\rho_e + \rho_p\right)} \times \frac{D}{l}\left(1 - \frac{1}{\cosh\sqrt{\frac{4h}{k_{fiber}D}}l}\right)^2 \tag{5.7}$$

where t is the thickness of films. With an increase in segment length, the resistance of the fiber-based thermoelectric device increases linearly. However, there is also an increase in ΔT, until the maximum ΔT of T_h- T_∞ is obtained. At short segment lengths, the increase in ΔT dominates, and there is an increase in power. At large segment lengths, ΔT saturates at a value of T_h-T_∞, and the power decreases as 1/l. A maximum power per couple is obtained by minimizing Equation (5.7) with respect to l, yielding an optimization condition for a given diameter of fiber:

$$\sqrt{\frac{4h}{kD}}l_{\max} = 2.44 \tag{5.8}$$

For the silica fiber having approximately 0.71 mm diameter used in the experiments here, l_{max}=13 mm is obtained. Smaller diameter fibers would allow a shorter segment length.

Other controllable parameters include the thickness and composition of the deposited thin films. In **Fig.** 5.10, the effects of depositing materials with high thermoelectric figure-of-merit (ZT) at different film thicknesses are investigated. Bi_2Te_3-Sb_2Te_3 is a high ZT material, but for thin films the increase in electrical resistance caused by using a semiconductor material can offset the effect of increased thermopower. The Seebeck coefficient for Bi_2Te_3-Sb_2Te_3 is taken to be 375 μV/K, and the total resistivity is taken to be 33.5 μΩ·m. These values are based on thermally co-evaporated thin film measurements with a substrate temperature of 260 °C [84]. Similar values have also been obtained for Bi_2Te_3-Sb_2Te_3 films evaporated on polyimide substrates [85]. For Bi_2Te_3-Sb_2Te_3 thin films having the same thickness as Ni-Ag films, the generated power is

predicted to increase by a factor of 5, limited by a comparatively higher resistivity in the semiconductor material. In addition, because semiconductors have lower thermal conductivity than metals, they can be deposited as thicker layers (with correspondingly less electrical resistance) without reducing ΔT due to thermal leakage between the hot side and cold side. Bi_2Te_3-Sb_2Te_3 films on the order of 2000 nm (still thin enough to remain flexible) can produce an order of magnitude increase in power over 120 nm films.

If polymer fibers such as polyimide are used instead of silica fibers, the lower substrate thermal conductivity can lead to increased power output. Taking the thermal conductivity of polyimide to be 0.2 W/mK [65] and the heat transfer coefficient to be the same as that measured for silica fibers, we plot in **Fig.** 5.10 the power output per couple for a hollow polyimide fiber of outer diameter 550 μm and inner diameter 500 μm. Convection on the inside surface of the fiber is neglected, and ΔT is calculated using Equation (5.5). A power output of 1 μW per couple for segment length of 5 mm can be

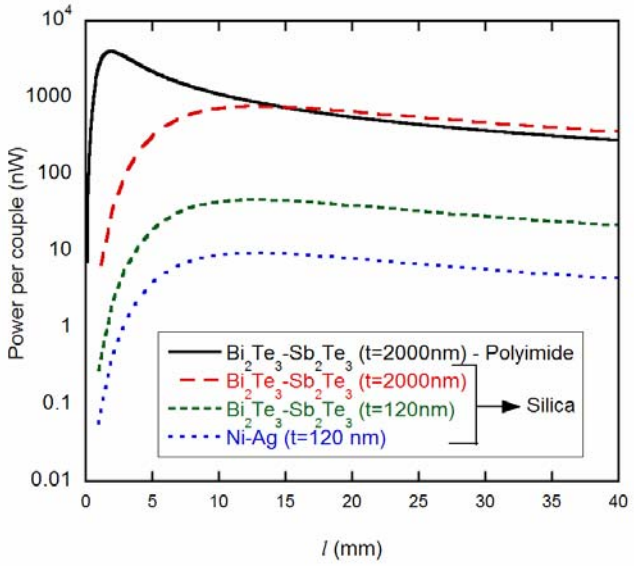

Figure 5.10. Comparison of power per couple from Ni-Ag thin films on silica fiber substrate and Bi_2Te_3-Sb_2Te_3 thin films on silica and polyimide fiber substrates for T_h=100 °C.

achieved for T_h=100 °C. Hence hollow polyimide fibers can be good candidates for compact, relatively high-power thermoelectric power generators. The peak in power when using a polyimide substrate is shifted to lower segment lengths because of the smaller thermal conductivity of polyimide compared to silica which allows a larger ΔT to develop for smaller segment lengths.

5.4 Multi-fiber thermoelectric power generators: Plain weave geometry

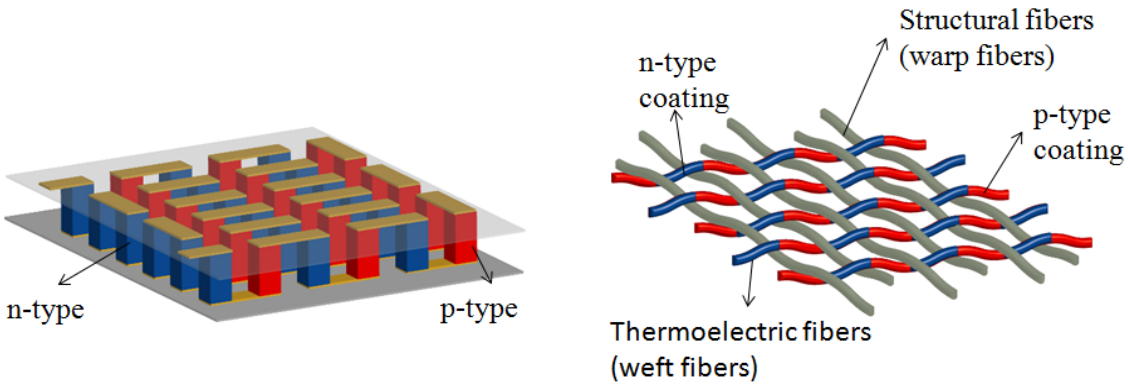

a) Conventional TE power generator b) Woven TE power generator

Figure 5.11. Schematic of **(a)** conventional TE power generator **(b)** woven TE power generator with plain weave geometry.

In Section 4.3 we looked at fabrication and characterization of single fiber, multi-thermocouple power generators. For large area heat scavenging applications, multiple fibers must be incorporated into a single device. Suitable candidates for achieving this include composites or textiles. In this section we look at textile-based thermoelectric power generators. **Figure** 5.11(a) shows the schematic of a conventional thermoelectric power generator with *n* and *p* type elements which are electrically in series but thermally in parallel. The junction between the *n* and *p* type elements is made by metal contact pads. The devices structure for TE power generators on woven textiles is shown in **Fig.**

5.11(b). Here we have replaced the metal contact pads by a small overlap between n and p type elements as also seen in Section 4.3. The TE fibers go over and under the structural warp fibers. The bending of the fibers is called crimp. To maximize the weft crimp, the warp cover factor or the number of warp fibers for each weft fiber must be increased. The weft crimp can also be increased by using a warp of higher tensile strength or weaving the structure under higher tension. We expect upto 1000 segments can be woven per cm^2, depending on the weave density and the fiber diameter. In comparison commercial TE generators made from bulk Bi_2Te_3/Sb_2Te_3 have ~ 10 couples per cm^2. A higher density of thermocouples in textile based thermoelectric power generators can offset their low efficiencies because of using thin films.

5.4.1 Fabrication method and testing procedure

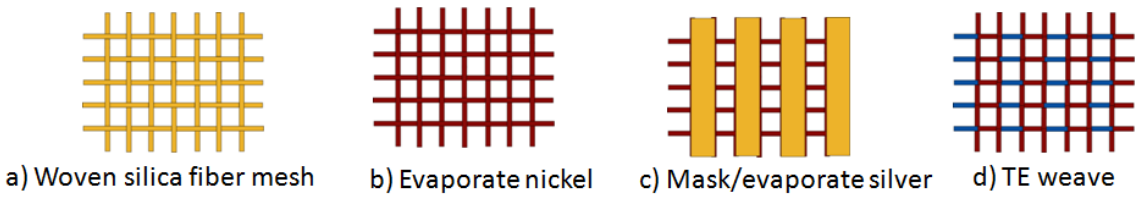

Figure 5.12. Fabrication method for vapor deposited TE power generators **(a)** a plain weave mesh is used as substrate **(b)** 100 nm of nickel is deposited **(c)** alternate junctions are masked **(d)** 100 nm of silver is deposited through the mask.

We demonstrate the ability to fabricate plain weave TE generators using both vapor-deposited and solution-deposited metals. Nickel is used as an *n-type* TE material and silver as a *p*-type TE material for vapor-deposited devices. For solution-deposited devices, nickel is used as an *n-type* material and silver as a *p-type* material. In **Fig.** 5.12 we show all the fabrication steps for vapor deposited devices. A plain weave polyimide coated silica fiber mesh is used as substrate. Weft fibers of diameter 100 μm, warp fibers

from 100-400 μm, and segment length of 5 mm are used. 100nm Nickel is evaporated everywhere on the weave, followed by masking of alternate junction. Silver is then evaporated through the mask. This results in alternate junctions being made of 100nm silver film on top of a 100 nm nickel film. The electrical conductivity and Seebeck coefficient of the two conductors in parallel is given by Equations (5.9) and (5.10) respectively.

$$\sigma_{composite} = \sigma_{Ag} t_{Ag} + \sigma_{Ni} t_{Ni} \tag{5.9}$$

$$S_{composite} = \frac{S_{Ag}\sigma_{Ag} t_{Ag} + S_{Ni}\sigma_{Ni} t_{Ni}}{\sigma_{Ag} t_{Ag} + \sigma_{Ni} t_{Ni}} \tag{5.10}$$

Since silver has much higher electrical conductivity than nickel, from Equation (5.9) we find the electrical conductivity of composite layer is determined by the silver film.

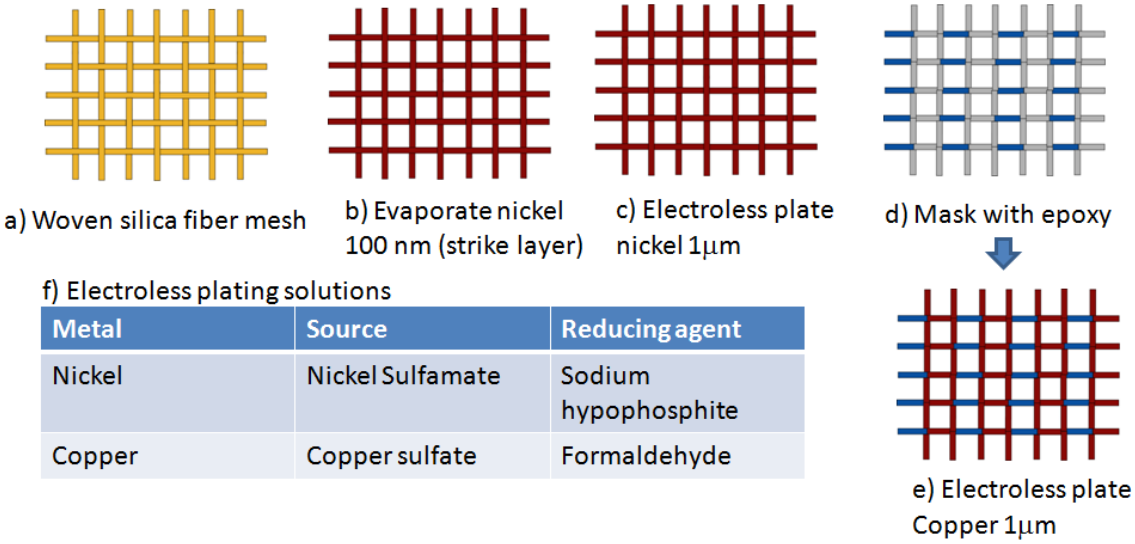

f) Electroless plating solutions

Metal	Source	Reducing agent
Nickel	Nickel Sulfamate	Sodium hypophosphite
Copper	Copper sulfate	Formaldehyde

Figure 5.13. Fabrication method for solution deposited TE power generators **(a)** a plain weave mesh is used as substrate **(b)** 100 nm of nickel is evaporated **(c)** 1 μm of electroless nickel is plated **(d)** alternate junctions are masked with epoxy **(e)** 1 μm of copper is electroplated **(f)** plating and reducing solution for nickel and copper.

Substituting in Equation (5.10) we find $S_{composite} \approx S_{Ag}$. Hence, the composite layer acts like silver film for thermoelectric transport.

In **Fig.** 5.13 we show the fabrication method for solution-processed plain weave TE generators. Plain weave silica meshes are again used as the substrate. 100 nm nickel is evaporated on it to acts as a strike layer. This is followed by electroless deposition of 1μm nickel. We use phosphide free nickel plating solution which gives better electrical properties but may be less adhesive and may produced films that are more brittle than other solutions. After nickel plating, a thin layer of epoxy is brush-coated on alternate junctions to avoid being plated by copper. Finally, 1μm of copper is plated, acting as an *n*-type material.

The experimental setup is shown in **Fig.** 5.14. The device is placed on a hot plate and a thermocouple is used to measure the hot side or surface temperature and cold side

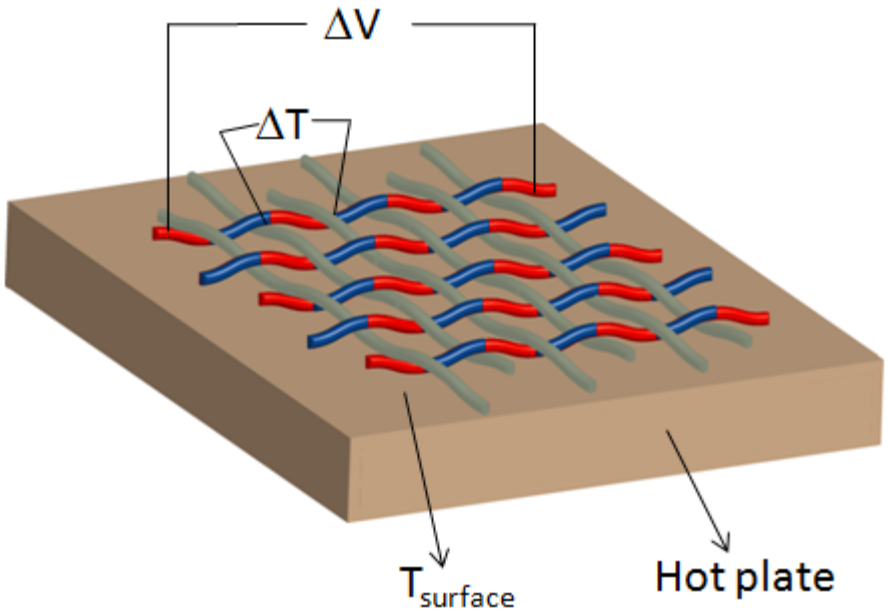

Figure 5.14. Experimental setup used for measuring the open circuit voltage and Seebeck coefficient

temperature. The open circuit voltage is measured using a multimeter.

5.4.2 Results and discussion

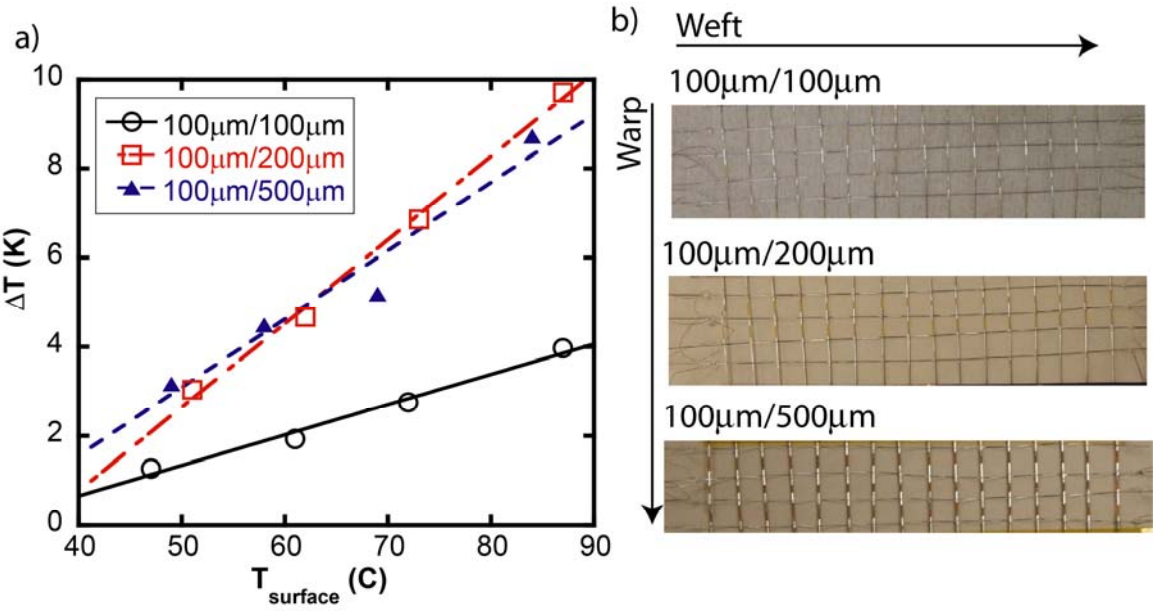

Figure 5.15. (a) Temperature drop across a thermocouple for different weft and warp diameters as a function of the difference between surface temperature and ambient temperature for evaporated devices. (b) Photograph of woven fiber meshes of different warp diameters.

Figure 5.15 (a) shows the temperature difference between the hot and colds side of thermocouple for different warp diameters and surface temperatures which are shown in **Fig.** 5.15 (b). With an increase in warp diameters the crimp of weft fibers is also increased, leading to a higher temperature difference. At the same time, there is a decrease in the crimp of warp fibers because the rigidity of glass fibers increases with diameter. Since heat flows through both weft and warp fibers, the decreasing crimp of warp fibers will lead to a smaller temperature difference between the hot and cold junctions. As a result, on increasing the warp diameter from 200 µm to 500 µm there is no net increase in the temperature difference. **Figure** 5.15 also shows linear fits passing through 0 to the experimental data. From Equation (5.5) we find that the temperature

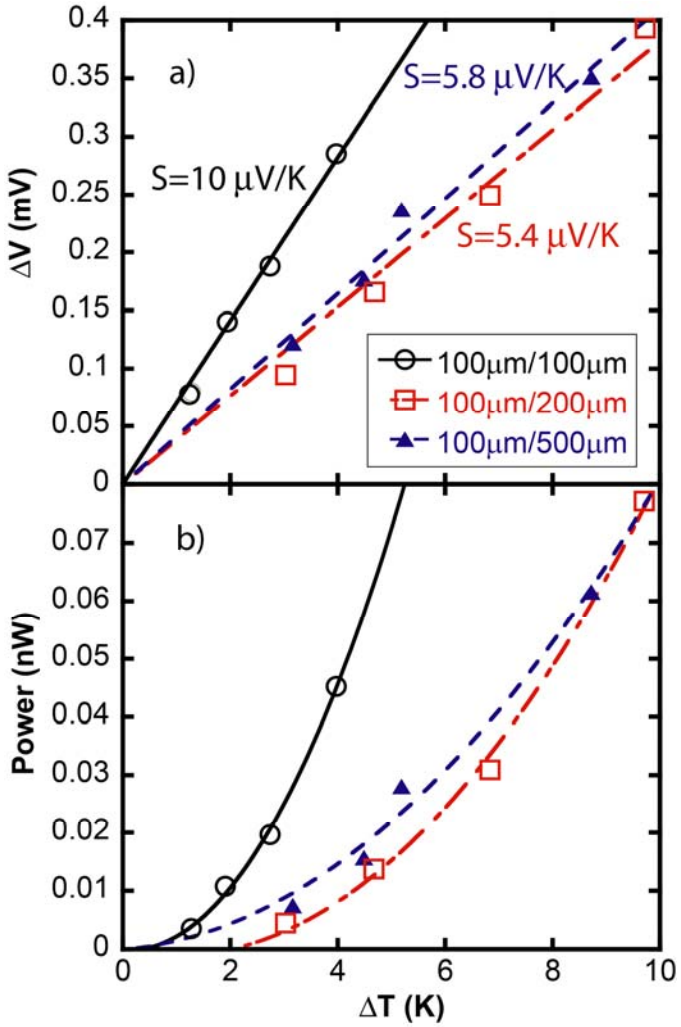

Figure 5.16. (a) Thermoelectric voltage and **(b)** maximum power generated for 7 thermocouples as a function of the temperature difference between the hot and cold junctions.

difference between the hot and cold sides can be written as:

$$\Delta T = \left(T_h - T_\infty\right)\left(1 - \frac{1}{\cosh\left(ml\right)}\right) \tag{5.11}$$

Under steady state, $T_{surface}$ can be approximated as T_h for fabrics in close contact with the surface. Using the slope of the linear fit from **Fig.** 5.15 and Equations (5.6) and (5.11), we can find an effective heat transfer coefficient. The heat transfer coefficient is obtained as 0.122 W/m^{2}K for 100μm/100μm TEG, 0.312 W/m^{2}K for 100μm/200μm TEG, and,

0.293 W/m^{2}K for 100μm/500 μm TEG. This is much smaller than that measured for single fibers in Section 5.3. In plain weave geometry, the thermoelectric segments are much closer to the hot surface across their whole length as compared to the thermoelectric segments in single fiber geometry. Because of this, radiative and convective heating of the whole fiber segment is expected, leading to a reduced heat transfer coefficient and temperature gradient across the fiber segment.

Figure 5.16 shows the thermoelectric voltage and maximum power developed for 7 thermocouples. The net Seebeck coefficient is found to be smaller than that measured for a single fiber. We attribute this reduction in Seebeck coefficient to poor junction formation.

Similar measurements are made for plain weave TE generators fabricated using electroless plating of nickel and copper as shown in **Fig.** 5.13. A segment length of 3 mm

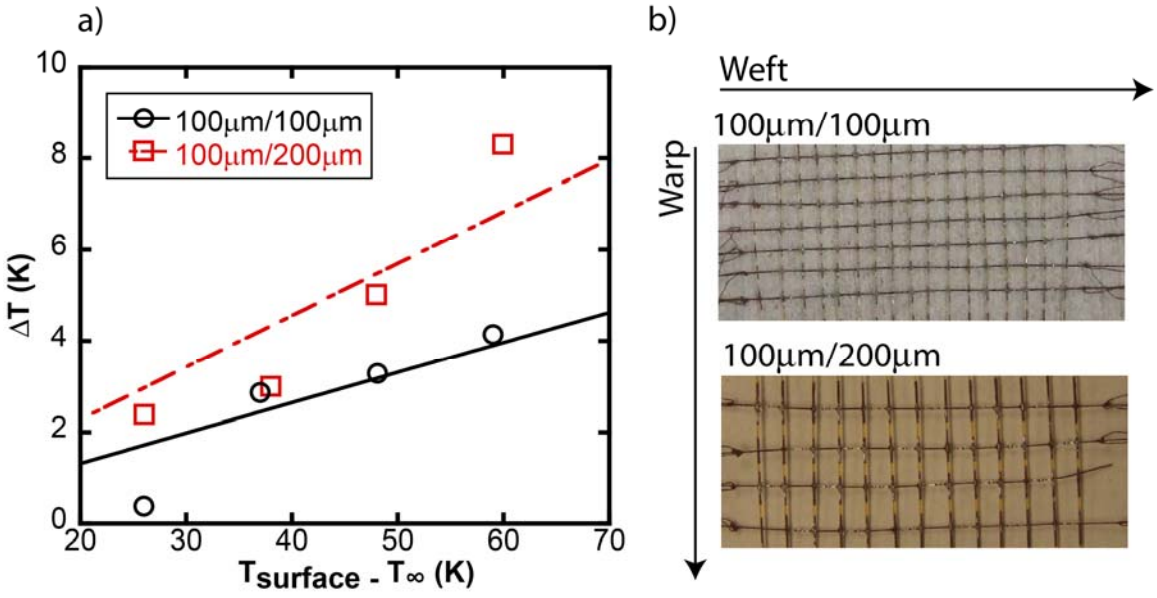

Figure 5.17. (a) The temperature difference between the hot and cold sides of thermocouple as a function of surface temperature. **(b)** Photograph of 8 couple 100μm/100μm and 6 couple 100μm/200μm plain weave fiber meshes.

is chosen for testing these devices. **Figure** 5.17 (a) shows the temperature drop across the thermocouple as a function of surface temperature for 100mm/100mm and 100μm/200μm plain weave meshes whose pictures are shown in **Fig.** 5.17 (b). The heat transfer coefficients calculated are: 0.14 W/m^{2}K for 100μm/100μm TEG, and 0.7 W/m^{2}K for 100μm/100 μm and 3 mm segment length TEGs. The heat transfer coefficient is smaller than that of evaporated TEGs because of the use of epoxy, which can add significant thermal resistance between the surface and the hot side of fiber. **Figure** 5.18 shows the thermoelectric voltage and power generated by 8 couple 100μm/100μm and 6 couple 100μm/200μm plain weave meshes. The Seebeck coefficient is found to be 4

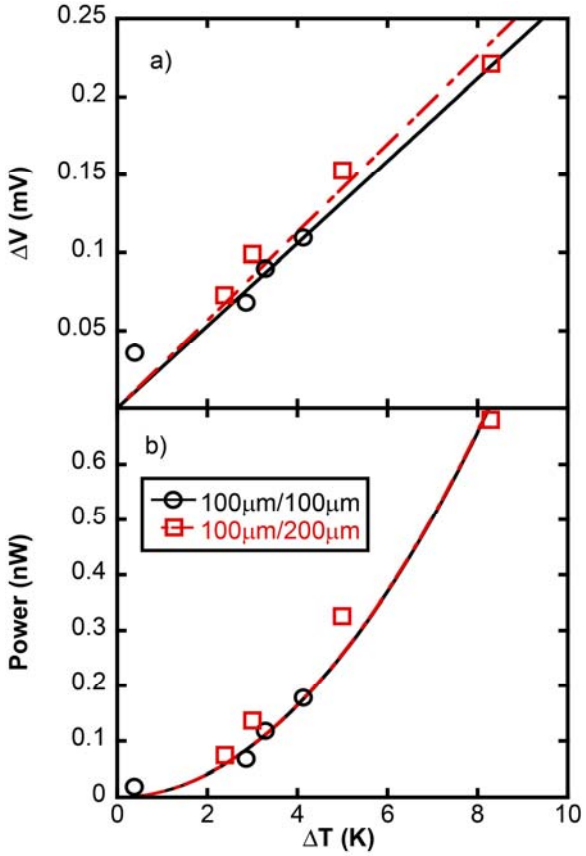

Figure 5.18. (a) Thermoelectric voltage and **(b)** maximum power generated for 8 couple 100μm/100μm and 6 couple 100μm/200μm plain weave meshes as a function temperature difference between hot and cold junction for electroless plated TEG.

μV/K for 100μm/100μm plain weave meshes and 4 μV/K for 100μm/200μm plain weave meshes. The lower Seebeck coefficient can arise because of poor junction quality or poor quality of electroless plated films. The power generated is proportional to square of thermoelectric voltage, and hence scales as the square of temperature difference. Using electroless plating, a larger thickness of metal layers can be obtained, yielding a smaller electrical resistance. Hence, the maximum power produced is much higher than that achievable in evaporated TEGs.

5.5 Summary

We demonstrated novel fiber-shaped thermoelectric devices composed of thermally evaporated or electroless plated thin film thermocouples for both single fiber and multiple fiber plain weave devices. Single fiber thermoelectric power generators were characterized by measuring open circuit voltage and electrical power output as a function of the temperature difference between the junctions. The measurements were extended to different thermocouple segment lengths, different material systems, and different fiber geometries by applying simple heat transfer analysis based on the measured data. These theoretical and experimental analyses show that fiber-based thermoelectric devices can be utilized to make flexible thermoelectric power generators for waste heat recovery. In particular, thicker semiconductor films evaporated on hollow, low thermal conductivity polymer substrates offer a good opportunity to extract and convert a relatively large amount of heat energy from arbitrarily shaped heat sources.

Multiple fiber thermoelectric power generators were demonstrated using plain weave textile geometries. Polyimide fibers of diameter 100μm were woven with polyimide fibers of diameter in range 100μm-500μm. Thin film metal thermocouples were

fabricated using either thermal evaporation of Ni-Ag thermocouples or a combination of thermal evaporation and electroless plating of Ni-Cu thermocouples. Although, the convective cooling for plain weave geometries is adversely affected because of close spacing to hot surface, this technique can lead to fabrication of a large number of thermocouples per unit area. For example, with close packing of 100μm fibers and a segment length of 1mm, upto 500 thermocouples can be fabricated per cm^2. In comparison, commercially available thermoelectric power generators have about 10 thermocouples per cm^2. A high thermocouple density is expected to offset the low efficiency expected from thin film thermoelectric devices. Other weave geometries such as twill, matt, and satin require more complicated weaving techniques but are possible candidates for textile based thermoelectric power generators.

Chapter 6

Organic photovoltaics

The photovoltaic effect consists of the conversion of light into electricity. Photovoltaic devices are based on the photoelectric effect, which holds that a minimum amount of energy given by the work function of a material is needed to absorb a photon and eject an electron from the material [9]. Semiconductor solar cells are based on the internal photoelectric effect in which an electron moves from the valence band to the conduction band upon absorption of a photon.

Most photovoltaic devices are made from inorganic semiconductors such as silicon (amorphous and crystalline), II-VI compounds (CdTe or CdS) and chalcogenides ($CuInSe_2$ or $CuInGaSe_2$) [86]. These materials consist of covalently bonded atoms which support strong delocalization of electronic wavefunctions and the formation of bands. Organic semiconductors, on the other hand, consist of Van der Waals bonded molecules made up of conjugate bonded carbon and hydrogen atoms. The presence of conjugate bonds results in a large delocalization of electronic wavefunctions over single molecules. However, Van der Waals interactions are very weak, causing most organic crystals to retain the electronic properties of single molecules. In addition, these weak intermolecular forces result in significant differences in charge transport. While charge transport in inorganic semiconductors occurs through band transport, in organic

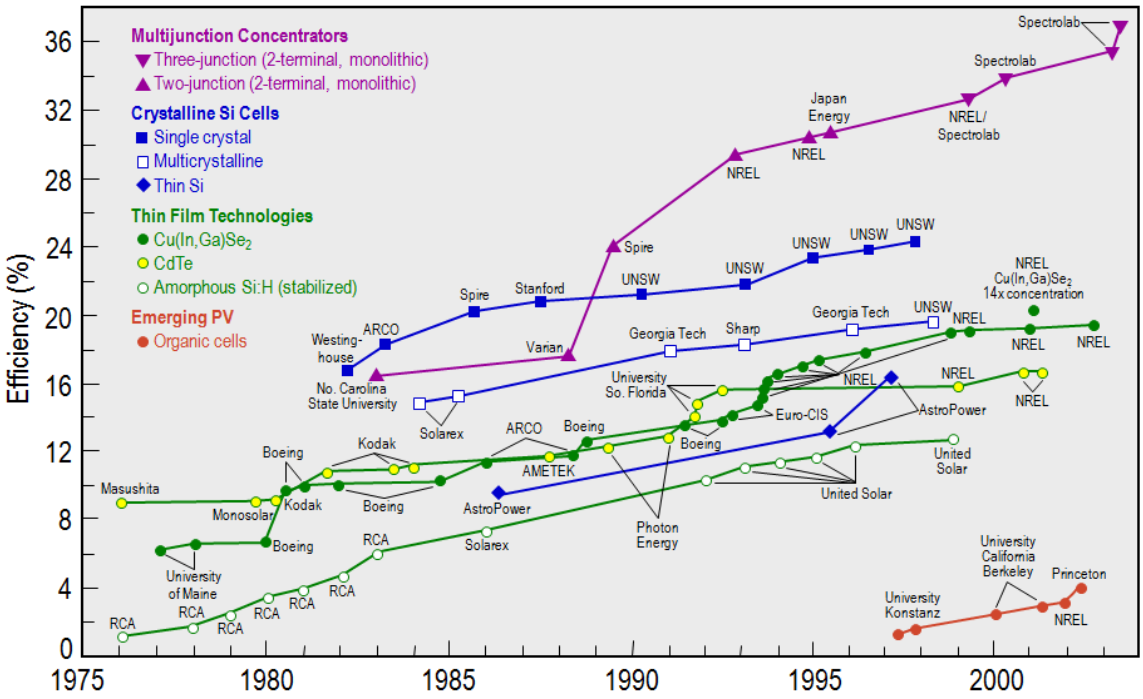

Figure 6.1. Maximum conversion efficiency for solar cells made from different material systems [88].

semiconductors it is dominated by carrier hopping [87]. Hence, the carrier mobility in organic semiconductors is much lower than that in inorganic semiconductors.

Figure 1.1 shows the maximum efficiencies achieved from solar cells made from different material systems [88]. Solar cells made from organic semiconductors have significantly lower efficiencies than inorganic based semiconductors, yet can provide significant cost advantages because of low material costs. For example, the organic semiconductors known as phthalocyanines are also used as dyes in the textile and paint industries and are cheap to produce. Organic semiconductors are ideal candidates for making large area devices since no lattice matching to a substrate is required.

6.1.1 Materials and device structures

Figure 6.2 (a) shows the general structure of an organic semiconductor based

photovoltaic device [86, 87]. The substrate consists of Indium doped tin oxide (ITO) coated glass; ITO is used as the anode because it is highly transparent to visible light. Two organic materials, which are used to absorb light, form a heterojunction. One of the organic materials has an electron donor characteristic with low ionization potential, while the other has an electron acceptor characteristic with high ionization potential. Typical donor materials include metal phthalocyanines such as copper phthalocyanine shown in **Fig.** 6.2 (b), while a commonly used acceptor is C_{60}, the chemical structure of which is shown in **Fig.** 6.2 (c).

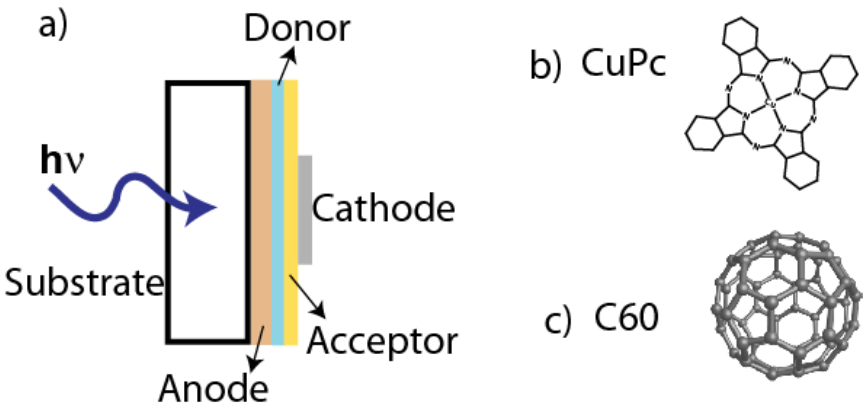

Figure 6.2. (a) Device structure for an organic semiconductor based photovoltaic device, **(b)** A commonly used donor material, copper phthalocyanines (CuPc), **(c)** a commonly used acceptor material, fullerene (C_{60}).

6.1.2 Working principle of organic photovoltaics

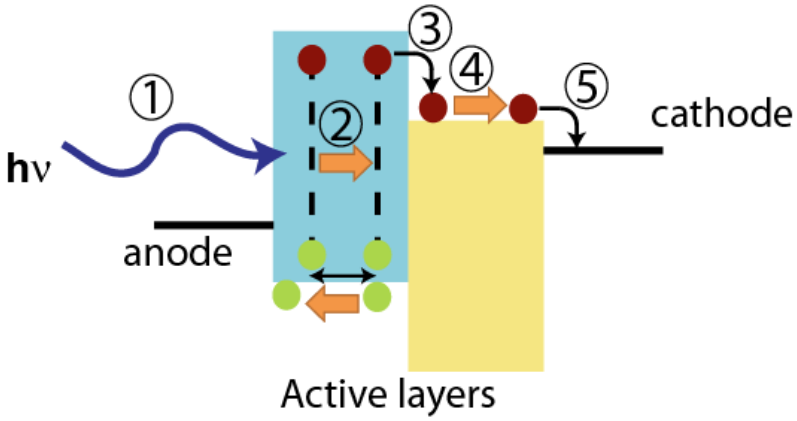

Figure 6.3. Working principle of organic photovoltaic device

A photovoltaic device based on organic semiconductors consists of two active layers which form a heterojunction. One of the semiconductors has low ionization energy and therefore acts as an electron donor, while the other has a high ionization energy and therefore acts as an electron acceptor [86, 89]. Upon junction formation, the bands align as shown in **Fig.** 6.3. The transformation of a photon to free carriers requires the formation of an intermediate bound electron-hole pair state called an exciton. The ground state for electrons in an organic semiconductor is a bound state the called highest occupied molecular orbital (HOMO). Upon excitation with light, they can move to higher bound state called the lowest unoccupied molecular orbital (LUMO). The transport gap lies above the bound states. The formation, transport, and disassociation of excitons are of fundamental importance for understanding and improving the successful working of an OPV. The working of an OPV can be summarized in 5 primary steps (shown in Fig. 1.9) which are discussed below:

Step 1: Light absorption

Light absorption in organic semiconductors occurs through the formation of bound electron-hole pairs called excitons as shown in **Fig.** 6.4. This is in contrast to inorganic semiconductors where light absorption results in the formation of free carriers. This distinction in formation of excitons or free carriers arises due very different dielectric constants in organic and inorganic semiconductors. Organic semiconductors have very low dielectric constants (typically in the range of 3-4) while the dielectric constant of

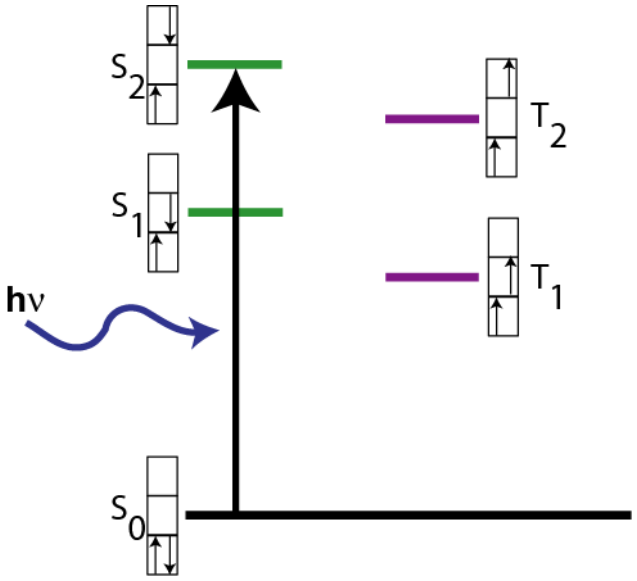

Figure 6.4. Excitation of electrons upon absorption of a photon leads to formation of bound states called excitons. S_0 is the ground state, S_1 is first singlet excited state also called a Frenkel exciton, S_2 is the second singlet excited state, and T_1 and T_2 are the first and second excited triplet states.

inorganic semiconductors is 2-3 times higher. As a result, the binding energy of excitons, which is inversely proportional to square of the dielectric constant, is few hundreds of meV in organic semiconductors. In comparison, the binding energies of excitons are only few meV in inorganic semiconductors, which is comparable to the thermal energy (k_BT = 26 meV at room temperature). Hence, the formation of excitons in inorganic

semiconductors is not stable, and light absorption results in direct free carrier formation.

Exciton formation in organic semiconductors can result in two types of excitons, depending on the spin configuration of electrons in the ground and excited states. If the spins of electrons in the ground and excited states are opposite, then a Frenkel or singlet exciton is formed. If the spin for both ground and excited state electrons is the same, then triplet excitons are formed. Triplet excitons have significantly larger lifetimes because the spin of one of the electrons has to be reversed for recombination to occur.

The absorption spectrum of organic semiconductors has to be matched well to the incident light spectrum. For solar cells, the spectrum of incident light is often approximated as AM 1.5G, which peaks in the green. Tuning of the bandgap can also affect the oscillator strength of transitions. It has been observed that with a decrease in bandgap, the oscillator strength goes down. Hence, organic materials with absorption in visible wavelengths are most suitable for solar applications.

Step 2: Exciton diffusion

Excitons generated due to absorption of light have to diffuse to an interface where the local electric field is sufficent to effect successful disassociation. Excitons are neutral particles and do not respond to electric fields. Hence, diffusion occurs through random hop. In general the diffusion of singlet excitons is modeled as Forster energy transfer. The diffusion lengths in organic semiconductors vary from few nm to 10's of nm. Typical values are 3 nm for PTCBI, 10 nm for CuPc, and 40 nm for C60 [89].

Step 3: Exciton disassociation

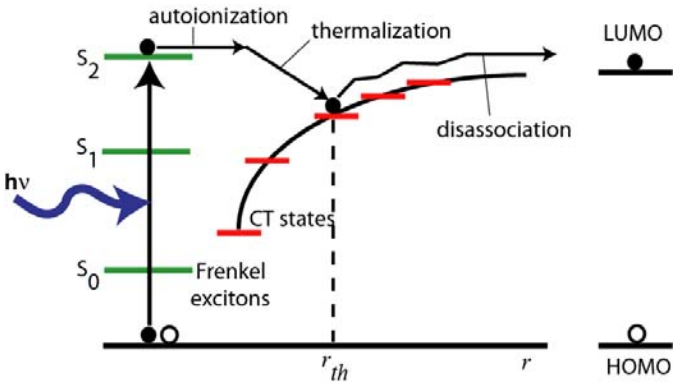

Figure 6.5. The process of autoionization of excitons leading to the formation of free carriers.

In order to generate free carriers that make up electrical current, excitons must be successfully disassociated. This process occurs through autoionization as shown in **Fig.** 6.5. The free carrier is thermalized by scattering from neighboring molecules and falls in energy to form an intermediate bound state known as a charge transfer state. In this case the hole and electron reside on separate donor and acceptor molecules and are held together by Columbic interactions. Successful disassociation can also occur if excitons move away from interface and if the binding energy of the CT state is smaller than thermal energy at room temperature. Since the binding energy of excitons in organic materials is a few hundreds of meV, disassociation of excitons in bulk organic materials is very inefficient. At heterojunctions, however, the transport gap for electrons is below the LUMO of donor molecules, and very high disassociation efficiencies can be achieved.

Step 4: Charge transport and collection

Once excitons are disassociated at the interface, the constituent electrons and holes move in opposite directions towards the cathode and anode. The transport of charge can occur through both drift and diffusion; charge collection efficiencies of ~ 100 % can be achieved [89].

6.2 Summary

In this chapter, the basic photophysics of organic semiconductors was discussed. The process from light absorption to free carrier generation can be divided into five main steps. The efficiency of organic photovoltaic devices is mainly determined by the tradeoff between exciton diffusion length and absorption length, which are dependent on the nature of exciton. The open circuit voltage is determined by the disassociation of excitons at heterojunctions. Charge transfer excitons play an important role in this process and their identification at heterojunctions is important. The morphology and crystal structure can affect the intermolecular interactions significantly leading to change in excitonic properties. In chapter 7, we use modulation spectroscopy based on temperature to determine excitonic nature in CuPc thin films. The effect of different crystal structure on the optical spectrum and excitonic properties is also studied. Finally, assuming the dipole moment matrix element for charge transfer excitons to decay exponentially, we determine the coefficient of exponential decay.

Chapter 7
Temperature Modulation Spectroscopy for Studying Excitonic Properties of Organic Semiconductors

7.1 Introduction

Organic thin films are finding applications in next-generation light-emitting and photovoltaic devices [89, 90]. The correlation of molecular structure and optical properties is a fundamental problem in condensed matter physics and is central to the design of optoelectronic materials and devices. While strong carrier localization in organic semiconductors is known to lead to the generation of bound electron-hole pairs (excitons) during light absorption or emission, the complex physical structure of most organic materials has precluded a detailed understanding of the processes governing exciton formation and transport. However, this carrier localization entails a sensitivity of exciton formation to perturbations in physical structure that can be significantly stronger than that of optical processes involving delocalized free carriers in inorganic crystalline semiconductors. Here we demonstrate that perturbation by thermal expansion offers a powerful and convenient method to characterize the excitonic properties of organic semiconductors.

The light absorption or emission spectrum of an organic material is determined by the

superimposed contributions of a number of excitonic transitions, each of which is typically described in terms of transition energy, oscillator strength, and lifetime broadening. The oscillator strength describes the interaction strength between the two states involved in the transition, while the lifetime broadening determines the exciton coherence length, affecting exciton transport properties such as diffusion length [87]. Exciton formation or recombination typically occurs through the direct transfer of charge between highest occupied molecular orbital (HOMO) and lowest unoccupied molecular orbital (LUMO) states. For charge transfer (CT) excitons, the transition occurs between HOMO and LUMO levels that are on neighboring molecules, while for Frenkel excitons it occurs between levels on the same molecule [91, 92]. Frenkel and CT excitons have significant differences in diffusion length, dissociation efficiency, and other transport properties [93, 94].

The intermolecular electronic transfer integral plays a key role in quantifying charge transfer in molecular crystals [95]. Photoemission spectroscopy has been used to derive transfer integrals for intraband (HOMO-HOMO and LUMO-LUMO) intermolecular transitions [96], which govern carrier mobility. However, no measurements have been made of interband (HOMO-LUMO) intermolecular transfer integrals, which govern the formation and dissociation of CT excitons. Here we demonstrate the use of thermal modulation to obtain interband transfer integrals; a simple variation of the technique in which modulated electrical current rather than optical transmission was measured could similarly be applied to obtain intraband integrals.

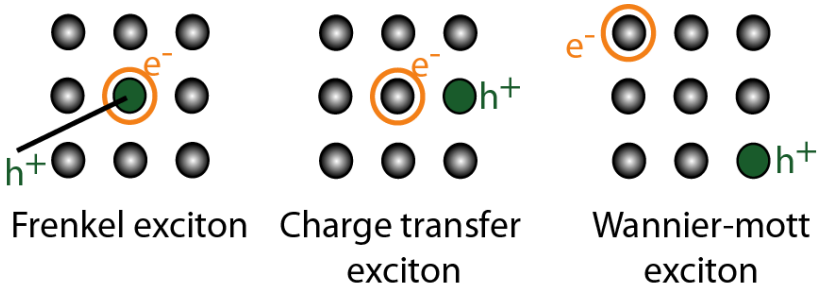

Figure 7.1. Representation of excitons in solid sate materials **(a)** Frenkel excitons with hole and electron bound on one molecule **(b)** Charge transfer excitons with hole and electron on neighboring molecules **(c)** Wannier-Mott excitons with hole and electron delocalized and separted by distance larger than intermolecular spacing.

Excitons in solid state materials fall into three different categories: 1) Frenkel excitons as shown in **Fig. 7.1(a)**, in which the bound electron and hole are on the same molecule, 2) charge transfer (CT) excitons as shown in **Fig. 7.1(b)**, in which the bound electron and hole are on neighboring molecules, and 3) Wannier-Mott excitons as shown in **Fig. 7.1(c)**, in which the hole and electron are separated by more than few intermolecular spacing lengths [91, 92]. The binding energy of an exciton is often written in terms of the Coulomb interaction as [87]:

$$E_B = -\frac{e^2}{4\pi\varepsilon\varepsilon_0 r} \tag{7.1}$$

where r is the radius of the exciton and ε is the dielectric constant of the intervening medium. Although not strictly valid for all exciton types, the binding energy is usually largest for Frenkel excitons because of their small radius and smallest for Wannier-Mott excitons.

Wannier-Mott excitons require strong interactions between neighboring atoms or molecules. In organic semiconductors, which are bonded by weak Van der Waals forces, only Frenkel and CT excitons are typically formed. Frenkel and CT excitons have

significantly different transport properties [93, 94]. While Frenkel excitons have a larger diffusion length than CT excitons, their smaller radius often leads to lower dissociation efficiency. Furthermore, Frenkel and CT excitons may couple to each other; for example, light absorption in an organic photovoltaic cell may initially create a Frenkel exciton, which diffuses to the donor-acceptor interface and forms a CT exciton, which then dissociates to generate photocurrent [87, 91]. To obtain high quantum efficiency in photovoltaic devices, both large diffusion length and high exciton dissociation efficiency are desired. In the context of organic light-emitting devices, electroluminescence has mainly been attributed to recombination on individual molecules that is limited by free carrier diffusion (Langevin recombination). However, optical recombination can also occur through the formation of a CT state [91] if the binding energy is large.

The formation or recombination of CT exciton states typically occurs through the direct transfer of charge between the highest occupied molecular orbital (HOMO) of one molecule and the lowest unoccupied molecular orbital (LUMO) of a neighboring molecule. The strength of the CT state depends on the spatial overlap of HOMO and LUMO electronic wavefunctions, which we refer to as interband electronic coupling. Because of the spheroidal shapes of molecular wavefunctions, electronic coupling is often written as an exponentially decaying function of intermolecular separation [97]. The decay coefficient quantifies the strength of electronic coupling and depends on the size and shape of the electronic wavefunctions as well as the binding energy of the electron on the donor site. For charge transfer states in liquid and glassy media, the decay coefficient has been derived by varying the concentrations of donor and acceptor molecules and measuring time-resolved optical spectra [97, 98]. As we show below, thermal expansion provides a convenient means to measure this important parameter in

condensed media, where Van der Waals bonding makes it otherwise difficult to controllably change the intermolecular spacing.

7.2 Determining the nature of excitonic transitions

Optical spectroscopy is widely used to study exciton properties in organic thin films. However, simple absorption spectroscopy cannot be used to distinguish between Frenkel and CT excitons because of their similar optical properties. Both Frenkel and CT excitons can be modeled using Lorentz-Lorenz or Gaussian dielectric models. The derivative of the optical spectrum shows peaks corresponding to the excitonic transition levels, but does not give any information which can be used to distinguish between Frenkel and CT excitons. Modulation spectroscopy takes the derivative of the optical spectrum with respect to a modulated physical parameter such as electric field or strain [99, 100] and can be used to identify optical transitions with low oscillator strength that are not easily visible in the optical spectrum. The three main types of modulation spectroscopies are listed in Table 7.1.

Parameter	Modulating effect	$\Delta\varepsilon$
Electric field	Stark effect	F^2
Temperature	Change in lattice constant	ΔT
Strain	Change in lattice constant	Δa

Table 7.1 Examples of modulation spectroscopies with associated modulated parameters, effects, and proportionality factors for induced changes in the optical spectrum.

7.2.1 Electric field modulation spectroscopy

Electric field modulation spectroscopy is the most common type of modulation spectroscopy applied to organic thin films. The effect of electric field on electronic properties such as transition energy levels occurs through the Franz-Keldysh effect for inorganic semiconductors and the Stark effect for organic semiconductors [101, 102]. The Franz-Keldysh effect causes a change in the bandgap of inorganic semiconductors due to tunneling of electrons from the valence band to the conduction band. The Stark effect leads to a change in transition levels in organic semiconductors because of a change in molecular polarizability or dipole moment upon the application of an electric field. Electric field modulation spectroscopy has been used to identify CT excitons in polyacenes [101], metal phthalocyanines [103], perylene derivatives [104] and phosphors

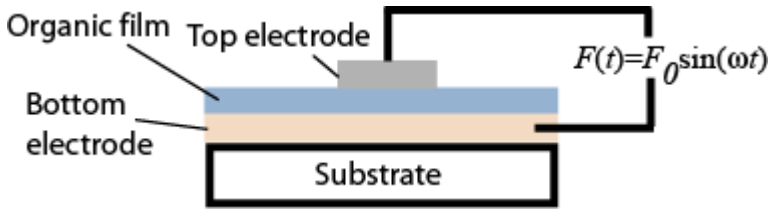

Figure 7.2. Sample structure for electric field modulation spectroscopy.

[105]. It has also been used to study charge injection [106], electric field distribution [107] and device degradation [108] in organic light-emitting diodes.

A schematic of the technique is shown in **Fig. 7.2**, where the material to be investigated is sandwiched between two electrodes and an oscillating electric field is applied. A lock-in measurement technique, which reduces errors due to noise in the optical detectors, is used to detect the induced change in the optical spectrum.

Because of the absence of band formation due to weak intermolecular forces, the main effect of applying an electric field in organic semiconductors is through the Stark effect. This effect causes a change in the optical spectrum through a shift in the excitonic transition energy given by:

$$\Delta E_{0i} = -\Delta m \cdot F - \frac{1}{2} F \cdot \Delta p \cdot F \tag{7.2}$$

where E_{0i} is the transition energy, F is the applied electric field, Δm is the change in dipole moment, and Δp is the change in molecular polarizability. The change in the absorption length can be written as:

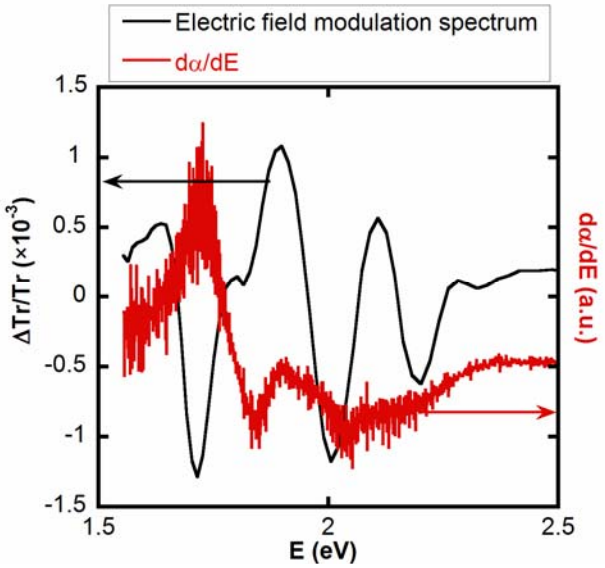

Figure 7.3. Electric field modulation spectrum of CuPc film of thickness 133 nm. The amplitude of the applied electric field modulation is 6×10^5 V/cm.

$$\Delta\alpha = \frac{\partial\alpha}{\partial E_{0i}} \Delta E_{0i} + \frac{1}{2} \frac{\partial^2\alpha}{\partial E_{0i}^2} \Delta E_{0i}^2 \tag{7.3}$$

For Frenkel excitons, where the change in excitonic energy level is dominated by the change in molecular polarizability, the change in absorption length is dominated by the first term and is proportional to the first derivative of optical spectrum. For CT excitons, the change in dipole moment dominates the change in excitonic energy level. In

this case the second order effect in Equation (7.3) is dominant and the change in optical spectrum is proportional to the second derivative of the optical spectrum. In **Fig. 7.3** the electric field modulation spectrum and first derivative of absorption spectrum are plotted. Although the lowest transition seems to follow $-d\alpha/dE$ well, the other transitions are difficult to match to $-d\alpha/dE$. Hence identifying excitonic transitions is not straightforward with electric field modulation spectroscopy. This is further complicated by parasitic effects caused by the application of the electric field. The presence of built-in electric fields at interfaces due to space charge can impede the application of this method to active devices and multilayer structures [109] as shown in **Fig. 7.4(a)**. In addition, injected charges can screen the applied AC electric field [110] or lead to formation of interface dipoles, destroying the proportionality between the EA spectrum and the magnitude of the electric field as shown in **Figs. 7.4(b)** and **(c)**.

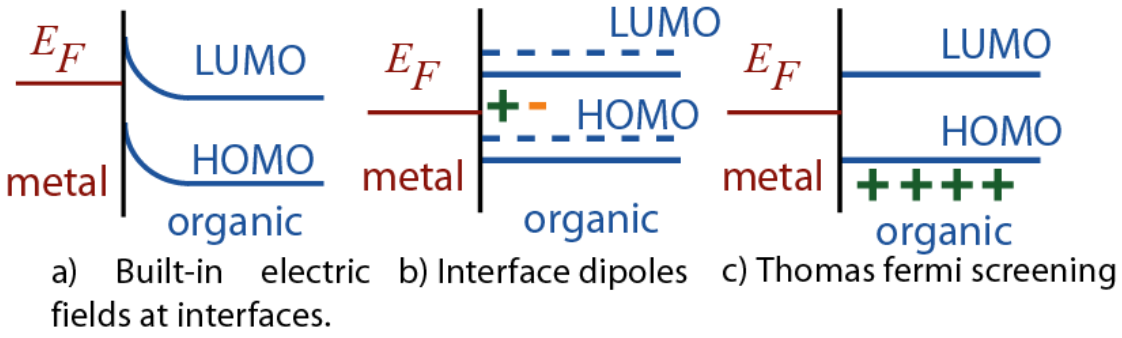

Figure 7.4. Disadvantages of electric field modulation spectroscopy

7.2.2 Piezomodulation spectroscopy

Piezomodulation spectroscopy involves change the lattice spacing between molecules using a piezoelectric modulator. This technique has been extensively applied to inorganic semiconductors, but its application to organic semiconductors is limited because of the difficulty in propagating strain waves coherently in disordered semiconductors. Films

have to be made with long distance order using a method such as Langmuir-Blodgett. Low temperature measurements are also needed to successfully propagate strain.

7.3 Temperature modulation spectroscopy

7.3.1 Theory

The effect of temperature on the dielectric constant occurs through both thermal expansion and increased phonon occupation. The average induced molecular polarizability for i^{th} optical transition can be written as [111]:

$$\alpha_i(E) = 2\hbar \frac{E_{0i} V_{DA,i}^2}{E_{0i}^2 - E^2 - iQ_i E} \tag{7.4}$$

where $V_{DA,i}$ is the dipole moment matrix element of i^{th} transition, E_{0i} is the transition energy, Q_i is the lifetime broadening, E is the energy of incident light. We make the assumption that the polarizability tensor has only one component in a local coordinate space (x,y,z) given by $\alpha_{xx,i} = \alpha_i$. The polarizability due to the electric field component along the X direction in laboratory coordinates (X,Y,Z) is then given by:

$$\alpha_{XX,i} = \alpha_{xx,i} \cos^2(Xx_i) \tag{7.5}$$

with all other components of the polarizability tensor being 0. Xx_i is the angle between the laboratory X-axis and the local x-axis for transition i. The net polarizability can be written by summing contributions from all electronic transitions:

$$\alpha(E) = 2\hbar \sum_i \frac{E_{0i} V_{DA,i}^2 \cos^2(Xx_i)}{E_{0i}^2 - E^2 - iQ_i E} \tag{7.6}$$

and the dielectric constant can be written as:

$$\varepsilon(E) = \varepsilon_\infty + 4\pi N\alpha(E) = \varepsilon_\infty + 8\pi N\hbar \sum_i \frac{E_{0i} V_{DA,i}^2 \cos^2(Xx_i)}{E_{0i}^2 - E^2 - iQ_i E} \tag{7.7}$$

where N is the number density of molecules. Phenomenologically we can write the dielectric constant as:

$$\varepsilon(E) = \varepsilon_\infty + \sum_i \frac{E_{pi}^2}{E_{0i}^2 - E^2 - iQ_i E} \tag{7.8}$$

where E_{pi} is the effective oscillator strength. From Equations (7.7) and (7.8), the effective oscillator strength can be written as:

$$E_{pi}^2 = 8\pi\hbar N E_{0i} V_{DA,i}^2 \cos^2(Xx_i) \tag{7.9}$$

The change in oscillator strength with respect to temperature can be written as:

$$\frac{2}{E_{pi}}\frac{dE_{pi}}{dT} = \frac{1}{N}\frac{dN}{dT} + \frac{1}{E_{0i}}\frac{dE_{0i}}{dT} + \frac{1}{V_{DA,i}^2}\frac{dV_{DA,i}^2}{dT} - 2\tan(Xx_i)\frac{dXx_i}{dT} \tag{7.10}$$

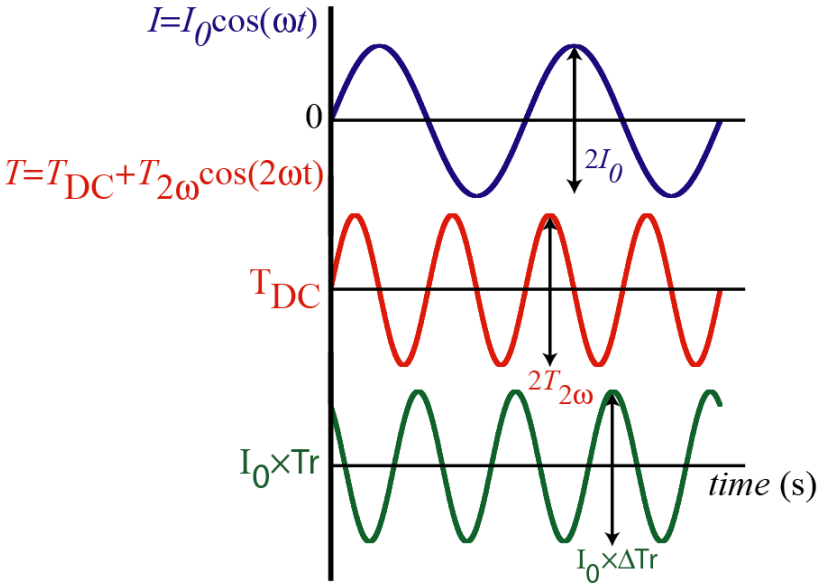

Figure 7.5. The working principle of phase sensitive detection.

The first term on right hand side arises because of a change in the number density due to

thermal expansion. Thermal expansion also changes the equilibrium distance between the molecules, leading to a shift in excitonic transition levels given by the second term. The third term arises if the dipole moment matrix element has a temperature dependence (due to, for example, a dependence on equilibrium intermolecular distance). The last term on the right hand side of Equation (7.10) is a geometric factor which arises because of a change in the orientation of molecules with respect to the incident electric field during thermal expansion.

In addition to affecting charge transfer at the level of individual molecules, temperature modulation is expected to affect resonant energy transfer in excitonic bands that form between a large number of coupled molecules in a thin film. The lifetime broadening is strongly linked to exciton band structure; the broadening of a given band through phonon absorption or emission depends on whether the band has a minimum or maximum at k_{ex}=0 [112]. For exciton energy bands for which lifetime broadening occurs through phonon absorption, we expect a significant increase in broadening with increase in temperature because of an increase in phonon occupation. Since lifetime broadening through phonon emission is a temperature-independent process, however, we expect to see no change in broadening for exciton bands with a maximum at k_{ex}=0 [87, 112].

7.3.2 Experimental setup

Temperature modulation spectroscopy requires the measurement of optical spectra at different temperatures. To obtain a true derivative spectrum, the modulation amplitude should be small. Since the change in optical spectra is of the order of 10^{-4}/K, which is comparable to the noise level in optical detectors, time averaging of the signal must be performed in order to remove the noise. Another method of achieving a high signal-to-

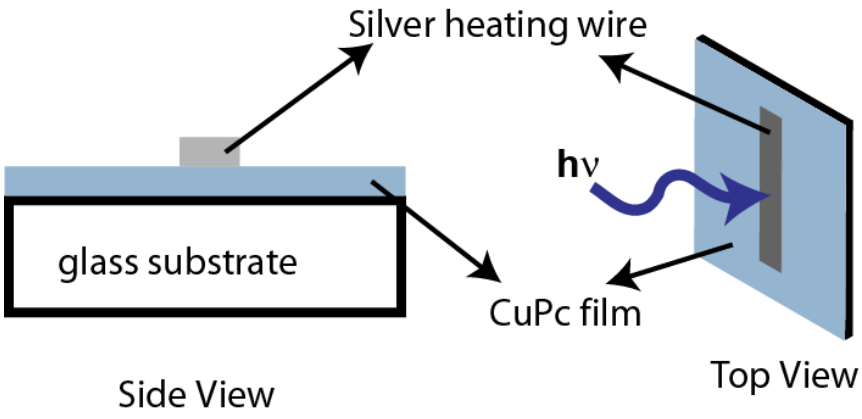

Figure 7.6. Sample structure to be measured using temperature modulation spectroscopy.

noise ratio is to use a phase-sensitive detection technique in which the temperature of the film is modulated at a certain frequency and a lock-in amplifier is used to measure the resulting signal. This technique has the advantage of avoiding long averaging times and is very suitable for spectroscopy in which a large number of data points is needed. On the other hand, time averaging is more suitable when the optical detector output is digital as data can be stored easily, such as when using a CCD camera to obtain thermoreflectance images [113].

The working principle of the phase-detection technique used in this work is shown in **Fig. 7.5**. On application of a sinusoidal current of magnitude I_0 and frequency ω, heating at frequency 2ω occurs. The temperature of the film oscillates at this 2ω frequency but with a phase difference determined by the thermal diffusivities of the film and substrate. In addition, there is a DC temperature rise (T_{DC}) of the film due to a DC component in the I^2R heating caused by the applied AC current in the heating wire. The oscillating temperature of the film causes the dielectric constant of the film to change at the same frequency, leading to a change in the optical spectrum which can be detected using a

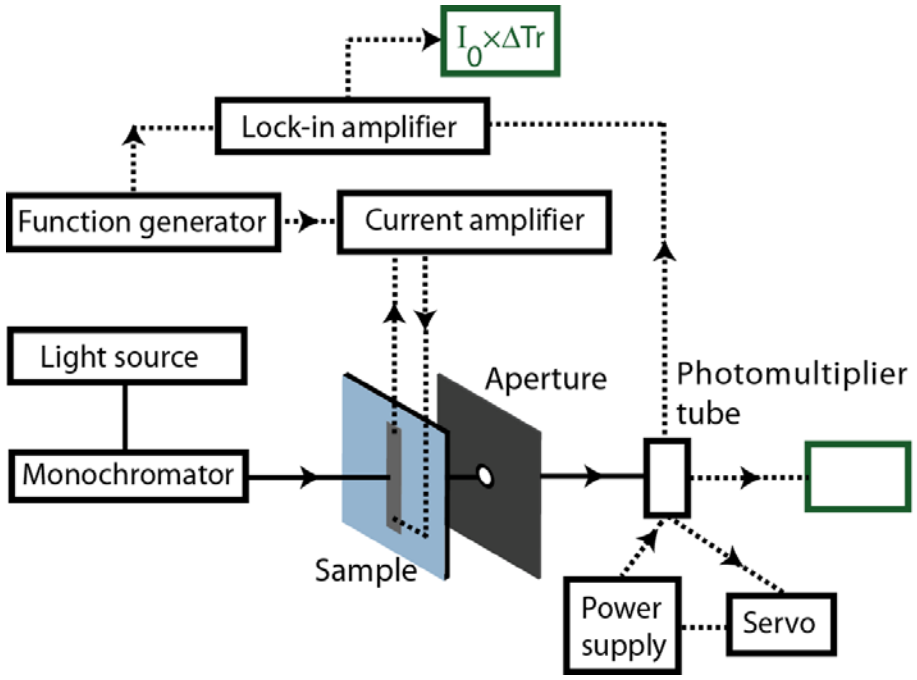

Figure 7.7. Experimental setup for measuring the temperature modulation spectrum. lock-in technique.

To demonstrate temperature modulation spectroscopy, we consider a sample consisting of a CuPc film deposited on top of a 0.2 mm thick glass cover slip as shown in **Fig. 7.6**. A silver heating wire of dimensions 13×1 mm^2 and thickness 50 nm is evaporated through a shadow mask on top of the CuPc film. Silver is chosen for the heating wire material because its temperature modulated transmission spectrum in the relevant energy range of 1.5-2.5 eV is negligible [114].

Figure 7.7 shows the experimental setup used for measuring the temperature modulation spectrum. The sample is mounted on a metal plate with a pinhole of diameter 0.7 mm to reduce the amount of light incident on the detector. Unpolarized light from an incandescent bulb is passed through a monochromator (Oriel 130 1/8m) and focused onto the sample. A photomultiplier tube (Hamamatsu R928) is used as the detector. Since the

light intensity from an incandescent bulb varies with wavelength, the DC output of the PMT also varies with the wavelength of light. To keep the DC output of PMT constant at the maximum possible level, a computer based servo is used to change the gain of the tube and achieve the desired constant DC output. For modulating the temperature of the thin film, an AC current is passed through the heating wire. The AC current is generated using a function generator to create a sine wave which is then input to a Howland current pump [115]. Because the change in transmitted intensity (or the AC signal) is of the order 10^{-4}, a lock-in amplifier (Stanford Research Systems 530) is used to sensitively measure the AC signal from the PMT. To quantify the sign of the AC signal with change in temperature, the temperature modulation spectrum of a thin gold film is measured and compared with that in literature.[116] The magnitude of temperature modulation is measured using a microthermocouple and is kept in the range of 1–1.5 K to satisfy the small perturbation requirement needed in order to measure the derivative spectrum.

7.4 Results and Discussion

7.4.1 Morphology of CuPc films

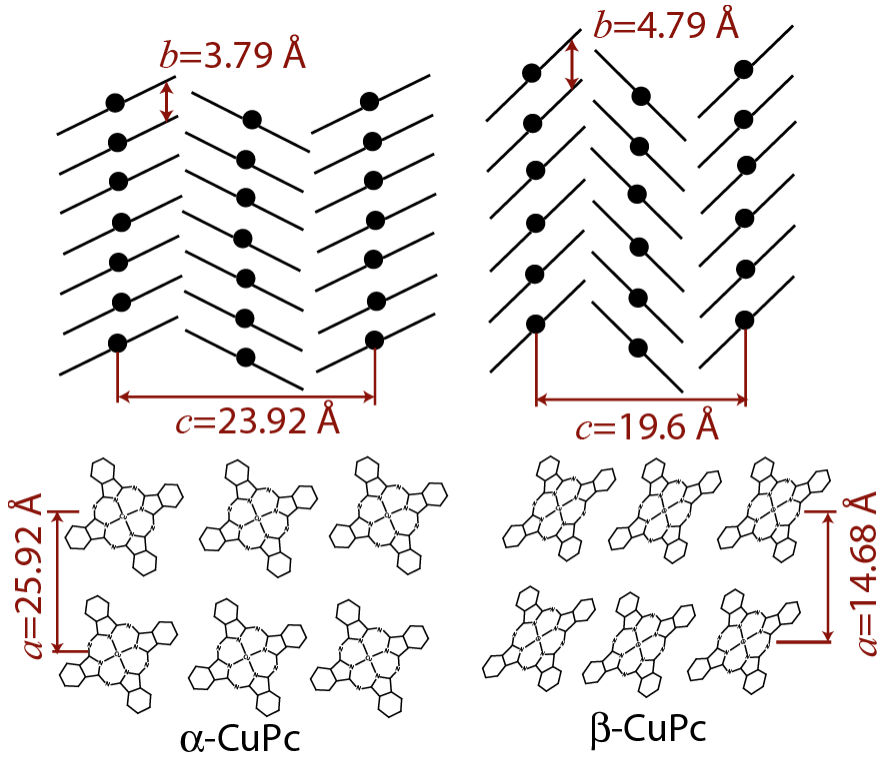

Figure 7.8. Crystal structure and lattice parameters of α and β CuPc.

CuPc has two polymorphic forms, α and β-CuPc, which are formed in a monoclinic lattice structure as shown in **Fig. 7.8**. While β-CuPc is the stable form of CuPc, as-deposited films are formed in α phase with their a-axis perpendicular to the substrate. This is seen from the X-ray diffraction data, shown in **Fig. 7.9**, for an as-deposited film and films annealed at 250 °C for 2 hours and 300 °C for 1 and 2 hours. For the as-deposited film, only (200), (400) and (600) planes of α-CuPc are visible. This is consistent with X-ray data in the literature for CuPc films deposited by vacuum thermal evaporation.[117] On annealing at 250 °C and 300 °C, a complete transformation from α to β phase is seen. On increasing the annealing temperature from 250 °C to 300 °C, the

rate of transformation from α to β phase is increased as is visible from the fact that the intensities of the peaks in samples annealed at 300 °C for 1 and 2 hours are larger than those annealed at 250 °C for 2 hours. The two main peaks seen in the XRD data correspond to (100) and ($\bar{2}$11) planes of the β-CuPc. With increasing annealing time and temperature the (100) peak increases in strength while the ($\bar{2}$11) peak remains constant, resulting in increasing orientation of *a* axis of β-CuPc perpendicular to substrate.

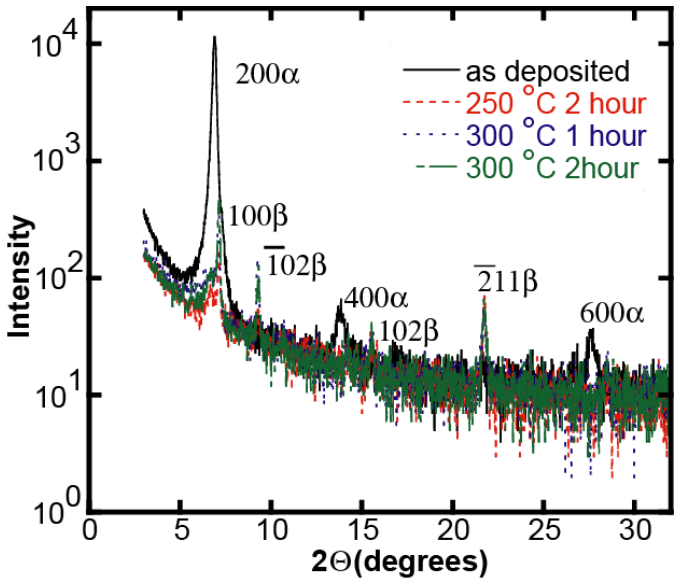

Figure 7.9. X-Ray diffraction data for *α* and *β*-CuPc. Data courtesy of Yansha Jin (University of Michigan)

Figure 7.10 shows atomic force microscopy (AFM) images of as-deposited and annealed CuPc films. For as-deposited film, an RMS surface roughness of 5 nm is measured. Crystal formation is observed upon annealing the film, with crystals growing perpendicular to the surface. This causes an increase in the rms roughness of the film which increases to 10 nm for films annealed at 250 °C for 2 hours, 15 nm for films annealed at 300 °C for 1 hours, and 21 nm for films annealed at 300 °C for 2 hours. Hence, with an increase in annealing temperature and time, the crystal size and height increase. Also, from the XRD data the peak at (100) plane is seen to increase in intensity.

It can therefore be concluded that the large crystals formed have (100) planes parallel to the surface, and the region between the crystals has mostly ($\bar{2}11$) planes parallel to the surface.

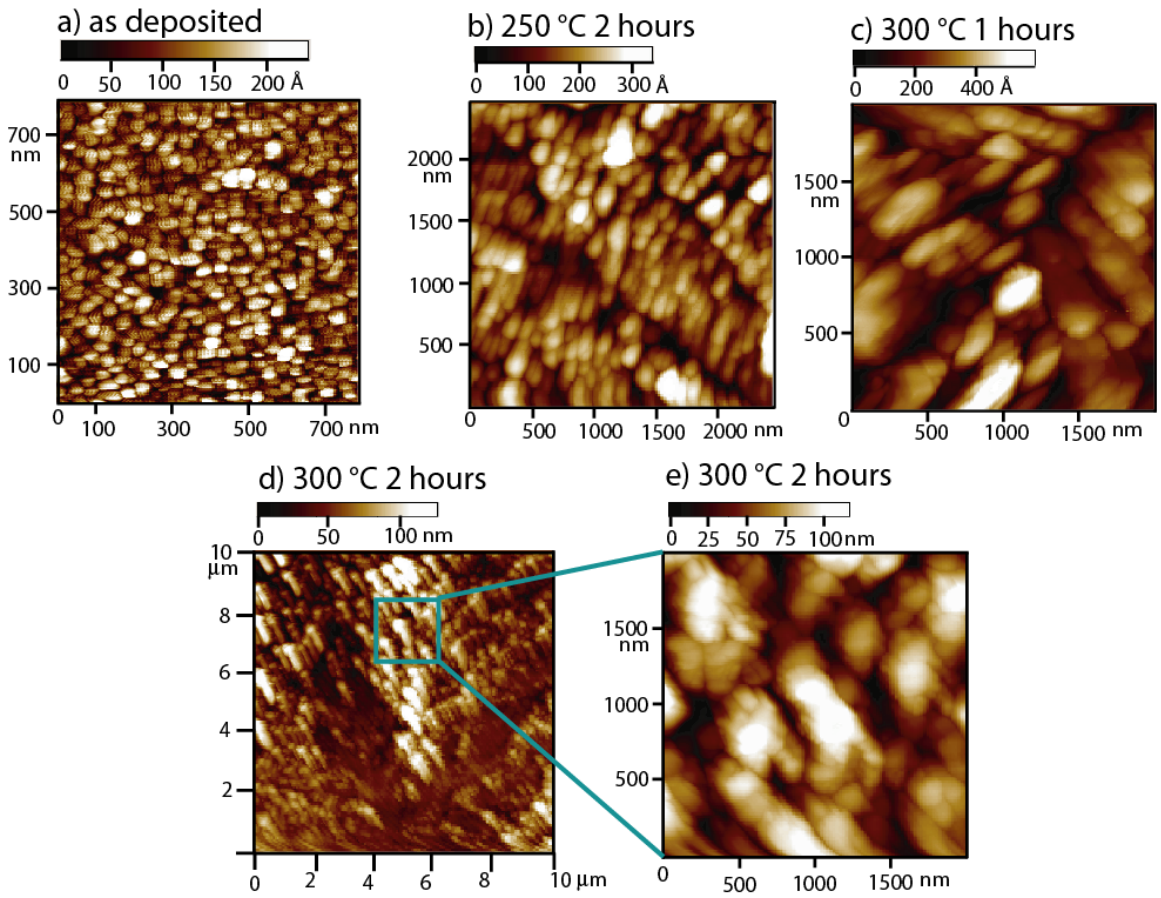

Figure 7.10. AFM image of a) as deposited CuPc films b) CuPc annealed at 250 ^{o}C for 2 hours c) CuPc annealed at 300 ^{o}C for 1 hour d) CuPc annealed at 300 ^{o}C for 2 hours e) AFM image of large crystals formed on annealing CuPc at ^{o}300 C for 2 hours. Data taken in a non-contact mode AFM (Agilent 5100 AFM).

7.4.2 Optical spectrum and data fitting

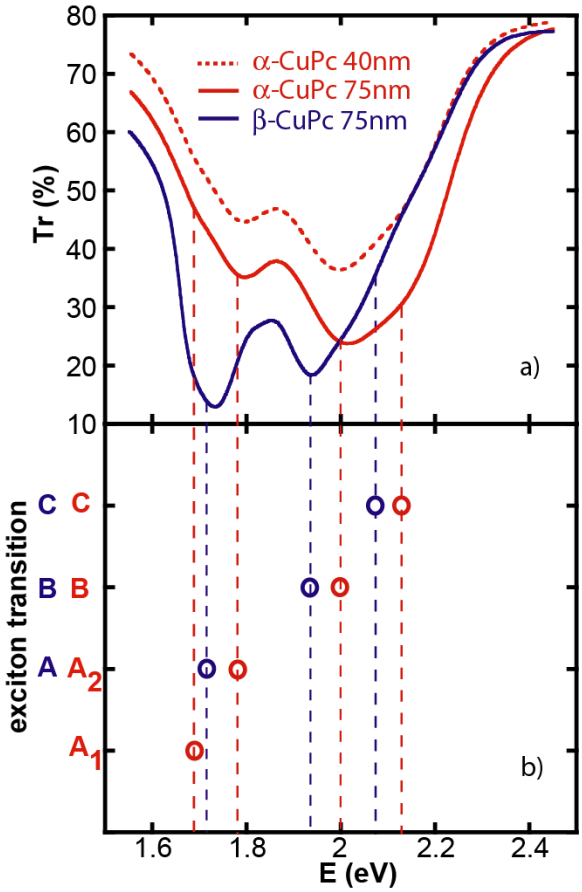

Figure 7.11. (a) Transmission spectrum of α and β CuPc films **(b)** exciton transition levels.

The presence of multiple exciton transition levels in a small energy range (~1eV) as well as lifetime broadening due to exciton-phonon interactions gives rise to a broad absorption spectrum. The transmission is related to the absorption length by the Beer-Lambert law. As with other modulation spectroscopies [101, 118], to distinguish and quantify the oscillator strengths, transition levels, and linewidths of different exciton levels, it is necessary to fit measured data to a modeled spectrum. We use the dielectric constant as written in Equation (7.7) to obtain the refractive index give by the equation:

$$n = \sqrt{\varepsilon} \tag{7.11}$$

where n is refractive index. The transmission $Tr(T_a)$ through the optically thin organic film and optically thick substrate can be modeled using Fresnel coefficients, taking into account multiple internal reflections using a matrix method [89] to obtain $E_{pi}(T_a)$, $E_{0i}(T_a)$, and $Q_i(T_a)$ as fitting parameters. These parameters can then be determined for all exciton transitions by minimizing the square of the error between the measured and modeled transmission spectra.

A temperature modulation due to periodic heating, ΔT_{AC}, causes a small change in the dielectric constant of CuPc. The perturbed dielectric constant is given by:

$$\varepsilon\left(T_0+\Delta T_{AC}\right)=\varepsilon_\infty+\sum_i \frac{E_{Pi}^2\left(T_0+\Delta T_{AC}\right)}{E_{0i}^2\left(T_0+\Delta T_{AC}\right)-E^2-iQ_i\left(T_0+\Delta T_{AC}\right)E} \tag{7.12}$$

where T_0 is the average temperature of the film. T_0 is higher than T_a by ΔT_{DC}, which is due to steady state heating caused by the periodic heating. For small ΔT_{AC} and ΔT_{DC} compared to T_a, the modulated values of E_{pi}, E_{0i} and Q_i can be approximated by:

$$E_{pi}\left(T_0+\Delta T_{AC}\right)=E_{pi}\left(T_a\right)+\frac{dE_{pi}}{dT}\left(\Delta T_{DC}+\Delta T_{AC}\right) \tag{7.13}$$

$$E_{0i}\left(T_0+\Delta T_{AC}\right)=E_{0i}\left(T_0\right)+\frac{dE_{0i}}{dT}\left(\Delta T_{DC}+\Delta T_{AC}\right) \tag{7.14}$$

$$Q_i\left(T_0+\Delta T_{AC}\right)=Q_i\left(T_0\right)+\frac{dQ_i}{dT}\left(\Delta T_{DC}+\Delta T_{AC}\right) \tag{7.15}$$

The change in transmission $\Delta Tr=Tr\left(T_0+\Delta T_{AC}\right)-Tr\left(T_0\right)$ can be modeled using Fresnel coefficients and solving for interference effects in the multilayer system of optically thin silver, optically thin CuPc, and optically thick substrate using a matrix method [89]. dE_{Pi}/dT, dE_{0i}/dT, and dQ_i/dT can then be obtained by a least-square minimization of the error in the modeled temperature modulation spectrum with respect to the measured spectrum.

Figure 7.11(a) shows the optical transmission spectra of as-deposited α-CuPc and annealed β-CuPc films. Results are shown for 2 different thicknesses of α-CuPc films, as well as a β-CuPc film of thickness 75 nm. The CuPc molecule has D_{4h} symmetry, which gives 2 degenerate transitions $a_{1u} \rightarrow e_g$ in the visible spectrum (Q band) [119]. On crystal formation, this degeneracy is lifted because of either the destruction of site symmetry or intermolecular distortion [103, 119]. A red shift in transition levels (known as a solvent shift) is also seen due to interactions between the molecules. This is illustrated in **Fig. 7.12**. A further splitting in these levels because of two different factor groups (Davydov splitting) can occur [119], but is seen only for the A band of α-CuPc.

CT excitons are formed because of intermolecular interactions between nearest

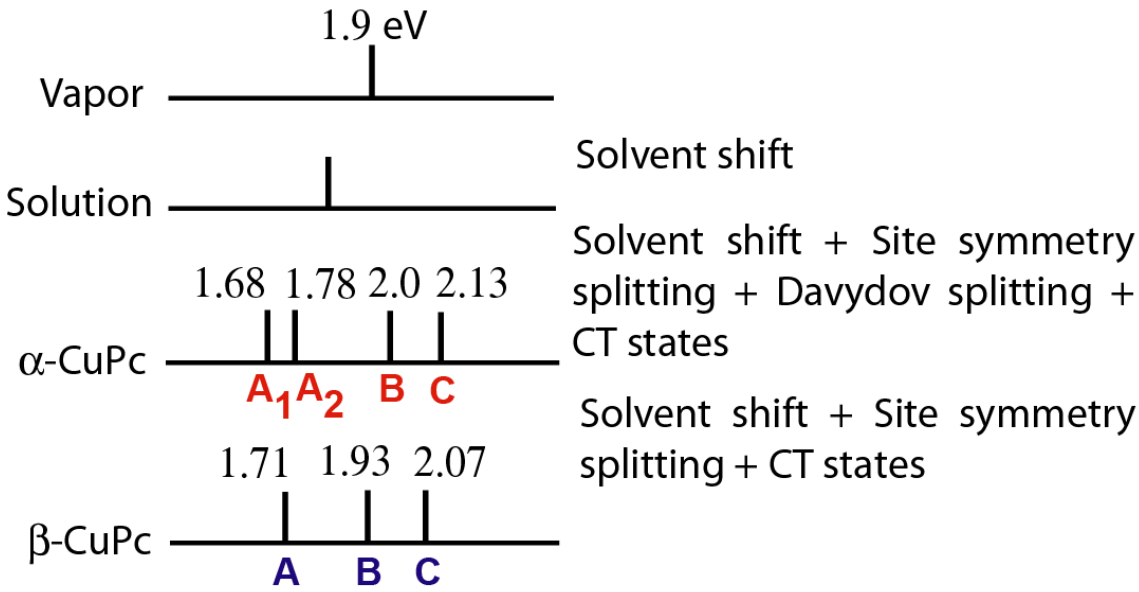

Figure 7.12. The shifts in exciton transition energy levels for CuPc that take place upon changing from vapor phase to condensed matter. The solvent shift is due to intermolecular interactions when going from vapor to solution phase. Davydov splitting occurs because of the formation of presence of two translationally inequivalent CuPc molecules in a unit cell.

neighboring molecules. Hence, we fit the spectrum of α-CuPc with a 4 oscillator model (A_1, A_2, B, C) and that of β-CuPc with a 3 oscillator model (A, B, C) [103]. **Figure 7.11(b)** plots the different excitonic transition levels obtained from fitting to the optical spectrum data.

7.4.3 Temperature modulation spectrum

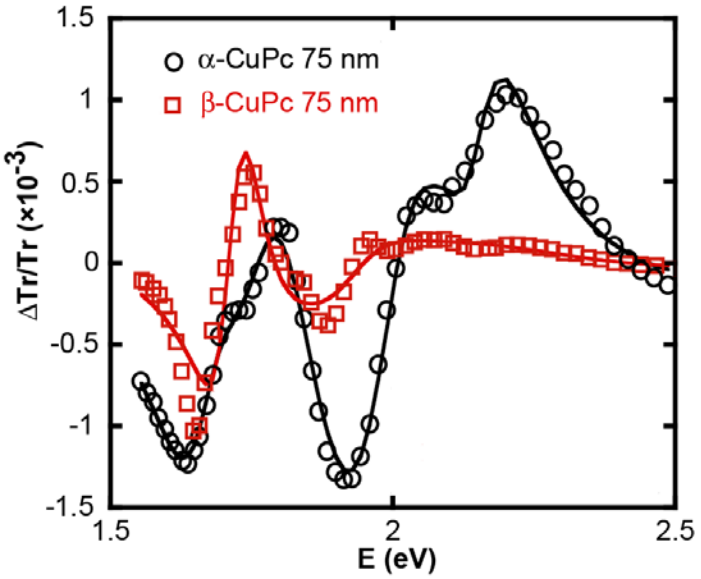

Figure 7.13. Temperature modulation spectra of α and β-CuPC films of thickness 75 nm. Square and circle correspond to the experimental data. Solid lines are fits to experimental data. The spectrum of β-CuPc has been scaled down 5 times to fit on the same scale. The AC temperature rise (ΔT_{AC}) is 1.1 K for α-CuPc and 0.95 K for β-CuPc. The DC temperature rise (ΔT_{DC}) is 21.3 K for α-CuPc and 7.7 K for β-CuPc.

The temperature modulation spectra of as-deposited and annealed films are shown in **Fig. 7.13**. Fits to the measured spectra are shown as solid lines. The spectrum of β-CuPc has been scaled down by a factor of 5 to fit on same y-axis scale. The AC temperature rise (ΔT_{AC}) is 1.1 K for α-CuPc and 0.95 K for β-CuPc. The DC temperature rise (ΔT_{DC}) is 21.3 K for α-CuPc and 7.7 K for β-CuPc. Peaks corresponding to different exciton

transition energies are visible in the modulation spectrum. For α-CuPc, the first three peaks (~ 1.65 eV, 1.8 eV and 1.93 eV) and the shoulder at ~ 2.05 eV correspond to the first 3 Frenkel exciton transitions [103]. The peak at ~ 2.2 eV corresponds to a CT exciton [103]. For β-CuPc, the first three peaks (~ 1.65 eV, 1.75 eV and 1.9 eV) correspond to the first 2 exciton transitions, and the peak at 2.05 eV corresponds to a CT exciton [103]. The modulation spectrum corresponding to the Frenkel exciton states is larger in β-CuPc than in α-CuPc, while the modulated spectrum of CT excitons is smaller. The increase in the modulation spectrum of Frenkel states could be because of increased roughness of the film observed in XRD and AFM data, which leads to an increase in effective thickness of the film because of light scattering at film surface. A decrease in the modulation spectrum corresponding to CT excitons is seen for β-CuPc because of a larger intermolecular spacing along the *b*-axis as compared to α-CuPc. This leads to a smaller effect on CT excitonic properties for β-CuPc than α-CuPc upon applying the same amplitude of temperature modulation.

Because of small intermolecular forces, the separation between the exciton transition levels is small in molecular crystals (~ 0.1 eV) as compared to inorganic crystals where the bandgaps are of the order of 1 eV. This leads to a strong overlap between the different exciton transition levels, leading to a broad absorption spectrum. The temperature modulation spectrum also shows this effect, and the assignment of peaks to different exciton transition levels is difficult because of spectral overlaps. In addition, a change in temperature leads to a shift in exciton transition levels as well as a change in the oscillator strength and linewidth. Hence, we use a data fitting method based on least square minimization of error in the calculated temperature modulation spectrum to link temperature modulation data to different exciton transition levels.

To understand the effect of temperature modulation on excitonic properties we must know the angle between the molecular polarizability and the electric field for each excitonic transition. Then, using equation (7.10), we can calculate the change in various electronic properties such as the dipole moment matrix element or the angle between the molecular plane and substrate. Evaporated CuPc films are formed with molecules stacked parallel to the substrate, and CT excitons are formed along the nearest neighbor direction, which is in the plane of the substrate. Hence, Xx_i=0 and E_{pi} can be written as:

$$E_{pi}^2 = 8\pi N V_{DA,i}^2 \hbar E_{0i} \tag{7.16}$$

For CT excitons, the matrix element can be written as $V_{DA,CT}^2 = V_0^2 \exp(-\beta d)$, where β is the coefficient of exponential decay that characterizes the strength of electron exchange between the two molecules and d is the equilibrium distance between the molecules [97] along the b-axis. The dependence of E_p on temperature (T) is then given by:

$$\frac{2}{E_{p,CT}}\frac{dE_{p,CT}}{dT} = \frac{1}{N}\frac{dN}{dT} + \frac{1}{E_{0,CT}}\frac{dE_{0,CT}}{dT} - \beta(d\alpha) \tag{7.17}$$

For Frenkel excitons we make the assumption that all transitions are polarized along same direction in the plane of the molecule. The molecular plane makes an angle of θ to the substrate normal. For plane unpolarized light incident perpendicular to the substrate, the electric field can be written as:

$$\vec{F} = F\left(\hat{X} + \hat{Y}\right) \tag{7.18}$$

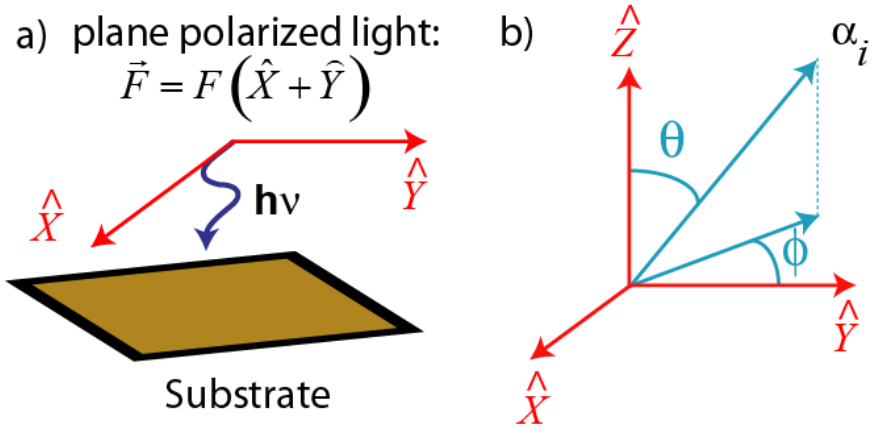

Figure 7.14. (a) Plane unpolarized light incident normally on substrate with electric field in the plane **(b)** Angle between molecular polarizability and laboratory axis.

where $\hat{X}$ and $\hat{Y}$ are unit vectors of the laboratory axis (or reference frame) with $\hat{Z}$ being the direction of light propagation perpendicular to the substrate as shown in **Fig. 7.14(a)**. Then, in addition to θ, another angle between the projection of molecular polarizability in the X-Y plane and Y axis is needed. This is denoted by ϕ, as shown in **Fig. 7.14(b)**. For crystalline films, the angle ϕ may be determined by the polarization of light, but evaporated films of CuPc are polycrystalline with crystals of size ~ 50nm randomly oriented on the surface as evident from XRD and AFM data. Hence the angle ϕ can be averaged from 0 to π, giving the average molecular polarizability for the i^{th} Frenkel transition as:

$$\alpha(E) = 2\hbar \sum_i \frac{E_{0i} V_{DA,i}^2 \sin^2(\theta)}{E_{0i}^2 - E^2 - iQ_i E} \tag{7.19}$$

The effective oscillator strength can then be written using Equations (7.7) and (7.8) as:

$$E_{pi}^2 = 8\pi N V_{DA,i}^2 \hbar E_{0i} \sin^2(\theta) \tag{7.20}$$

With a change in temperature, the dipole matrix element for Frenkel excitons is not expected to be altered significantly because it is a molecular property and is independent

of intermolecular interactions. The exciton transition level also varies slowly with temperature. Hence, the effect of temperature on effective oscillator strength for Frenkel excitons will come mainly from thermal expansion and molecular reorientation. With an increase in angle θ, the electric field is aligned more with the induced dipole moment of the molecules, increasing the oscillator strength of excitonic transitions. Neglecting the temperature dependences of the dipole matrix element and exciton transition level, the temperature dependence of Frenkel exciton oscillator strength can be written as:

$$\frac{\sum_{Frenkel} 2E_{Pi}\frac{dE_{Pi}}{dT}}{\sum_{Frenkel} E_{Pi}^2} = \frac{1}{N}\frac{dN}{dT} + 2\cot(\theta)\frac{d\theta}{dT} \tag{7.21}$$

The first term on right hand side is due to a decrease in the number density with thermal expansion. From our experiments, we find the left hand side of Equation (7.21) to be much larger than the decrease in number density. Hence, the main effect on increasing temperature is to change the molecular orientation. It is known that upon thermal annealing of CuPc films it is seen that the CuPc molecules lie flatter on the substrate or the angle θ is increased [120]. We therefore expect a similar behavior when the temperature is gradually increased.

Figure 7.15 (a) shows the temperature coefficient of E_{pi} for 75 nm thick α-CuPc and β-CuPc films. dE_p/dT for transitions A_2 and B for α-CuPc and A and B for β-CuPc is found to be positive, confirming their nature as Frenkel excitons; this is consistent with the results of electroabsorption spectroscopy [101].

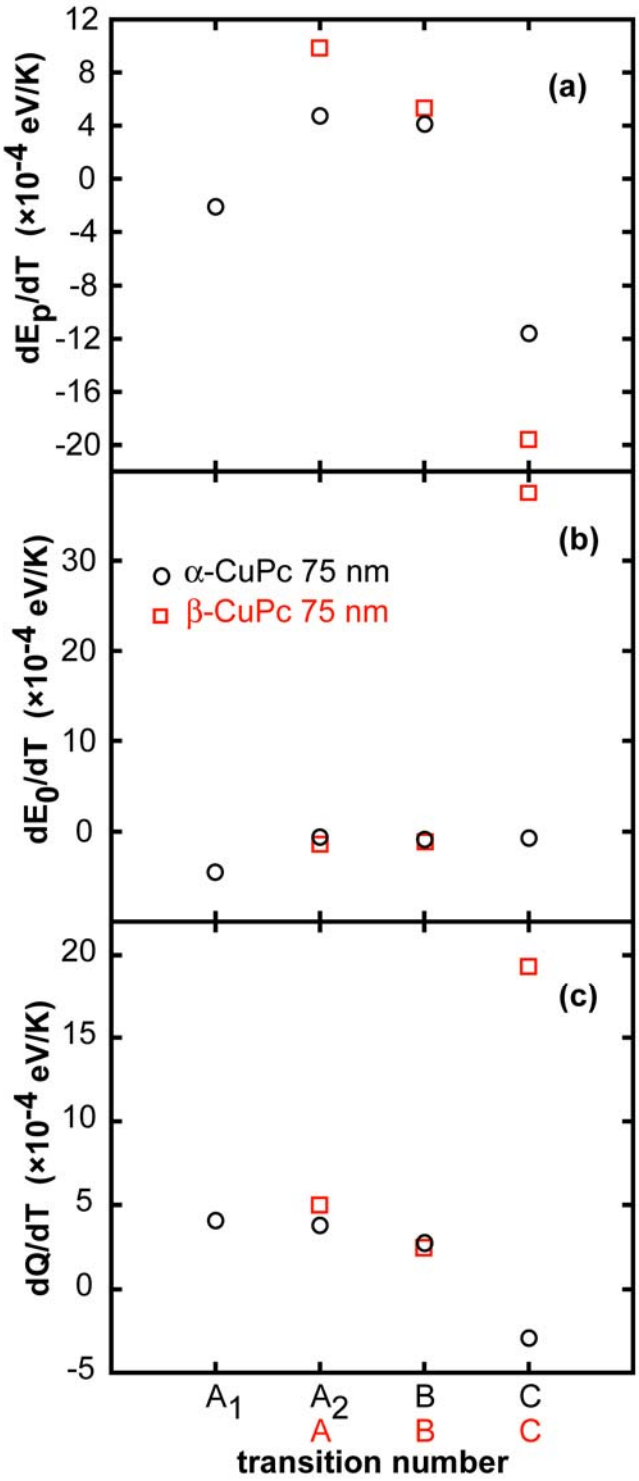

Figure 7.15. Temperature coefficient of **(a)** Oscillator strength, **(b)** Exciton transition level and **(c)** Lifetime broadening for α and β-CuPc.

Th

dE_p/dT. Hence, the C transition is of predominantly CT nature; this is confirmed with

electroabsorption spectroscopy [101]. The A_1 transition for α-CuPc has a negative dE_p/dT but has been identified as a Frenkel exciton in electroabsorption spectroscopy [101]. We expect a higher error in resolving the oscillator strength from the transmission spectrum for the A_1 transition in α-CuPc, because of lifetime broadening and its low oscillator strength. The higher measured dE_p/dT for transition C in β-CuPc in comparison to that in α-CuPc is in contradiction to the measured $\Delta Tr/Tr$ spectrum, where even a larger thickness of β-CuPc film has a smaller $\Delta Tr/Tr$ for the C transition as compared to α-CuPc. This is mostly likely because a larger equilibrium intermolecular distance along the stacking axis for β-CuPc leads to E_p for CT excitons being much less sensitive to changes in intermolecular distance than α-CuPc. This result is in contrast to electric field modulation, where CT states in β-CuPc are more sensitive to modulation amplitude of electric field than α-CuPc because of smaller mixing between CT and Frenkel excitons in β-CuPc, arising from a larger intermolecular distance along the *b*-axis [103].

Using Equation (7.17) and literature values for the coefficients of linear thermal expansion (1×10^{-4} for α-CuPc and 0.36×10^{-4} for β-CuPc [121]), we obtain a value of β of 13.6 $Å^{-1}$ for α-CuPc and 40.6 $Å^{-1}$ for β-CuPc. This value is significantly higher than those measured for LUMO-LUMO charge transfer in frozen media between various aromatic molecules such as biphenyl-naphthalene [97, 98]. The value of the transfer integral for HOMO-HOMO charge transfer is 5-10 times lower than LUMO-LUMO charge transfer, which could arise because of a larger β for HOMO-HOMO charge transfer [122]. Charge transfer excitons are formed between the HOMO of one molecule and the LUMO of a neighboring molecule. Because of the difference in energy levels and the spatial extent of electronic wavefunction between HOMO and LUMO levels, β is expected to be even larger for the case of charge transfer excitons. A discrepancy

between the values of β for α and β-CuPc is also seen, which most likely arises from the significant difference in thermal expansion coefficient.

The oscillator strength of Frenkel excitons is expected to increase with an increase in temperature because of an increase in the angle of molecules (θ) with respect to the substrate normal. The ratio $(\sum 2\times E_{pi}\times \mathrm{d}E_{pi}/\mathrm{d}T)/(\sum E_{pi}^2)$ is found to be 8.6 K^{-1} for α-CuPc and 18.4 K^{-1} for β-CuPc. The angle θ is not known with certainty for α and β-CuPc films, but it is expected to be larger for β-CuPc as evidenced by the smaller distance between the molecules along the *a*-axis in β-CuPc in comparison to α-CuPc. If π-π^* transitions are polarized in the plane of molecules, then using Equation (7.21) we find $\mathrm{d}\theta/\mathrm{d}T$ to be larger for β-CuPc in comparison to α-CuPc. The linear expansion coefficient of β-CuPc is smaller than α-CuPc. It can be concluded that the relaxation of intermolecular repulsion on increasing temperature occurs mostly through thermal expansion in α-CuPc but through molecular reorientation in β-CuPc. The molecules are inclined more in β-CuPc with respect to the normal to the surface than in α-CuPc. The end to end distance between neighboring molecules is smaller in α-CuPc, leading to a relatively larger thermal expansion.

Figure 7.15 (b) shows the temperature coefficients of E_{0i} for the same 75 nm thick α-CuPc film and 75 nm thick β-CuPc film as discussed above. Similar values of $\mathrm{d}E_0/\mathrm{d}T$ are obtained for β-CuPc and α-CuPc films, except for transition C for which there is a significant error in fitting as mentioned earlier. A general trend of E_0 to lower energies is seen. The magnitude of $\mathrm{d}E_0/\mathrm{d}T$ is also found to be smaller than $\mathrm{d}E_p/\mathrm{d}T$ or $\mathrm{d}Q/\mathrm{d}T$. Hence the exciton transition levels are affected to a lesser extent by temperature than by either oscillator strength or linewidth.

Figure 7.15 (c) shows the temperature coefficient of Q_i for the same 75 nm thick

α-CuPc film and 75 nm thick β-CuPc film. An increase in the linewidth is seen for Frenkel excitons in both α and β-CuPc, with the increase in linewidth being larger for lower energy excitons. The two lowest energy exciton bands have a minimum in the dispersion at k=0 according to reference [112]. Hence, lifetime broadening can occur only through the absorption of phonons. With an increase in temperature, phonon occupation at higher energies is increased, leading to a larger lifetime broadening. For the case of high energy excitons (B and C), the exciton dispersion shows a maximum at k=0 [112]. Hence, lifetime broadening occurs through the emission of phonons, which is a temperature independent process. Some increase in broadening is still seen for transition B, which could be caused by the absorption of phonons resulting from interband transitions. For the CT excitons, the linewidth shows a decrease for α-CuPc. The CT excitons in α-CuPc are strongly affected by temperature modulation, which may result in a decrease in exciton dispersion due to smaller interaction between neighboring molecules leading to a decrease in linewidth. For the case of β-CuPc there is a significant error in data fitting for CT excitons as seen in **Fig. 3**, which gives the erroneous result of a large increase in linewidth with temperature.

7.5 Summary and Conclusions

In summary, we have used the temperature modulation spectra of α and β-CuPc to quantify the interband coupling between molecules and differentiate exciton types. A dielectric model of excitons in conjunction with a least square minimization of error is used to determine the oscillator strength, exciton transition energy and linewidth from measured optical transmission. These values are then used to obtain the temperature coefficients of the oscillator strength, exciton transition energy, and linewidth from the

temperature modulation data. The oscillator strength for CT excitons is shown to decrease as temperature is increased, with the opposite behavior observed for Frenkel excitons. This criterion can be used to differentiate between Frenkel and CT excitons in organic semiconductors. The technique is shown to be more sensitive than electric field modulation spectroscopy for finding CT excitons with strong intermolecular interactions such as in α-CuPc. A shift in the exciton transition levels to lower energy is seen, but its magnitude is smaller than the temperature coefficients of oscillator strength and linewidth broadening. The linewidth increases with an increase in temperature. A larger increase in the linewidth broadening is seen for lower transition energies, which is attributed to temperature-dependent phonon absorption based lifetime broadening. In comparison, the linewidth broadening of higher energy excitons is through the temperature-independent process of phonon emission.

Chapter 8

Conclusions

8.1 Summary of present work

The aim of present work is to use thermal effects to understand electronic structure and transport properties in organic and inorganic semiconductors that play an important role in determining the efficiencies of thermoelectric and photovoltaic devices. In addition, innovative thermoelectric device geometries have been examined.

Thermoelectric energy conversion can provide many advantages over traditional compression cycle based engines or heat pumps, such as low cost, reliability, and small volume. However, current TE modules suffer from low conversion efficiency. In Chapter 2, we studied the tradeoff between electrical conductivity and Seebeck coefficient, a primary cause for low efficiency in bulk thermoelectric materials. Nanostructured materials provide an opportunity to circumvent this tradeoff by independently controlling the Seebeck coefficient and electrical conductivity. However, while 1D structures such as nanowires and nanowire superlattices have shown the potential for high ZT, practical devices based on these structures are plagued by practical difficulties. In Chapter 3, we examined nanocomposites based on quantum dots that are aligned to form 1D chains as an alternative method to achieve 1D transport (and consequently high ZT) without the practical difficulties of nanowires. An increase in the thermoelectric power factor of over

5 was predicted for InAs/GaAs quantum dot chains.

In spite of low efficiency, thermoelectric devices have applications in niche areas where cost or space requirements are important. Two such applications were investigated in Chapters 4 and 5. In Chapter 4, we demonstrated the feasibility of using monolithically integrated thermoelectric devices to cool HgCdTe-based infrared detectors. Using a steady state differential measurement, we measured the Seebeck coefficient and thermal conductivity of small barrier HgCdTe superlattices, deriving an upper limit for ZT of 1.4.

Chapter 5 examined the feasibility of thermoelectric textiles composed of thin film thermocouples on fibers. This technology could be suitable for waste heat recovery applications requiring large area flexible thermoelectric power generators. To demonstrate the fundamental building block of such a system, Ni-Ag thermocouples were fabricated on fibers, and thermoelectric power generation was measured. Plain weave geometries consisting of multiple fibers were also fabricated using a combination of thermal evaporation and electroless plating. The measured heat transfer coefficient of this device geometry was used to optimize convectively cooled thermoelectric segments and extrapolate performance to more high-performance thermoelectric material systems.

In Chapter 7, we studied thermal effects on excitonic properties of organic semiconductors. Excitons are of fundamental importance for the conversion of light into electricity in organic semiconductors. Recognizing that temperature affects a material's crystal structure by thermal expansion, we developed a phase-sensitive detection technique to measure the change in a material's transmission spectrum during temperature modulation. From the measured change in transmission spectrum for the organic material CuPc, the temperature derivatives of oscillator strength, exciton transition level, and lifetime broadening were calculated. The temperature derivative of

oscillator strength showed a clear distinction between Frenkel and CT excitons, demonstrating that the technique could be further applied to study the different mechanisms within the photovoltaic conversion process associated with these exciton types.

8.2 Suggestions for future work

8.2.1 Effect of band bending on thermoelectric power factor of metal nanoparticle-semiconductor nanocomposites

In Chapter 3 we examined quantum dot superlattices with unipolar doping. Bipolar doping or the presence of metal nanoparticles can significantly increase the electronic band bending at interfaces. It has been shown that the Seebeck coefficient can greatly increase in the depletion region surrounding an interface [123]. This could potentially be used to further enhance the thermoelectric performance predicted for quantum dot chains.

8.2.2 Fabrication of thermoelectric materials on plastic substrates

The feasibility of textile-based thermoelectric power generators has been demonstrated using metal thermocouples. However, the efficiency of such devices could be greatly increased if thin-film semiconductors with higher ZT (such as chalcogenides) could be fabricated on plastic substrates. Non-epitaxial growth of semiconductors can be achieved using vacuum methods such as vacuum thermal evaporation or solution-based methods such as electrodeposition. Films deposited using these methods are generally polycrystalline or amorphous, and optimization of annealing conditions are required to maximize their thermoelectric performance. In addition, surface preparation for maximizing adhesion is also important. The fabrication processes themselves must be optimized to obtain good quality films.

8.2.3 Stark effect imaging of organic field effect transistors

Stark effect spectroscopy has been used to study excitonic transitions in organic semiconductors; the change in optical spectrum has been shown to be proportional to square of the applied electric field. This method could also be used to study the local electric field in organic semiconductor devices such as thin film transistors. For example, if a light beam of less than 5μm diameter is scanned across a transistor channel while the Stark effect spectrum is simultaneously measured using a lock-in technique; the local electric field can be obtained. This map of the electric field would likely provide useful information regarding the mechanisms of charge injection.

Bibliography

[1] C. Kittel, *Introduction to solid state physics* (Wiley, New Jersey, 1966).

[2] K. P. Odonnell, and X. Chen, Appl. Phys. Lett. **58**, 2924 (1991).

[3] R. F. Pierret, *Semiconductor fundamentals* (Addison-Wesley, New York, 1983).

[4] G. Chen, *Nanoscale Energy Transport and Conversion: A Parallel Treatment of Electrons, Molecules, Phonons, and Photons* (Oxford University Press, New York, 2005).

[5] J. Singh, *Electronic and optoelectronic properties of semiconductor structures* (Cambridge University Press, New York, 2003).

[6] H. J. GOLDSMID, Rev. Gen. Therm. **6**, 102 (1967).

[7] A. F. Ioffe, *Semiconductor Thermoelements and Thermoelectric Cooling* (Infosearch, ltd., London, 1958).

[8] www.melcor.com

[9] S. W. Angrist, *Direct energy conversion* 1965), p. Medium: X; Size: Pages: 440.

[10] T. M. Tritt, Science **283**, 804 (1999).

[11] M. Lundstrom, *Fundamentals of Carrier Transport* (Cambridge University Press, Cambridge, 2000), p. 418.

[12] T. C. Harman *et al.*, Science **297**, 2229 (2002).

[13] L. D. Hicks *et al.*, Physical Review B **53**, 10493 (1996).

[14] D. A. Broido, and T. L. Reinecke, Physical Review B **51**, 13797 (1995).

[15] D. A. Broido, and T. L. Reinecke, Physical Review B **64**, 10 (2001).

[16] Y. M. Lin, X. Z. Sun, and M. S. Dresselhaus, Physical Review B **62**, 4610 (2000).

[17] Y. M. Lin, and M. S. Dresselhaus, Physical Review B **68**, 14 (2003).

[18] N. Mingo, Appl. Phys. Lett. **84**, 2652 (2004).

[19] N. Mingo, Appl. Phys. Lett. **85**, 5986 (2004).

[20] A. R. Abramson *et al.*, J. Microelectromech. Syst. **13**, 505 (2004).

[21] M. S. Dresselhaus *et al.*, Adv. Mater. **19**, 1043 (2007).

[22] D. J. Bergman, and O. Levy, J. Appl. Phys. **70**, 6821 (1991).

[23] A. A. Balandin, and O. L. Lazarenkova, Appl. Phys. Lett. **82**, 415 (2003).

[24] W. Ye *et al.*, in 32nd Annual Conference on the Physic and Chemistry of Semiconductor Interfaces (A V S Amer Inst Physics, Bozeman, MT, 2005), pp. 1736.

[25] B. Lita *et al.*, Appl. Phys. Lett. **74**, 2824 (1999).

[26] Z. M. Wang *et al.*, Appl. Phys. Lett. **84**, 1931 (2004).

[27] T. Mano *et al.*, J. Appl. Phys. **95**, 109 (2004).

[28] L. Li *et al.*, Appl. Phys. Lett. **92**, 3 (2008).

[29] N. Mingo, and D. A. Broido, Phys. Rev. Lett. **93**, 4 (2004).

[30] W. Kim *et al.*, Phys. Rev. Lett. **96**, 4 (2006).

[31] B. Yang *et al.*, Appl. Phys. Lett. **80**, 1758 (2002).

[32] K. Brunner, Rep. Prog. Phys. **65**, 27 (2002).

[33] S. Kiravittaya *et al.*, Nanoscale Res. Lett. **1**, 1 (2006).

[34] K. L. Wang *et al.*, Proc. IEEE **95**, 1866 (2007).

[35] G. Bastard, *Wave mechanics applied to semiconductor heterostructures* (Wiley-Interscience, **1988**).

[36] M. Califano, and P. Harrison, J. Appl. Phys. **86**, 5054 (1999).

[37] O. L. Lazarenkova, and A. A. Balandin, in 6th International on Quantum Confinement - Nanostructured Materials and Devices, edited by M. Cahay *et al.* (Electrochemical Society Inc, San Francisco, Ca, 2001), pp. 238.

[38] S. Tiwari, and D. J. Frank, Appl. Phys. Lett. **60**, 630 (1992).

[39] M. Califano, and P. Harrison, J. Appl. Phys. **88**, 5870 (2000).

[40] M. A. Cusack, P. R. Briddon, and M. Jaros, Physical Review B **54**, R2300 (1996).

[41] M. Grundmann, O. Stier, and D. Bimberg, Physical Review B **52**, 11969 (1995).

[42] O. L. Lazarenkova, and A. A. Balandin, Physical Review B **66**, 9 (2002).

[43] J. R. Leite *et al.*, in 1st International Conference on Low Dimensional Structures and Devices (Elsevier Science Sa Lausanne, Singapore, Singapore, 1995), pp. 250.

[44] D. K. C. MacDonald, *Thermoelectricity: An Introduction to the Principles* (Dover Publications 2006).

[45] X. Kleber *et al.*, Model. Simul. Mater. Sci. Eng. **13**, 341 (2005).

[46] D. Ganapathy, K. Singh, and P. E. Phelan, J. Heat Transf.-Trans. ASME **127**, 553 (2005).

[47] A. Wacker, and A. P. Jauho, Phys. Rev. Lett. **80**, 369 (1998).

[48] O. L. Lazarenkova, and A. A. Balandin, J. Appl. Phys. **89**, 5509 (2001).

[49] A. Rogalski, *Infrared detectors* (CRC Press, Amsterdam, 2000).

[50] R. W. Miles, in *Properties of Mercury Cadmium Telluride*, edited by J. Brice, and P. Caper (INSPEC, New York, 1987), p. 111.

[51] R. J. Radtke, H. Ehrenreich, and C. H. Grein, J. Appl. Phys. **86**, 3195 (1999).

[52] D. Vashaee, and A. Shakouri, J. Appl. Phys. **95**, 1233 (2004).

[53] D. Vashaee, and A. Shakouri, Appl. Phys. Lett. **88**, 3 (2006).

[54] G. H. Zeng *et al.*, J. Appl. Phys. **101**, 5 (2007).

[55] B. Yang *et al.*, Appl. Phys. Lett. **81**, 3588 (2002).

[56] T. Borca-Tasciuc *et al.*, Superlattices Microstruct. **28**, 199 (2000).

[57] Y. Zhang *et al.*, in *Thermoelectric Materials 2003-Research and Applications*, edited by G. S. Nolas *et al.* (Materials Research Society, Warrendale, 2004), pp. 59.

[58] J. O. Sofo, G. D. Mahan, and J. Baars, J. Appl. Phys. **76**, 2249 (1994).

[59] C. LaBounty *et al.*, Optical Engineering **39**, 2847 (2000).

[60] N. K. Dutta *et al.*, Appl. Phys. Lett. **47**, 222 (1985).

[61] P. R. Berger *et al.*, Appl. Phys. Lett. **59**, 117 (1991).

[62] E. E. Antonova, D. C. Looman, and Ieee, *Finite elements for thermoelectric device analysis in ANSYS* (Ieee, New York, 2005), pp. 200.

[63] C. Nui, T. A. S. Srinivas, and H. Ahmed, Microelectromechanical Systems, Journal of **6**, 136 (1997).

[64] S. Velicu *et al.*, J. Electron. Mater. **37**, 1504 (2008).

[65] J. Yang, in American Physical Society March Meeting, Energy Workshop, New Orleans, Louisiana (March 9, 2008).

[66] A. I. Casian, in *Thermoelectrics Handbook: Macro to Nano*, edited by D. M. Rowe (CRC Press, London 2006).

[67] C. Lungenschmied *et al.*, Solar Energy Materials and Solar Cells **91**, 379 (2007).

[68] B. O'Connor *et al.*, Adv. Mater. **19**, 3897 (2007).

[69] J. J. Allen, and A. J. Smits, Journal of Fluids and Structures **15**, 629 (2001).

[70] F. Mohammadi, A. Khan, and R. B. Cass, in Symposium on Electronics on Unconventional Substrates-Electrotextiles and Giant-Area Flexible Circuits held at the 2002 MRS Fall Meeting, edited by M. S. Shur, P. M. Wilson, and D. Urban (Materials

Research Society, Boston, Ma, 2002), pp. 263.

[71] J. A. Paradiso, and T. Starner, Pervasive Computing, IEEE **4**, 18 (2005).

[72] K. Itoigawa *et al.*, in 4thInternational Workshop on Micro and Nanotechnology for Power Generation and Energy Conversion Applications (Iop Publishing Ltd, Kyoto, JAPAN, 2004), pp. S233.

[73] N. Sato, M. Takeda, and Ieee, in 24th International Conference on Thermoelectrics (ICT) (Ieee, Clemson, SC, 2005), pp. 160.

[74] A. P. Ghosh *et al.*, Appl. Phys. Lett. **86**, 223503 (2005).

[75] A. Dhawan *et al.*, in Symposium on Electronics on Unconventional Substrates-Electrotextiles and Giant-Area Flexible Circuits held at the 2002 MRS Fall Meeting, edited by M. S. Shur, P. M. Wilson, and D. Urban (Materials Research Society, Boston, Ma, 2002), pp. 67.

[76] A. R. Horrocks, and S. C. Anand, *Handbook of Technical Textiles* (Woodhead Publishing Cambridge, England, 2000).

[77] Syukri *et al.*, Thin Solid Films **422**, 48 (2002).

[78] W. Zhang *et al.*, Microelectronic Engineering **76**, 146 (2004).

[79] F. J. Blatt *et al.*, *Thermoelectric Power of Metals* (Plenum press, New York 1976).

[80] S. W. Angrist, *Direct Energy Conversion* (Allyn and Bacon Inc., Boston 1982).

[81] G. Min, and D. M. Rowe, in *CRC Handbook of Thermoelectrics*, edited by D. M. Rowe (CRC Press, London 1995).

[82] D. M. Rowe, and G. Min, Journal of Power Sources **73**, 193 (1998).

[83] F. P. I. a. D. P. DeWitt, *Fundamentals of Heat & Mass Transfer* (John Wiley & Sons, New York 2002).

[84] L. W. d. Silva, M. Kaviany, and C. Uher, J. Appl. Phys. **97**, 114903 (2005).

[85] L. M. Goncalves *et al.*, in Thermoelectrics, 2006. ICT '06. 25th International Conference on2006), pp. 327.

[86] J. L. Bredds, and J. R. Durrant, Accounts Chem. Res. **42**, 1689 (2009).

[87] M. Schwoerer, and H. C. Wolf, *Organic Molecular Solids* (Wiley-VCH, 2007).

[88] http://www.nrel.gov/pv/thin_film/docs/kaz_best_research_cells.ppt

[89] P. Peumans, A. Yakimov, and S. R. Forrest, J. Appl. Phys. **93**, 3693 (2003).

[90] S. R. Forrest, Nature **428**, 911 (2004).

[91] M. Pope, and C. E. Swenberg, *Electronic Processes in Organic Crystals* (Oxford University Press, New York, 1982).

[92] E. A. Silinsh, and V. Capek, *Organic Molecular Crystals* (AIP Press, New York, 1994).

[93] Y. Vertsimakha *et al.*, Thin Solid Films **515**, 7950 (2007).

[94] V. Bulovic, and S. R. Forrest, Chem. Phys. Lett. **238**, 88 (1995).

[95] J. L. Bredas *et al.*, Proc. Natl. Acad. Sci. U. S. A. **99**, 5804 (2002).

[96] N. Koch *et al.*, Phys. Rev. Lett. **96**, 4 (2006).

[97] R. A. Marcus, and N. Sutin, Biochimica Et Biophysica Acta **811**, 265 (1985).

[98] J. R. Miller, J. V. Beitz, and R. K. Huddleston, J. Am. Chem. Soc. **106**, 5057 (1984).

[99] M. Cardona, *Modulation spectroscopy* (Academic Press, New York, 1969).

[100] R. K. Willardson, and A. C. Beer, *Modulation techniques* (Academic Press, New York, 1972).

[101] L. Sebastian, G. Weiser, and H. Bassler, Chemical Physics **61**, 125 (1981).

[102] G. U. Bublitz, and S. G. Boxer, Annual Review Of Physical Chemistry **48**, 213

(1997).

[103] H. Yoshida, Y. Tokura, and T. Koda, Chemical Physics **109**, 375 (1986).

[104] Z. Shen *et al.*, Chem. Phys. Lett. **236**, 129 (1995).

[105] W. Stampor, Chemical Physics **305**, 77 (2004).

[106] M. Liess *et al.*, Synthetic Metals **102**, 1075 (1999).

[107] F. Rohlfing, T. Yamada, and T. Tsutsui, J. Appl. Phys. **86**, 4978 (1999).

[108] C. Giebeler *et al.*, Applied Physics Letters **75**, 2144 (1999).

[109] W. Stampor, Chemical Physics **334**, 216 (2007).

[110] N. W. Ashcroft, and N. D. Mermin, *Solid State Physics* (Holt, Rinehart and Winston, New York, 1976).

[111] W. H. Flygare, *Molecular Structure and Dynamics* (Prentice Hall Englewood Cliffs, NJ.

[112] Y. Iyechika, K. Yakushi, and H. Kuroda, Chemical Physics **87**, 101 (1984).

[113] P. K. L. Chan *et al.*, Appl. Phys. Lett. **89**, 011110 (2006).

[114] R. Rosei, C. H. Culp, and J. H. Weaver, Physical Review B **10**, 484 (1974).

[115] L. T. Harrison, *Current Sources and Voltage References* (Elseiver, New York, 2005).

[116] R. Rosei, Antonang.F, and U. M. Grassano, Surf. Sci. **37**, 689 (1973).

[117] O. Berger *et al.*, Journal Of Materials Science-Materials In Electronics **11**, 331 (2000).

[118] M. Tanaka *et al.*, Journal Of Chemical Physics **95**, 2371 (1991).

[119] E. A. Lucia, and F. D. Verderame, The Journal of Chemical Physics **48**, 2674 (1968).

[120] S. Dogo *et al.*, Thin Solid Films **219**, 244 (1992).

[121] C. Hamann, and M. Schenk, Kristall und Technik **6**, K103 (1971).

[122] J. Kjelstrup-Hansen *et al.*, Organic Electronics **10**, 1228 (2009).

[123] K. P. Pipe, *Bipolar thermoelectric devices*, PhD Thesis (Massachusetts Institute of Technology, Boston, 2004)